MODELING, VALIDATION AND PARAMETRIC ANALYSIS OF THE AXIAL DYNAMICS OF A VIBRATION-ASSISTED DRILLING TOOL

Eduardo Ferreira Vieira d'Almeida

Dissertação de Mestrado apresentada ao Programa de Pós-graduação em Engenharia Mecânica, COPPE, da Universidade Federal do Rio de Janeiro, como parte dos requisitos necessários à obtenção do título de Mestre em Engenharia Mecânica.

Orientador: Thiago Gamboa Ritto

Rio de Janeiro
Julho de 2019

MODELING, VALIDATION AND PARAMETRIC ANALYSIS OF THE AXIAL DYNAMICS OF A VIBRATION-ASSISTED DRILLING TOOL

Eduardo Ferreira Vieira d'Almeida

DISSERTAÇÃO SUBMETIDA AO CORPO DOCENTE DO INSTITUTO ALBERTO LUIZ COIMBRA DE PÓS-GRADUAÇÃO E PESQUISA DE ENGENHARIA (COPPE) DA UNIVERSIDADE FEDERAL DO RIO DE JANEIRO COMO PARTE DOS REQUISITOS NECESSÁRIOS PARA A OBTENÇÃO DO GRAU DE MESTRE EM CIÊNCIAS EM ENGENHARIA MECÂNICA.

Examinada por:

Prof. Thiago Gamboa Ritto, D.Sc.

Prof. Romulo Reis Aguiar, D.Sc.

Prof. Edson Luiz Cataldo Ferreira, D.Sc.

Prof. Fernando Augusto de Noronha Castro Pinto, D.Sc.

RIO DE JANEIRO, RJ – BRASIL
JULHO DE 2019

d'Almeida, Eduardo Ferreira Vieira

Modeling, validation and parametric analysis of the axial dynamics of a vibration-assisted drilling tool/Eduardo Ferreira Vieira d'Almeida. – Rio de Janeiro: UFRJ/COPPE, 2019.

XXIV, 121 p.: il.; 29, 7cm.

Orientador: Thiago Gamboa Ritto

Dissertação (mestrado) – UFRJ/COPPE/Programa de Engenharia Mecânica, 2019.

Referências Bibliográficas: p. 118 – 121.

1. lumped parameters system. 2. model validation. 3. nonlinear dynamics. 4. vibration-assisted drilling. 5. vibro-impact. I. Ritto, Thiago Gamboa. II. Universidade Federal do Rio de Janeiro, COPPE, Programa de Engenharia Mecânica. III. Título.

"The experimenter who does not know what he is looking for will not understand what he finds."
— Claude Bernard (1813 - 1878)

Acknowledgments

I would like to acknowledge Schlumberger, UFRJ, CNPq, and CAPES for the financial support for this work.

I would like to thank the BTiC team at Schlumberger for providing the ideal working conditions that made this work possible. Being a member of the BTiC team at Schlumberger made me perceive the oil field industry not only in an engineering perspective, but in a geological, in a geomechanical, and in a petrophysical perspective.

To my advisor Thiago Ritto, I would like to thank you for your guidance throughout these two years. This work would not have been possible without your support.

I would like to thank Romulo Aguiar for the opportunity to work alongside him at Schlumberger. The advises that you gave me helped me to grow and improve personally and professionally. I am forever grateful for your support and I will always carry the core values that you have taught me.

This work was made possible due to the unconditional support of my family, whose love and encouragement helped me endure this arduous journey. I would like to thank my girlfriend Daniella for always being by my side and for providing me with a safe haven. Additionally, I would like to take liberty to thank my grandmother Nelsa in my native language: *Vó, gostaria de lhe agradecer todo o apoio e conselhos que recebi durante toda a minha vida. Como avó e madrinha, essa conquista também é sua.*

Resumo da Dissertação apresentada à COPPE/UFRJ como parte dos requisitos necessários para a obtenção do grau de Mestre em Ciências (M.Sc.)

MODELAGEM, VALIDAÇÃO E ANÁLISE PARAMÉTRICA DA DINÂMICA AXIAL DE UMA FERRAMENTA DE PERFURAÇÃO ASSISTIDA DE VIBRAÇÃO

Eduardo Ferreira Vieira d'Almeida

Julho/2019

Orientador: Thiago Gamboa Ritto

Programa: Engenharia Mecânica

Um modelo de vibro-impacto de parâmetros concentrados é desenvolvido para descrever a dinâmica axial de um protótipo de ferramenta de perfuração assistida por vibração, a qual foi desenvolvida para melhorar a eficiência de perfuração em formações duras. O modelo proposto possui sete graus de liberdade com quatro superfícies de impacto. Dados de campo adquiridos em alta freqüência, os quais foram medidos em múltiplos locais da ferramenta, são utilizados para validar o modelo matemático. Uma análise paramétrica é realizada para investigar a influência que certos parâmetros de projeto têm sobre comportamento dinâmico do sistema. Além disso, uma métrica é proposta para avaliar a eficiência do processo de perfuração, e indicar modificações de projeto da ferramenta de vibro-impacto original. Os resultados mostram uma correspondência satisfatória entre dados de campo e saídas de modelo, visto que o modelo de vibro-impacto é capaz de capturar e reproduzir o comportamento dinâmico da ferramenta de perfuração assistida por vibração. Além disso, o modelo proposto é capaz de reproduzir um comportamento dinâmico complexo com pouco custo computacional devido ao baixo número de graus de liberdade. Os resultados da análise paramétrica revelam a possibilidade de aumento de 85% na transferência da força de impacto e 125% de aumento na faixa de operação, quando comparados com o projeto original.

Abstract of Dissertation presented to COPPE/UFRJ as a partial fulfillment of the requirements for the degree of Master of Science (M.Sc.)

MODELING, VALIDATION AND PARAMETRIC ANALYSIS OF THE AXIAL DYNAMICS OF A VIBRATION-ASSISTED DRILLING TOOL

Eduardo Ferreira Vieira d'Almeida

July/2019

Advisor: Thiago Gamboa Ritto

Department: Mechanical Engineering

The purposes of this work are: to develop a mathematical model that represents the axial dynamics of a vibration-assisted drilling tool, to validate the proposed mathematical model with field data, and to analyze the axial nonlinear dynamics of a vibro-impact system used as a drilling tool. A lumped-parameter vibro-impact model is presented to describe the axial dynamics of a prototype vibration-assisted drilling tool developed to improve the drilling efficiency in hard-rock formations. The proposed model has seven degrees of freedom with four impact surfaces. Field data from high-frequency acquisition, measured at multiple locations, is used to validate the mathematical model. A parametric analysis investigates the effect that some design parameters have on the dynamic behavior of the system. Furthermore, a measure is proposed to evaluate the efficiency of the process, and used for design modifications of the current vibro-impact system. The results show an overall reasonable match between field data and model outputs because the vibro-impact model is capable of reproducing the main dynamic behavior of the vibration-assisted drilling tool. Furthermore, the proposed model is able to reproduce complex dynamic behavior with little computational cost due to the small number of degrees of freedom. The results from the parametric analysis reveal the possibility of 85% increase in the impact force transfer and 125% increase in the mud flow operating range, when compared with the original design.

Contents

List of Figures

List of Tables

List of Symbols

F	Generic representation of an impact force, p. 104
F_o	Maximum magnitude of the excitation force, p. 40
$F_D(\dot{x_2})$	Fluid-structure interaction force, p. 38
$F_H(x_2, x_3, t)$	Excitation force, p. 38
$F_I(x_1, \dot{x_1}, x_2, \dot{x_2})$	Impact force from the impact face, p. 38
$F_{Off}(x_1, \dot{x_1}, x_3, \dot{x_3})$	Impact force from the off-bottom shoulder, p. 37
$F_{On}(x_1, \dot{x_1}, x_3, \dot{x_3})$	Impact force for the on-bottom shoulder, p. 37
$F_R(x_1, \dot{x_1})$	Bit-rock interaction force, p. 38
$F_S(x_2, \dot{x_2}, x_3, \dot{x_3})$	Force from the recoil spring, p. 37
$H(\delta)$	Heaviside function, p. 39
J^*	Impulse per second, p. 104
L_1	Distance from the top to the first degree-of-freedom, p. 41
L_2	Distance from the top of the second degree-of-freedom, p. 40
L_3	Length from the top to the third degree-of-freedom, p. 39
L_R	Distance between the rigid support and the flexible support that represents the rock formation, p. 41
L_S	Length of the recoil spring, p. 40
L_I	Distance between impact surfaces #2 and #3, p. 39
L_{On}	Gap between the on-bottom and the off-bottom shoulders, p. 39
L_{gap}	Gap between the impacting mass and the recoil spring, p. 110

L_{gap} Gap between the impacting mass and the recoil spring proposed for every simulation, p. 110

Q Mud flow rate in gallons per minute, p. 40

Z_i^* Average impacts per cycle in a given impact surface represented by the subscript i, p. 102

α Constant that converts the mud flow rate from gallons per minute to radians per second, p. 40

β Constant that converts displacement into radians, p. 40

$\ddot{x}_1$ Axial acceleration of the first degree-of-freedom, p. 38

$\ddot{x}_2$ Axial acceleration of the second degree-of-freedom, p. 38

$\ddot{x}_3$ Axial acceleration of the third degree-of-freedom, p. 37

$\ddot{x}_4$ Axial acceleration of the fourth degree-of-freedom, p. 37

$\ddot{x}_5$ Axial acceleration of the fifth degree-of-freedom, p. 37

$\ddot{x}_6$ Axial acceleration of the sixth degree-of-freedom, p. 37

$\ddot{x}_7$ Axial acceleration of the seventh degree-of-freedom, p. 36

δ_I Indentation coefficient related to impact surface #2, p. 39

δ_{Off} Indentation coefficient related to impact surface #3, p. 39

δ_{On} Indentation coefficient related to impact surface #4, p. 39

δ_R Indentation coefficient related to the rock formation, p. 41

δ_S Indentation coefficient related to impact surface #1, p. 40

$\dot{x}_1$ Axial velocity of the first degree-of-freedom, p. 38

$\dot{x}_2$ Axial velocity of the second degree-of-freedom, p. 38

$\dot{x}_3$ Axial velocity of the third degree-of-freedom, p. 37

$\dot{x}_4$ Axial velocity of the fourth degree-of-freedom, p. 37

$\dot{x}_5$ Axial velocity of the fifth degree-of-freedom, p. 37

$\dot{x}_6$ Axial velocity of the sixth degree-of-freedom, p. 37

$\dot{x}_7$ Axial velocity of the seventh degree-of-freedom, p. 36

ϕ Initial phase difference related to the influence of the mud flow rate, p. 40

ψ Phase difference introduced by the dependency on the relative displacement between the second and third degrees-of-freedom, p. 40

c_3 Viscous damping of the third degree-of-freedom, p. 37

c_4 Viscous damping of the fourth degree-of-freedom, p. 37

c_5 Viscous damping of the fifth degree-of-freedom, p. 37

c_6 Viscous damping of the sixth degree-of-freedom, p. 37

c_7 Viscous damping of the seventh degree-of-freedom, p. 36

c_D Drag coefficient of the low viscosity fluid, p. 40

c_I Viscous damping coefficient related to impact surface #2, p. 39

c_{Off} Viscous damping coefficient related to impact surface #3, p. 39

c_{On} Viscous damping coefficient related to impact surface #4, p. 39

c_R Viscous damping coefficient related to the rock formation, p. 41

c_S Viscous damping coefficient related to impact surface #1, p. 40

k_3 Axial stiffness coefficient displacement of the third degree-of-freedom, p. 37

k_4 Axial stiffness coefficient displacement of the fourth degree-of-freedom, p. 37

k_5 Axial stiffness coefficient displacement of the fifth degree-of-freedom, p. 37

k_6 Axial stiffness coefficient displacement of the sixth degree-of-freedom, p. 37

k_7 Axial stiffness coefficient displacement of the seventh degree-of-freedom, p. 36

k_I Stiffness coefficient related to impact surface #2, p. 39

k_{Off} Stiffness coefficient related to impact surface #3, p. 39

k_{On} Stiffness coefficient related to impact surface #4, p. 39

k_R Stiffness coefficient related to the rock formation, p. 41

k_S Stiffness coefficient related to impact surface #1, p. 40

m_1 Mass of the first degree-of-freedom, p. 38

m_2 Mass of the second degree-of-freedom, p. 38

m_3 Mass of the third degree-of-freedom, p. 37

m_4 Mass of the fourth degree-of-freedom, p. 37

m_5 Mass of the fifth degree-of-freedom, p. 37

m_6 Mass of the sixth degree-of-freedom, p. 37

m_7 Mass of the seventh degree-of-freedom, p. 36

n Number of impact cycles, p. 102

p_i Number of impacts registered in a given impact surface represented by the subscript i evaluated in a determined number of impact cycles, p. 102

x_1 Axial displacement of the first degree-of-freedom, p. 38

x_2 Axial displacement of the second degree-of-freedom, p. 38

x_3 Axial displacement of the third degree-of-freedom, p. 37

x_4 Axial displacement of the fourth degree-of-freedom, p. 37

x_5 Axial displacement of the fifth degree-of-freedom, p. 37

x_6 Axial displacement of the sixth degree-of-freedom, p. 37

x_7 Axial displacement of the seventh degree-of-freedom, p. 36

Chapter 1

Introduction

1.1 Motivation

In sub-surface drilling, percussive drilling techniques have been an important drilling mechanism since the time of cable tool rigs [1]. The low-frequency, high-energy-level percussive action of cable tools was surpassed in drilling efficiency by the development of rotary rigs and roller cone bits in the beginning of the twentieth century [1]. However, some form of percussive drilling continues to be used today to penetrate hard formations, particularly in mining applications.

A vibration-assisted drilling tool for oil well drilling can be defined as a drilling system that combines the rotary motion (scratching) with a percussive action (indenting). In the oil industry, several prototypes were developed to be used in field applications, such as the Andergauge Drilling Systems hammer [2], the SDS Digger Tools Pty Ltd fluid hammer [3, 4], and the National Oilwell Varco Fluid-hammer [5–8]. Preliminary field test results with these vibration-assisted drilling tools have shown a significant improvement in the rate of penetration (ROP) when drilling hard-rock formations. Thus, this technology has the potential to deliver a step-change in the drilling efficiency when drilling the presalt reservoirs in offshore Brazil where low ROP and short bit-runs are responsible for high-cost operations.

In this context, this work focus on the development of a mathematical model which is able to describe the axial dynamics of a vibration assisted drilling tool developed by Schlumberger. This prototype was submitted to field tests in drilling environment to evaluate and characterize the tool performance. Although this prototype have been successfully tested in field applications, the level of understanding of the physics of vibration-assisted drilling tools is limited because there is no available model to describe the dynamics inside the tool.

1.2 Objectives

The objectives of this work are to: (1) propose a mathematical model to describe the axial vibration of a new vibration-assisted drilling system, (2) validate the mathematical model with experimental data, (3) employ this model to explore the analysis of the impact forces inside the tool, (4) perform a parametric analysis to evaluate how the design parameters (geometry, spring stiffness, excitation force) influences the dynamic behavior of the tool, and (5) propose design modifications for the current vibro-impact system.

1.3 Literature Review

The literature review is divided into three sections to present different perspectives on the development of the vibration-assisted drilling (VAD) technology. A description about the development and evolution of the concept of vibration-assisted systems, as well as the advantages associated with this technology in improving drilling performance for the mining and oilfield industries, is given in section 1.3.1. Next, a brief explanation on the theoretical concepts that were developed to describe and predict the performance of such drilling techniques is presented in section 1.3.2. Finally, from a vibration-assisted drilling perspective, a brief introduction to the complex phenomenon of the cutter-rock interaction, considering experimental and simulation results, is presented in section 1.3.3.

1.3.1 Vibration-Assisted Systems

The vibration-assisted systems section is divided into three subsections: vibration-assisted machining (VAM), percussive drilling and vibration-assisted drilling. The first subsection describes the concept of the vibration-assisted machining, as well as the benefits associated with the VAM technique. The next subsection focus in the concept and application of percussive drilling. Finally, the last subsection analyses the experimental results of three VAD prototypes that were introduced in the oilfield industry to improve drilling performance.

Vibration-Assisted Machining

The vibration-assisted Machining (VAM) combines precision machining with small-amplitude tool vibration to improve the fabrication process. In time, the application of this technique expanded into several different procedures from turning to drilling to grinding [9]. For instance, the emphasis of the VAM includes complex machining applications, such as diamond turning of ferrous and brittle materials. As a

result, this enables the creation of microstructures with complex geometries for the production of molds and optical elements, or for economically producing precision macro-scale components in hard alloys, such as Inconel or titanium.

The main advantage of the VAM is the reduction of the machining forces, as well as thinner chip generation [9]. This, in turn, leads to improved surface finishes, better form accuracy, and near-zero burr compared to conventional machining. Additionally, the tool life is dramatically extended with the application of this technique, especially in the case of diamond tools cutting ferrous materials. When cutting brittle materials, VAM has also been found to increase the depth of cut for ductile-regime cutting, which enables the fabrication of complex optical shapes without grinding or polishing. The initial application of the vibration-assisted machining remotes to the late 1950s for traditional macro-scale metal-cutting applications. In the mid-1980s, the desire to machine materials that were previously not considered diamond-turnable led to significantly greater interest in VAM.

The system parameters of a VAM procedure, such as depth of indentation and oscillation frequency, depends on the application and the desired objectives, which includes improved surface finishing, performance, machining of complicated alloys, and others. In general, the depth of indentation ranges from a few micrometers up to 0.5mm, although the micrometer range tends to be restricted to precision machining applications [9].

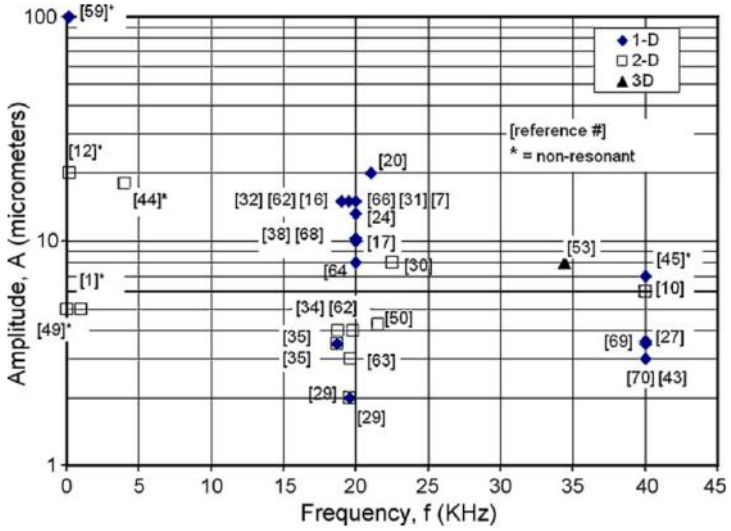

Figure 1.1: Operating ranges for vibration-assisted machining. The amplitude in the y-axis corresponds to the depth of indentation. Numbers inside brackets indicate literature references listed in [9].

Figure 1.1 maps the range of vibration frequency and horizontal amplitude for VAM systems described by technical references given in [9]. The amplitudes range from 2 to 100μm and the frequency from a few Hz to 40kHz, with the majority of

these systems operating around 20kHz. The main advantage of a high vibration frequency is that it allows higher up-feed velocities, resulting in a decrease in machining time.

Experimental data shows a reduction in tool forces in VAM operations when compared with those measured during conventional machining under similar operating conditions [10], as represented in Fig. 1.2. These tool force reductions are observed for a range of tool geometries, ductile, brittle and "hard metal" materials, tool-work material combinations and depths of cut.

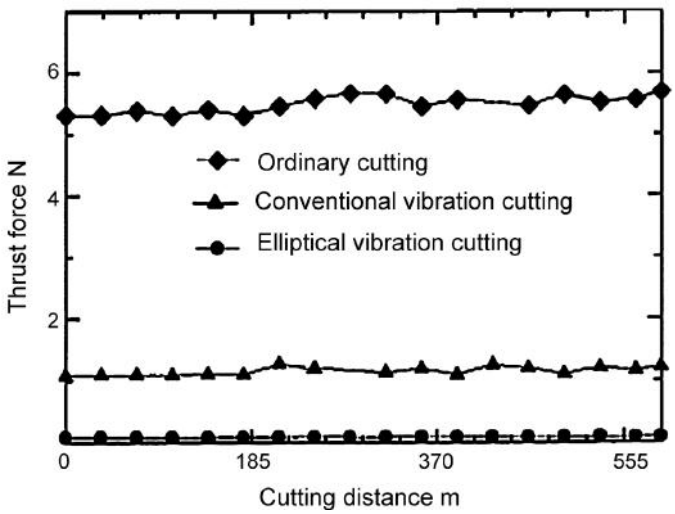

Figure 1.2: Average thrust force comparison for conventional cutting and VAM (named "conventional vibration cutting") for carbide tool in aluminum workpiece at a vibration frequect of 18kHz [10].

The reduced tool forces for VAM appears to be the result of several mechanisms that affects chip geometry, as well as a result of interactions between the tool rake face and the chip as it is extracted from the workpiece, although the precise explanation for this phenomenon is not fully understood [11]. In some VAM applications, the reduction in tool forces are related to the cutting action, which relates to thinner chips formation that are thinner than the ones generated in conventional machining under similar operating conditions. Additionally, in a machining cycle, there are instances where the tool is moving upwards relative to the workpiece. In this scenario, the vertical velocity of the cutting edge can approach – and exceed – the speed of the chip. If the tool is moving faster than the chip, the direction of the friction force is reversed. Thus, in this condition, the friction force pushes the chip away from the workpiece, reducing cutting forces and improving performance. Furthermore, improved lubrication resulting from periodic tool-work separation in VAM has been offered as an explanation for reduced tool forces as well [11].

Another VAM technique found in the literature is the Ultrasonically Assisted

Drilling (UAM) [12]. This method consists of ultrasonic vibrations superimposed onto the relative cutting motion between a drill bit and the work piece, as represented in Fig. 1.3. Usually, this is achieved by excitation of the drill vibration in either torsional or axial vibrations.

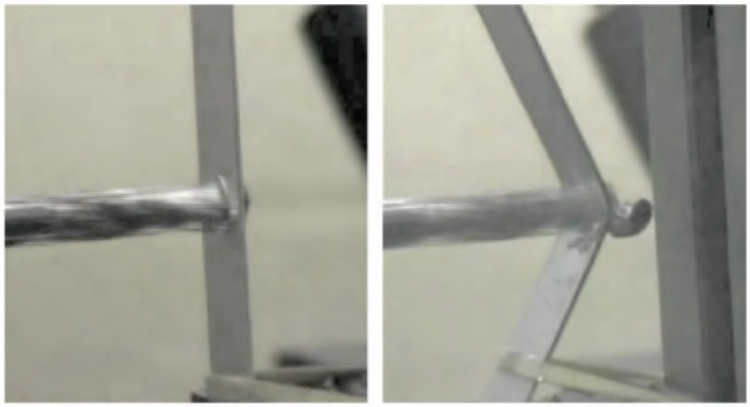

Figure 1.3: Comparison in drilling of flexible aluminum plates: left – ultrasonically assisted, right – conventional drilling [12].

The benefits in drilling performance of the UAM includes: faster penetration rates, as given in Fig. 1.4; reduction of tool wear and improvements in the surface finish; roundness and straightness of holes and; in ductile materials, the reduction or even complete elimination of burrs on both the entrance and exit faces of plates [12]. Additionally, when drilling through flexible thin plates, the reduction in the reactive force greatly reduces the deformation and helps to alleviate delamination hazard, as represented in Fig. 1.3. Therefore, the force reduction highlights observed in UAM are similar to the ones observed in VAM [11].

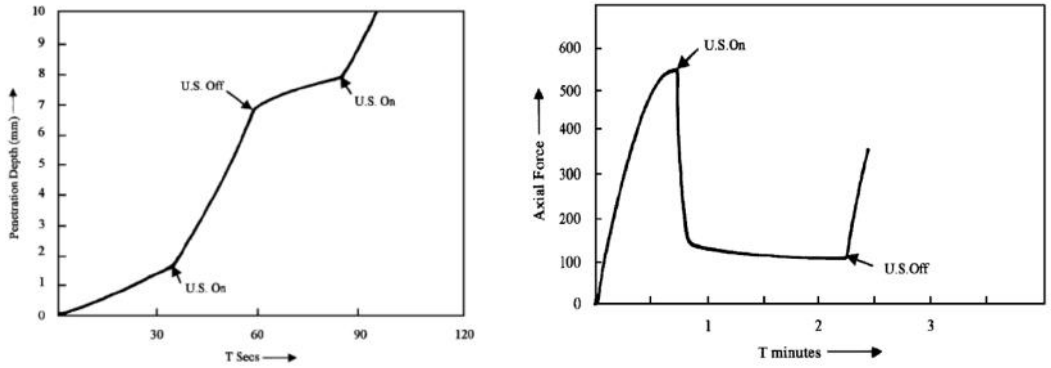

Figure 1.4: Speed of penetration with and without ultrasonic feature caused by the reduction of cutting forces [12].

Brief Introduction to Oil Well Drilling

In rotary drilling, the rock formation is bored using a drill bit, which is rotated and simultaneously forced against the rock formation at the bottom of the hole by a

drill string, as shown in Fig. 1.5a. The cuttings produced by the bit are transported up to the surface by a drilling fluid (oil-based mud or water-based mud) circulated into the wellbore. After a certain depth is reached, the drill string is removed from the borehole. Next, sections of steel pipes, called casings, are cemented in place during the construction process to stabilize the wellbore. These casing forms a major structural component of the wellbore and provides a means of maintaining control of formation fluids and pressure as the well is drilled [13].

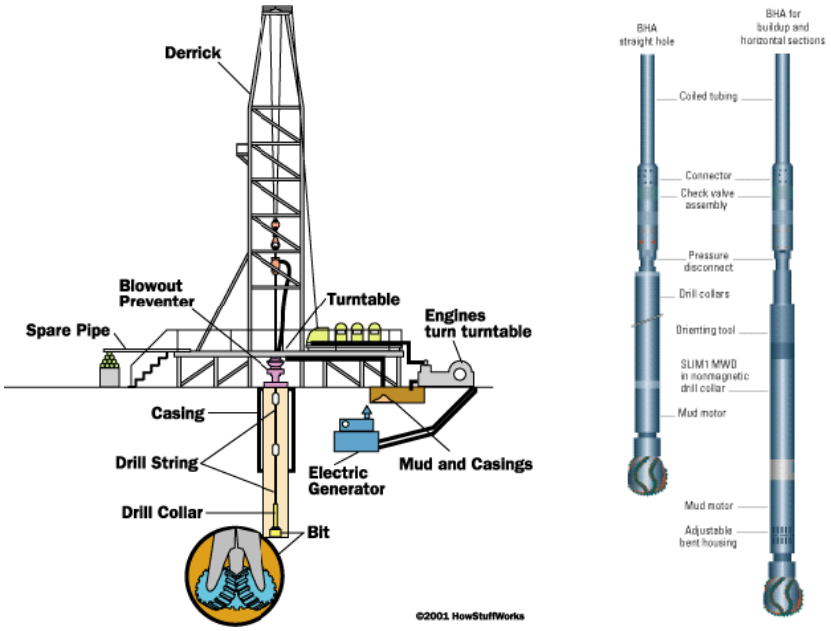

(a) (b)

Figure 1.5: (a) Sketch of a drilling rig [14] and (b) Sketch of the main components of a bottom hole assembly [13].

The drill string is an assemblage of drill pipes and drill collars, extending from the surface to the bottom of the hole. The drill collars (thick-walled) and the drill pipes (thin-walled) are tubular steel conduit fitted with special threaded ends called tool joints. These components are responsible for connecting the surface equipment with the end of the drill string (bottom hole assembly), as well as responsible for the circulation of the drilling fluid to the bottom of the hole [13].

The bottom hole assembly (BHA) is the assembly of heavy drilling tools at the end of the drill string designed to survive a hostile mechanical environment and provide the driller with directional control of the well. A typical BHA includes a drill bit, stabilizers and drill collars, as shown in Fig. 1.5b. Oftentimes the BHA may contain other specialized tools, such as a down hole motor, directional drilling systems, measurements-while-drilling tools (MWD), logging-while-drilling tools (LWD) [13].

Percussive Drilling for Oil well Drilling

Percussive drilling techniques have been an important drilling mechanism since the time of cable tool rigs [1]. The low-frequency high-energy-level percussive action of cable tools was surpassed in drilling efficiency by the development of rotary rigs and roller cone bits in the early 1900's. However, some form of percussive drilling continues to be used today to penetrate hard formations, particularly in mining applications.

The principle of percussive drilling is based on the proposition that the optimum way to drill hard rock would be to have high-energy loads per cutter and a rotary action that would move the cutters to "new" unfractured formation between each successive load, This is precisely the goal of the air hammers that have been used in the mining industry since the early 1900's, which were commonly referred Down-the-Hole (DTH) Hammers. However, not until the 1960's that a low-frequency high-energy hammer was introduced into the oilfield industry. These hammers were first attached to roller cone bits in an effort to increase penetration rate over conventional WOB/rotary applications in large surface holes [1].

Traditionally, these percussive hammer tools are pneumatic, which defines that circulating system must use air (or air-based). This factor can be seen as both an an advantage and a limitation of the percussive drilling, as the formation pressure control is minimal and drilling is restricted to geological regions where reservoir pore pressures are low, i.e., drilling is limited to geological regions where the rock formations are mature and competent because there is little or no fluid pressure to support the borehole wall and prevent sloughing [1].

Percussion downhole hammers are primarily used to improve penetration rate in medium to hard formations [1]. They can also be used effectively in drilling softer rock formations, wherever air or foam systems can be used. The downhole hammer is less effective in unconsolidated formations such as clay, sand, or gravel for which roller cone bits are better suited. The bits designed specifically for percussive drilling applications present no cutting mechanism, only indentation.

Additionally, bit weight, rig size, torque loads and rotation speeds can be reduced when compared to rotary drilling. For example, a rotary bit may require 5,000 pounds of weight-on-bit (WOB) per inch of bit diameter. Downhole hammer bits require only 200 to 500 pounds of WOB per inch of bit diameter [1].

Torque loads and rotation speeds are much lower in downhole hammers than rotary bits. A rotary speed of 10 to 60 RPM allows the inserts to penetrate new formation after each blow. The piston drives its energy through the bit and into the formation. After fracturing occurs, the inserts are rotated to a new position. Bit rotation should also be as slow as possible to maintain a smooth operation with as

little torque as possible.

It has been widely recognized that percussive drilling (even without rotary assistance) can result in higher penetration when compared to conventional means such as rotary drill or diamond drill in hard formations, such as siliceous granite, sandstone, limestone, dolomite. This advantage is mainly due to the effects of frequent blows and high impact loads through bit teeth, as well as chipping of rock from a clean surface with the bit rotation [15].

Vibration-Assisted Drilling

Different to percussive drilling, when the rock failure is achieved through cutter indentation, in vibration assisted drilling (VAD) both cutting mechanisms are in action (indentation and cutting).

Andergauge Hammer (1996)

In 1996, Andergauge started the development of a fluid hammer tool for oilfield applications [2], as represented in Fig. 1.6. The technology consists of a rotating valve system that alternately directs fluid to a piston that drives down a steel mass to strike the rear of the bit and then to a port that bypasses the piston. This action allows the mass to return to its original position for the next downward stroke [2].

The tool was land tested in Norway in a series of three tests with similar rock formation (granite). The drilling condition for these three tests included a water based drilling fluid to be used with roller cone bits. The hammer tool (6.75in in tool diameter) developed 80klbf strokes at 8Hz using roller cone bits. The results recovered from tests 1 and 2 were unable to reach a satisfactory increase of ROP, which undermines the usage of this prototype in those conditions. However, the last test showed a 100% increase in ROP for the first drilling hour, followed by a drop in ROP due to tool failure (seal leakage).

In original design of the Andergauge hammer, the piston displacement range was 18mm, which translated in a 20% gain in ROP in the field tests. In the following prototype, there were design modifications on the displacement range of the impacting mass. Thus, the piston displacement range was increased to 50mm, which translated in a 100% ROP gain in the last field test [2].

The analysis of the hammer designs and the field tests results suggests a correlation between the increase in the piston displacement and the increase in the impact force [2]. Furthermore, it appears that there is a frequency restriction to values under 10Hz due to hydraulic limitations of piston chamber and the return spring.

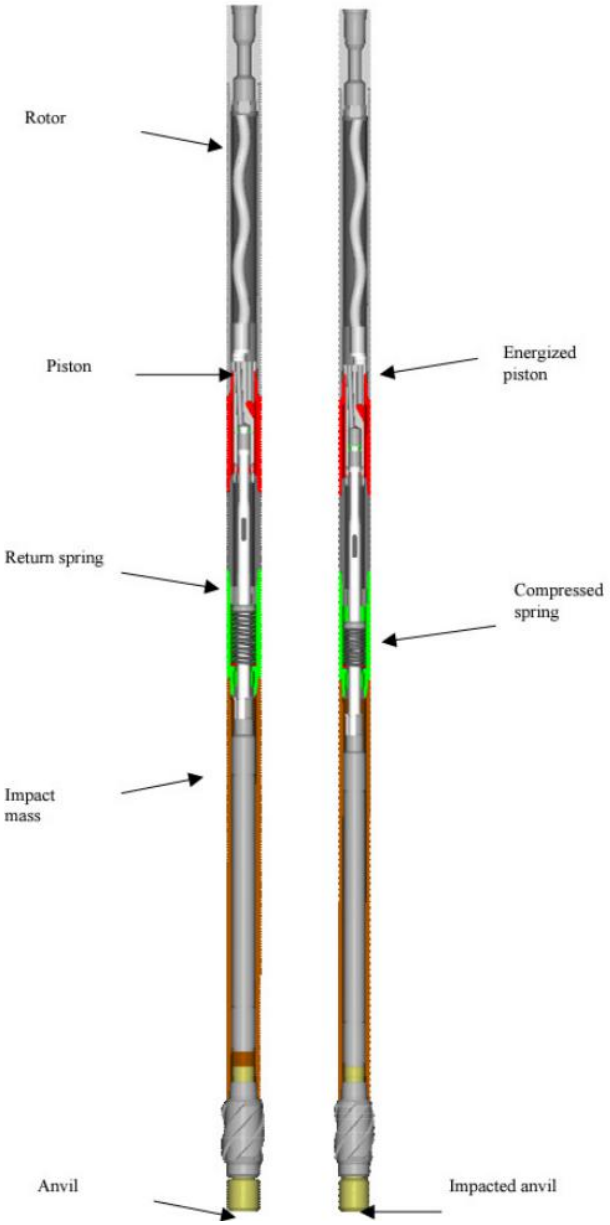

Figure 1.6: Sketch of the Andergauge Hammer design, [2].

The Andergauge hammer was also submitted to tests in a closed flow loop system to measure the impact forces in a controlled environment [2]. The impact force measured over time is shown in Fig. 1.7. According to PLACIDO *et al.* [2], the impact forces obtained in the experimental data did not capture the actual behavior of tool, as the measurement devices exhibited a low acquisition sampling frequency. The experimental results indicate that a higher sampling rate is required to reproduce the actual behavior of the impact forces. For instance, a viable solution could be selecting a different measurement device with an acquisition frequency in the order of kHz, assuming that the impact phenomenon occurs in a millisecond time window [11].

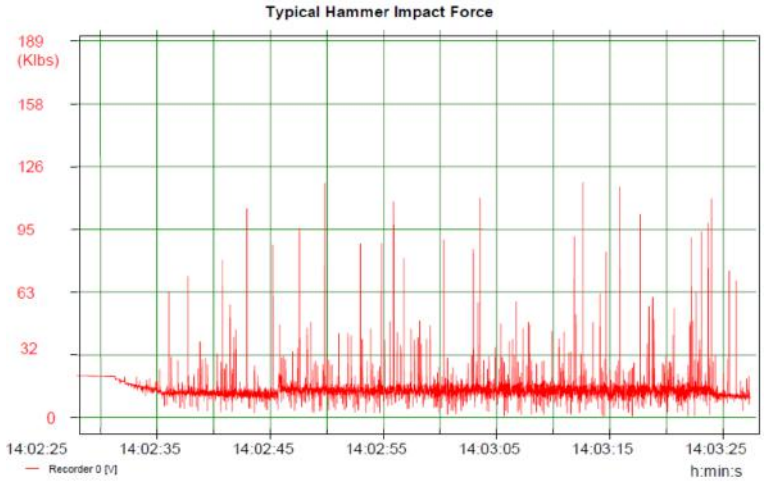

Figure 1.7: Hammer impact force. According to the authors the impact pulses appear irregular on the chart due to lack of acquisition sampling [2].

The performance charts of the hammer tests shown in Fig. 1.8 correlate the value of the weight-on-bit with the correspondent ROP. The data seems to indicate that there is a minimum WOB threshold required to produce a significant increase in ROP. However, for high values of WOB, the percussive action seems to be undermined by the conventional drilling, as its contribution to ROP decreases. Thus, the experimental data seems to indicate an operating WOB condition where the hammering action contributes the most for the ROP, ergo, a "sweet spot" for the percussive action [11].

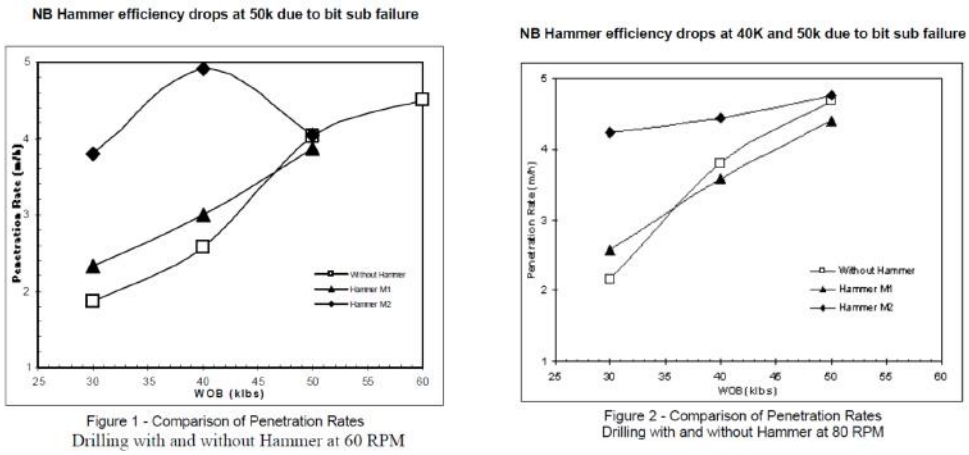

Figure 1.8: Hammer tests performance comparison [2].

SDS Digger Fluid Hammer (2002)

This fluid hammer tool was developed by SDS Digger Tools Pty Ltd. and tested in field conditions by Petróleos de Venezuela, S.A. (PDVSA) in Eastern Venezuela using a 12.25in roller cone bit [3]. The lithology drilled was the top of Barranquín Formation, with unconfined compressive strength (UCS) between 20 and 30 kpsi.

The sandstone content was over 80% and highly consolidated and very abrasive. LAGRECA *et al.* [3] did not reveal information regarding the operating mechanism of the fluid hammer. The drilling conditions included 11 to 20klbf of WOB and 15 to 30 rotations per minute (RPM). Although it reached in few intervals instant of ROP levels higher than offset wells, the average ROP (4 ft/hr) was lower than average of the offset wells (5.5 ft/hr).

In 2002, a consortium of Department of Energy, operator and industry participants put together an effort to test and optimize mud driven fluid hammers as one emerging technology, as this technology had shown promising results that seems to indicate an increase penetration rates in hard rock [4]. The focus of this program had been to test and record the performance of fluid hammers in full scale test conditions, in Terratek, including: hard formations at simulated depth, high density/ high solids drilling mud, and realistic fluid power levels, refer to Fig. 1.9. These tests included: two 7.75in diameter fluid hammers coupled with 8.5in diameters drill bits. These fluid hammers were tested with several bit types, with performance being compared to a conventional roller cone bit. These tools functionally operated in all proposed downhole environments that emulated an actual drilling environment. The experimental data reveals that the performance of both fluid hammers were within the baseline range of roller cone or better at lower borehole pressures, however, at higher borehole pressures, the performance was within the lower range or below roller cone bit baseline.

Figure 1.9: Terratek test facility where the tests with the SDS Digger Hammer were performed and two of the bits used in these tests. [4].

NOV Fuild Hammer (2011-2013)

This fluid hammer tool was developed by NOV and tested in field conditions by Petrobras in São Francisco Basin (Brazil) using a 9.5in tool in a 17.5 diameter section in exploratory vertical well [5].

The offset wells performance consisted of 2.1m/h of ROP while drilling in a rock formation composed of shale with interbedded siltstone, hence a lithology that is considered both hard and abrasive. The Hammer drilled 115m with an average ROP of 3.2m/h, which indicates a 50% improvement in both ROP and footage using a roller cone bit. The drilling parameters in this drilling operation consisted of 35klbf of WOB and a mud flow rate of 700 gallons per minute (GPM).

NOV continued the development of the Fluid Hammer tool in China [6–8]. The drilling operations were performed in an inland site at Tarim field, west China, in vertical wells. Additionally, the lithology in these test areas consisted of sandstone, limestone and anhydrite. The drilling operations were performed using fixed cutter bits. The offset wells presented an average ROP in the range of 1.7 to 1.9m/h. The results from the case studies using the Fluid Hammer Tool revealed improvements in ROP, such as 7.7m/h in one scenario and 6m/h in a second test, as well as showed improvement in meters drilled per run.

Neither HERRINGTON *et al.* [7], HERRINGTON *et al.* [6] or POWELL *et al.* [8] provided information on the fluid hammer characteristics, such as impact frequency and impact forces, nor on the drilling parameters (WOB, RPM, GPM, etc.).

1.3.2 Vibro-Impact Modeling

The vibro-impact modeling section is divided into two subsection: impact theory and vibro-impact models. The first subsection defines the concepts of impact and contact forces. Moreover, this subsection explores the advantages and limitation of three impact forces models: Hertz model, spring-dashpot model and Hunt-Crossley model. The subsection section focus on vibro-impact mathematical models, such as impact oscillators models, vibro-impact drilling models and vibration-assisted drilling models.

Impact Theory

An impact can be defined as a complex physical interaction between two or more bodies that undergo one or more collisions between themselves [16]. The main properties of the impact phenomenon can be simplified into four characteristics: quasi-instantaneous interaction, high forces generated from this interaction, rapid energy dissipation (see Fig. 1.10), and considerable acceleration variation [17]. These characteristics varies according to the material properties of each body that undergoes an impact, as well as geometrical discontinuities. In contrast, the definition of contact is a more ambiguous term. In that sense, the usage of the term contact implies a continuous process, which takes place over a finite time, where two or more bodies come in touch with each other at some locations [17].

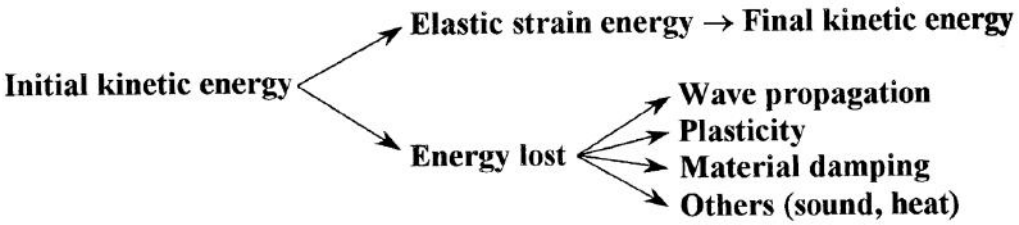

Figure 1.10: Energy flow associated with normal direction of impact [17].

Although the definition for both impact and contact reveals some intrinsic dependency, there are two general approaches that distinguish a contact analysis from an impact analysis regarding the collision among multiple bodies. The first analysis, named impulse–momentum or discrete methods, assumes that the interaction between the multiple bodies is quasi-instantaneous and that there is no significant change in configuration of the impacting bodies [18]. The second approach, referred to as continuous analysis or force based methods, considers that the interaction forces is continuously applied throughout the whole impact interaction [18].

There are some limitations associated with the application of discrete methods (impulse-momentum) in the modeling of the impact dynamics of rigid bodies [17]. In relation to the Coulomb friction methodology, the application of this method under certain conditions could result in a set of differential equations that have multiple solutions or does not even have a solution [19]. Additionally, STRONGE [20] reveals that there is a possibility of violation of the principles of conservation of energy in frictional impacts. Moreover, the continuous contact models are more easily extensible to generic multi-body systems, since the modeling of the impact force as a function of local indentation (continuous analysis) bypasses the intrinsic limitations of discrete methods [19]. It is worth mentioning that the main advantage of the continuous contact dynamics analysis is the possibility of selecting between several friction models available in literature.

Furthermore, the contact stiffness and the damping forces show dependence to at least two parameters, such as the coefficient of stiffness and the coefficient of damping [17]. In general terms, the coefficient of stiffness is related to the material and the geometry of the bodies that are in contact, while the coefficient of damping seems to be related to the coefficient of restitution.

The description of the interaction force between contacting objects has been extensive analyzed theme, since there were several contact force models developed over the years [16]. Among those models, there are three established contact force models in literature: the Hertz model [21], the Kelvin-Voigt model (spring-dashpot model) [22], and the Hunt-Crossley model [23].

The first model considers that the local indentation of the interaction between two contacting bodies can be modeled using elastostatic theory, considering only as elastic force without any energy dissipation [21]. Additionally, this impact force model allows a nonlinear relationship between the local indentation and the contact force. The second model introduces a linear damping force that is proportional to the rate of indentation between the two contacting objects [22]. This impact force model is named Kelvin-Voigt, or spring-dashpot model, also assumes a linear correlation between the indentation and the impact force. The third impact force model proposes a nonlinear damping force, based on the Hertz model of elastic contact force, that considers both the indentation and the rate of indentation to calculate the total dissipating force [23]. Furthermore, the results show that the linear damping force model derived from the Kelvin-Voigt model does not accurately represent the physical phenomena of an impact force, thus the nonlinear damping force is introduced to retain physical consistency [23].

A detailed analysis of these three impact forces are presented below.

Hertz Model

The continuous contact model proposes a nonlinear relationship between the impact force and the deformation of the contacting bodies [21]. This model assumes a purely elastic impact interaction, which does not include energy dissipation mechanisms. Thus, the impact interaction can be modeled as a nonlinear spring, which represents the contact surface of the two bodies that undergo a collision. Hence, the impact force obtained from the Hertz model is represented in Eq. (1.1).

$$F_I = k\delta^n \tag{1.1}$$

where k and n are constants, whose values are related to material and geometric properties and computed by using elastostatic theory. For instance, in the case of two spheres in central impact, $n = 1.5$ and k is defined in terms of Poisson's ratios, Young's moduli and the radii of the two spheres [24].

It is important to emphasize that the Hertz model assumes that the deformation of the colliding bodies is concentrated in the vicinity of the contact surface, neglecting the elastic wave motion effect [17].

Kelvin-Voigt Model

The Kelvin-Voigt model also known as spring-dashpot model, introduces a linear damping force that is proportional to the rate of indentation between the two contacting objects [22]. Additionally, this model assumes that there is a linear relationship between the indentation and the impact force. Thus, the impact interaction can be represented by a linear damper, which is the dashpot component

responsible for energy dissipation, associated in parallel with a linear spring, which is responsible for the elastic behavior. Therefore, the impact force is defined by Eq. (1.2).

$$F_I = k\delta + c\dot{\delta} \tag{1.2}$$

where k is the impact stiffness coefficient and c is the impact damping coefficient.

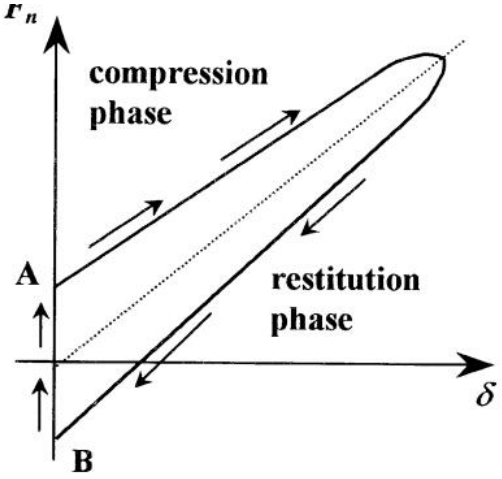

Figure 1.11: Contact force history for the Kelvin-Voigt model [17].

A visual representation of the contact force history for model, which is represented in Fig. 1.11, reveals two limitations regarding the impact dynamics physical consistency [22]. First, the contact force is discontinuous at the initial stage of impact (point A), due to the damping component of the impact force. In a more realistic model, both elastic and damping terms should be initially at zero and gradually increase over time. Secondly, as the objects loose contact (point B), i.e., the indentation tends to zero, their relative velocity tends to be negative, which translates into a negative force that holds the objects together.

Although the spring-dashpot model is not physically consistent, its simplicity has made it a popular choice for modeling the impact interation in various vibro-impact models [25–29]. It provides a reasonable method for capturing the energy dissipation associated with the normal forces without explicitly considering plastic deformation issues.

Hunt-Crossley Model

The Hunt-Crossley model was developed with an intent to overcome the limitations of the spring-dashpot model and still be able to retain the advantages of the Hertz's model [23]. This model, named Hunt-Crossley model, expands the Hertz contact model by introducing a non-linear damping term, which follows a similar behavior of the elastic term. The comparison between the contact force history for

the Kelvin-Voigt model and the Hunt-Crossley model is represented in Fig. 1.12. The impact force model is described by Eq. (1.3).

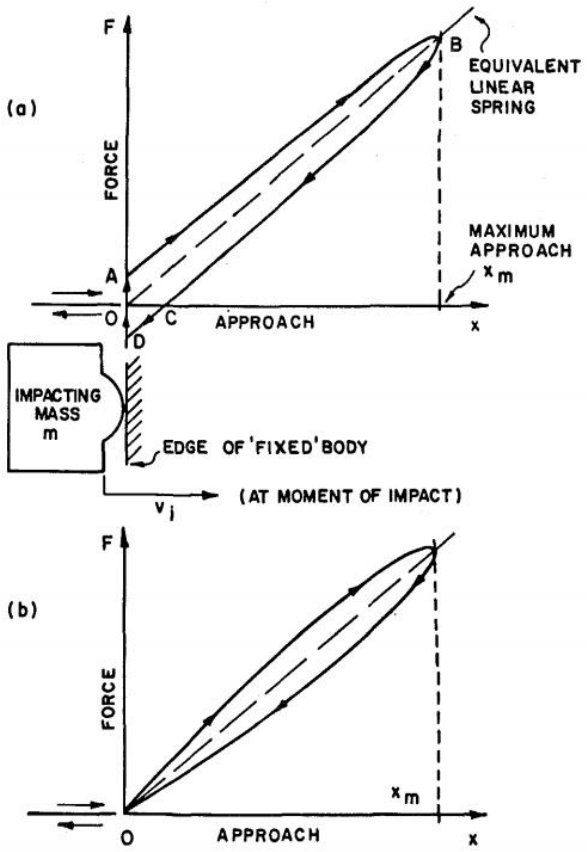

Figure 1.12: Contact force history for both the Kelvin-Voigt model (a) and the Hunt-Crossley model (b) [23].

$$F_I = k\delta^n + c\dot{\delta}^q\delta^p \tag{1.3}$$

where k is the impact stiffness coefficient and c is the impact damping coefficient. The parameters n, p and q are constants whose values are related to material and geometric properties. It is a common practice to set p equal to n and assume that q is equal to 1.

The Hunt-Crossley model solves the continuity limitation of the Kelvin-Voigt model by including an indentation dependence on the damping term of the impact force [23]. This results in a more physically consistent model, as the contact surface area increases with the indentation and a plastic region is more likely to develop for larger indentations. Furthermore, this model presents no discontinuities at the initial contact phase and at the separation phase, as it assumes a value of zero in both the initial and the final stage of the impact interaction.

Finally, with these three impact forces introduced, an important discussion arises regarding the difference of each impact force model in the dynamic behavior of a

given system. Thus, a local dynamics analysis, as described in AJIBOSE *et al.* [30], indicates that, in the case of a one degree-of-freedom drift impact oscillator, all three models result in almost identical dynamic behavior. Hence, the Kelvin-Voigt model seems to be an acceptable candidate for a first approach to model the impact interaction.

Vibro-Impact Dynamic Models

PAVLOVSKAIA *et al.* [25] developed a physical model to examine the dynamic behavior of impact oscillators. This model consisted of a two degree-of-freedom system that accounts for the viscoelastic impacts and is capable to mimic the dynamics of a bounded progressive motion through the usage of a dry frictional slider, see Fig. 1.13. The parameter values for this model were selected to induce the stick-slip phenomenon, which is the phenomenon responsible for the progression rates.

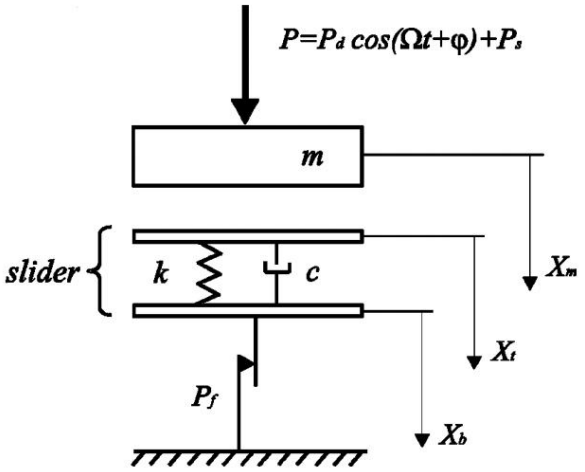

Figure 1.13: Sketch of the physical model for the impact oscillator, adapted from [25].

The results of the nonlinear dynamic analysis of this model revealed a complex behavior ranging from periodic to chaotic motion. Moreover, the bifurcation diagrams were constructed using variation of the mass velocity as the displacement has a drift. The results revealed that the maximum progression coincided with the end of periodic regime and the beginning of chaotic motion, after a cascade of sub-critical bifurcations to period one. An explanation for this behavior seems to be related to the phase difference when the mass and the slider are in contact and out of contact [29].

Additionally, a further analysis conducted by PAVLOVSKAIA *et al.* [28] explores the same vibro-impact model with the addition of the soil resistance curves. The

results reinforce the idea that the maximum progression rate coincides with the end of periodic regime.

An approach by CAO *et al.* [31] investigated the nonlinear dynamics of a modified physical model of vibro-impact drilling system represented in Fig. 1.13. The reduced model without non-holonomity is derived by the introduction of a new state variable, of which averaging technique is employed successfully to detect the periodic motions. The results from the numerical simulations show that the efficiency of penetration depends on the ratio between the static force and the dynamic force. The maximized penetration can be achieved when this ratio (b/a) is close to 0.5, which is within the periodic region, as represented in Fig. 1.14. The penetrating rate appears to decrease when this ratio is low, which corresponds to the region where the chaotic motions coexist.

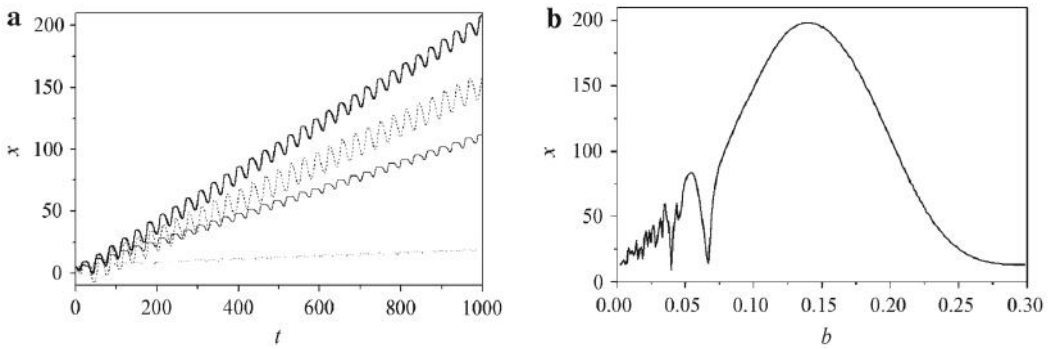

Figure 1.14: (a) Displacements of the mass, assuming $a = 0.3$ (dynamic force coefficient), x versus time, t with different values of parameter b (static force coefficient) at $b = 0.15$ (bold solid), $b = 0.2$ (dashed), $b = 0.1$ (thin solid) and $b = 0.25$ (dotted). (b) Total penetration, x against parameter, b over the 1,000 seconds [31].

FRANCA e WEBER [26] investigated the drilling technique called resonance hammer drilling, see Fig. 1.15.

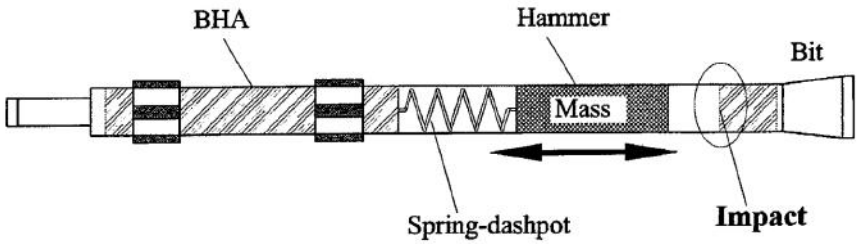

Figure 1.15: Ressonance hammer drilling concept sketch [26].

The basic concept of this technique consists of usage of the already existent axial vibration from the cutting process to generate a harmonic load on the bit and an excitation in a steel mass (hammer). When this excitation frequency approaches

resonance frequency of the hammer, the system is designed to induce impacts on the bit, since the steel mass displacement is limited by the gap. Therefore, besides the rotary penetration, where the teeth of the bit penetrate in the rock when the drill string rotates, a percussive penetration happens due to the harmonical load or due the impact action.

The mathematical model developed considers only the percussive action of the resonance hammer. Furthermore, a simple model for the longitudinal behavior of the bit–rock interface is proposed and the drilling resistance is modeled by a dry friction element, refer to Fig. 1.16. Moreover, the model presented in this work moves forward (a drift) in stick–slip phase with or without impact. The results of this mathematical model are compared with experimental data obtained from a test rig that emulates a percussive drilling environment with and without impact.

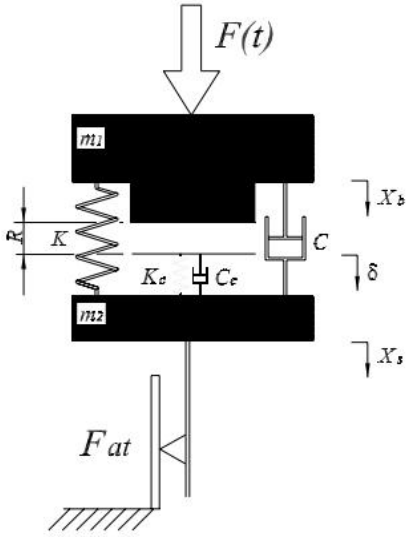

Figure 1.16: Sketch of the physical model for the resonance hammer [26].

The results show that the numerical and experimental investigations presented are qualitatively and quantitatively similar. Additionally, the dynamic analysis of the model exhibits a complex behavior, which including periodic and chaotic types of motion [26]. Furthermore, the results revealed that the best operating condition for the static loading coincides with the region that exhibits periodic behavior, which is consistent with the results of the previous vibro-impact models [25, 28, 29].

Further nonlinear analysis, performed by PETERKA *et al.* [32], focus on the explanation of the intermittency chaos appearance of the impact oscillator (see Fig. 1.17), since this vibro-impact model is a deterministic system and exhibits chaotic behavior. It is caused by the strong non-linearity of the impact motion and corresponding instabilities of periodic motions.

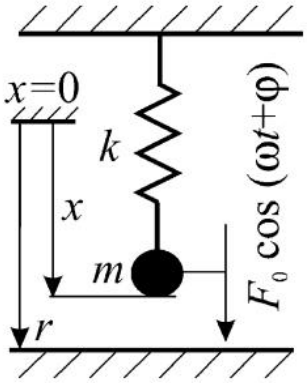

Figure 1.17: Impact oscillator model [32].

Additionally, the impact motion, defined by PETERKA *et al.* [32], is characterized by quantity $Z = p/n$, where p is number of impacts and n is number of excitation periods T in motion period. Quantity Z has rational and irrational value for periodic and chaotic motion, respectively. The parameter Z expresses mean number of impacts in one period T.

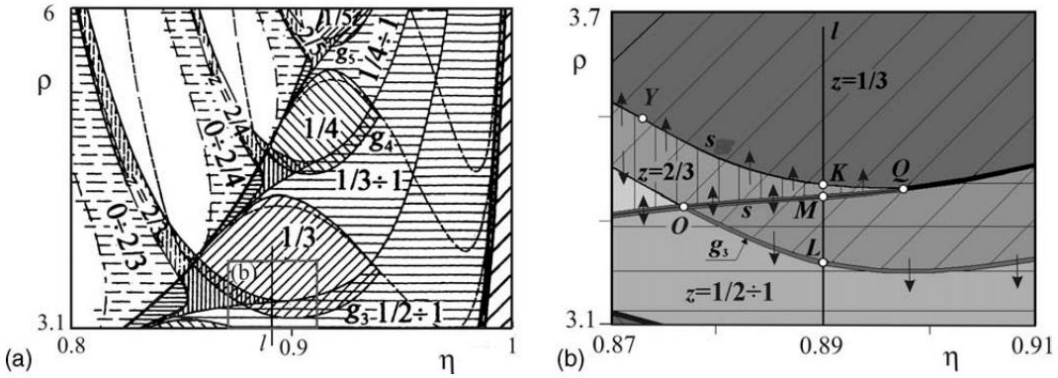

Figure 1.18: Regions of existence and stability of different periodic and chaotic impact motions. Regions of $Z = 2/3$ and $Z = 1/3$ motions exist in subregion (b) in (a). It is enlarged in (b), where regions both periodic motions $Z = 2/3$, $1/3$ and chaotic motion $Z = 1/2$ to 1 are hatched [32].

The results show that the chaotic motion of an intermittency type of the impact oscillator appears near segments of saddle-node stability boundaries of sub-harmonic motions with two different impacts in motion period, which is n multiple ($n \geq 3$) of excitation period, as detailed in Fig. 1.18. The cause for this phenomenon seems to be related with the appearance of additional impact, which interrupts the saddle-node instability development and initiates the chaotic motion of intermittency type.

AGUIAR e WEBER [27] developed an experimental investigation and the corresponding mathematical modeling to validate the impact force behavior of a vibro-impact system, where an elastically mounted hammer impacts inside a cart that vibrates under a prescribed displacement, see Fig. 1.19.

The test rig considers different values for the impact gap, the hammer stiffness and the excitation frequency. Thus, by changing the hammer parameters the impact force behavior is investigated for cart frequencies in a given range. Furthermore, certain behavior patterns of the impact force were observed, allowing the definition of frequency bands presenting similar characteristics according to the gap imposed between the neutral position of the hammer and the impact point on the cart. Inside the bands the impact force behavior presents a regular pattern while in the transition regions between adjacent bands the hammer shows a nonlinear behavior, as basins of attraction, jump phenomena and even chaotic behavior.

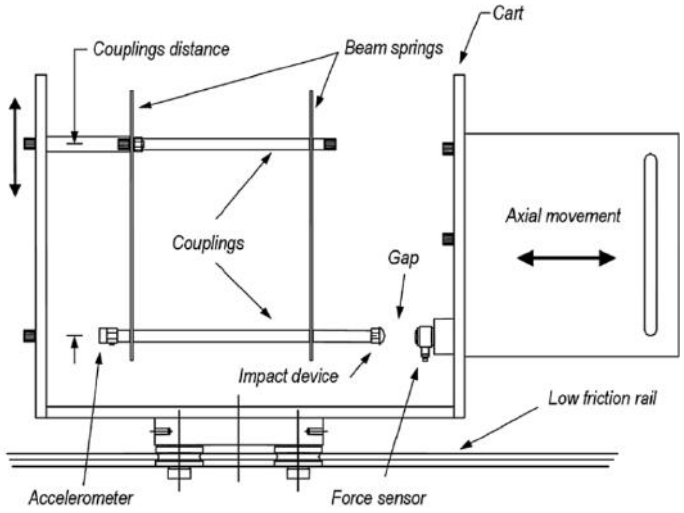

Figure 1.19: The experimental rig sketch that represents a main cart which slides along the horizontal axis on a low-friction rail bearing assembly, adapted from [27].

Similar to [32], AGUIAR e WEBER [27] defined Z, the characteristic of impacts, as a fraction where the numerator indicates the amount of impacts and the denominator indicates the excitation cycles. For instance, for an impact behavior of one impact per one excitation cycle, $Z = 1/1$.

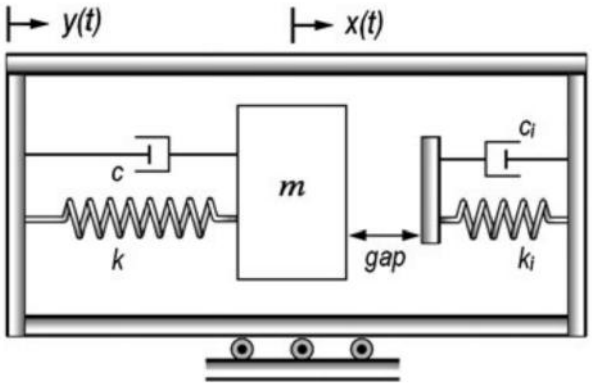

Figure 1.20: Mathematical model proposed for the physical represention of the experimental rig [27].

The mathematical model developed to validate the experiments, as represented in Fig. 1.20, is capable of determining qualitatively the frequency bands and predicting the impact force magnitude in the frequency domain for each stiffness/gap combination. However, the mathematical model did not predict well the hammer displacement, due to the energy used in the bending vibration modes of the beam springs, which support the hammer, following each impact.

To better visualize the behavior of this dynamical system, AGUIAR e WEBER [27] proposes a nonlinear tool, named Peterka map. This technique shows a map of regions of stable impact behavior, which provides information about the characteristic of the impact force as the gap is varied and the range of excitation frequencies is covered, as described by Fig. 1.21. From this chart one can see the areas where the two frequency bands occur, as noted by the red (Z = 1/1) and green (Z = 1/2) areas.

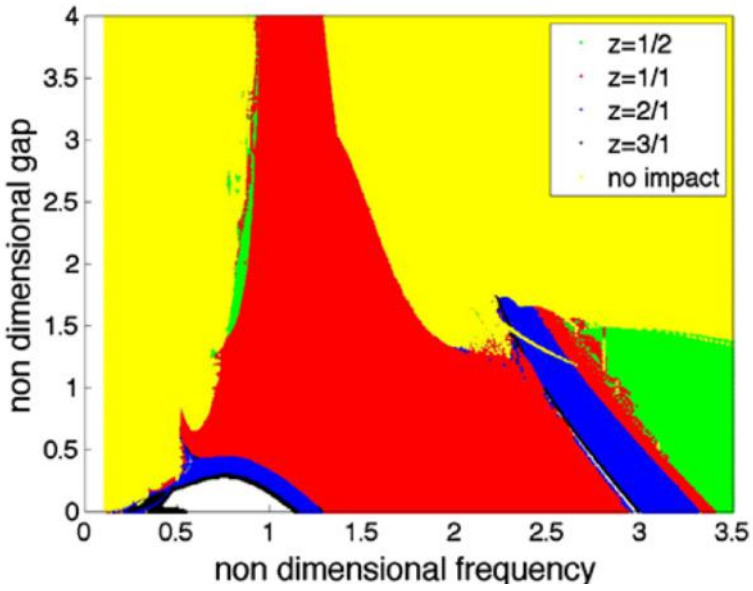

Figure 1.21: Peterka map of $Z = 1/1$ with impact force magnitude, adapted from [27].

Although the map of regions of stable impact behavior (Peterka map) provides important information about the condition of impact, no information regarding the impact magnitude is given. To overcome this problem, a slight variance of the Peterka map is suggested [27], which introduces the impact force amplitude, F_i, as a third coordinate represented in a color gradient, as represented in Fig. 1.22. Since, the relevant impact condition is established as $Z = 1/1$, only this are in the Peterka map is addressed.

By observing experimental data and modeling results using nonlinear tools, AGUIAR e WEBER [27] proposed a recommendation, regarding the gap range,

that one should operate with a 0.0 mm gap, because the magnitude of the impact forces was in the same range as the impact force using higher gap values. However, with higher gap values it was observed a nonlinear jump which will demand a careful tuning of the frequencies.

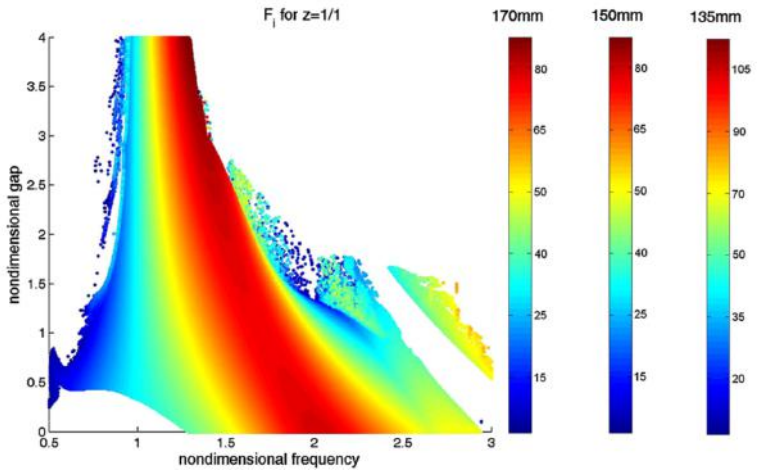

Figure 1.22: Peterka map indicates that there are regions where the two frequency bands occur, as noted by the red ($Z = 1/1$) and green ($Z = 1/2$) areas [27].

1.3.3 Cutter-Rock Interaction in Percussive Drilling

Due to the complexity of the cutter-rock interaction, the focus of this section is to give a brief introduction to the failure mechanism observed in the rock formations submitted to percussive drilling. This failure mechanism is called failure by indentation, which is a typical mechanism for roller cone bits, as well as the major rock failure mechanism for percussive bits.

LIU *et al.* [33] developed a rock and tool interaction code, namely, R-T2D, to simulate the fracture process indenting heterogeneous brittle materials. Rock fragmentation processes induced by single and double indenters were examined by this numerical method. The heterogeneous rock was modeled based on statistical theories and rock characteristic properties. The simulated results reproduce the progressive process of rock fragmentation in indentation, see Fig. 1.23 .

Rock deforms elastically at the initial loading stage. A fan-shaped stress field is radiated outside the highly stressed zone (see Fig. 1.23A). As the stress intensity builds up with an increasing load (see Fig. 1.23B), one or more of the flaws nucleates a crack around the two corners of the truncated indenter. It is interesting to find that, although the rock immediately beneath the indenter is highly stressed, it does not fail primarily because of the high confining pressure. The cone cracks lose their symmetrical shapes because of the rock heterogeneity. With the loading displacement increasing (see Fig. 1.23C), the cone cracks driven by tensile stresses run downward along the stress trajectories of the maximum principal stresses. Then,

tensile cracks are initiated around the two corners of the truncated indenter and propagate. The rocks immediately under the indenter are in a highly tri-axial stress state, and some of them fail in the ductile mode. With the tensile cone cracks and ductile failure releasing the confining pressure, the rocks under the indenter are compressed into failure and the crushed zone gradually comes into being (see Fig. 1.23D).

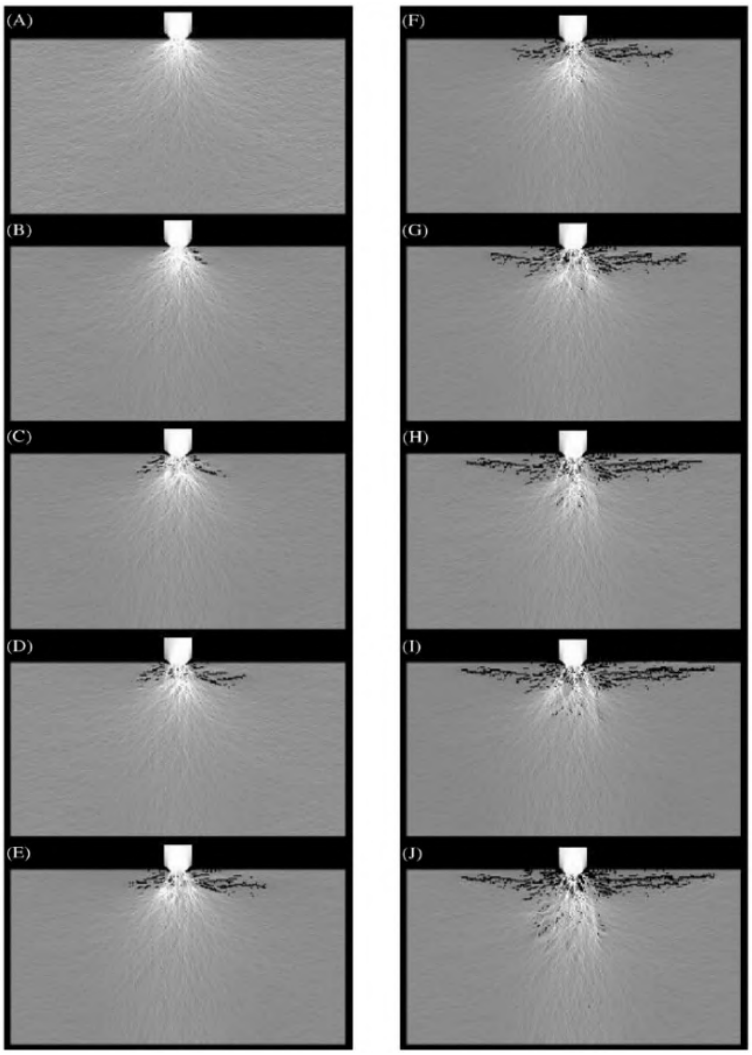

Figure 1.23: Simulated results for rock fragmentation process induced by single indenter [33].

With increasing loading displacement, the re-compaction behavior of the crushed zone occurs. Side cracks initiated from the crushed zone or bifurcated from cone cracks are driven by tensile stress associated with the crushed zone to propagate in a curvilinear path and finally intersect with the free surface to form chips (see Figs. 1.23E-F). As the penetration displacement increases, the side cracks on both sides of the indenter propagate stably to form almost symmetrical shapes. At the same time, some discrete cracks initiate under the crushed zone and are expected to form

median cracks (see Figs. 1.23G-H). With the loading displacement increasing, the side crack on the right side of the indenter accelerates and propagates unstably to form chips (see Fig. 1.23I). As the loading displacement increases, the side crack on the left side of the indenter is expected to form chips also. At the same time, more discrete cracks initiate under the indenter. Some of them coalesce to form subsurface cracks (see Fig. 1.23J). Apparently, optimum loading for such situation is where the first cracks intersect the free surface to form chips along with the formation of what LIU *et al.* [33] call median cracks, where exists a peak in formation damage (see Figs. 1.23F-G).

Additionally, the simulated results for the rock fragmentation process induced by double indenters, [33], is given in Fig. 1.24. Simultaneous loading using multiple indenters with an appropriate line spacing seems to provide a possibility of forming larger rock chips, controlling the direction of subsurface cracks and consuming a minimum total specific energy. In the following, the rock fragmentation process induced by two indenters simultaneously is simulated to see how the side cracks propagate, interact and coalesce to form large rock chips.

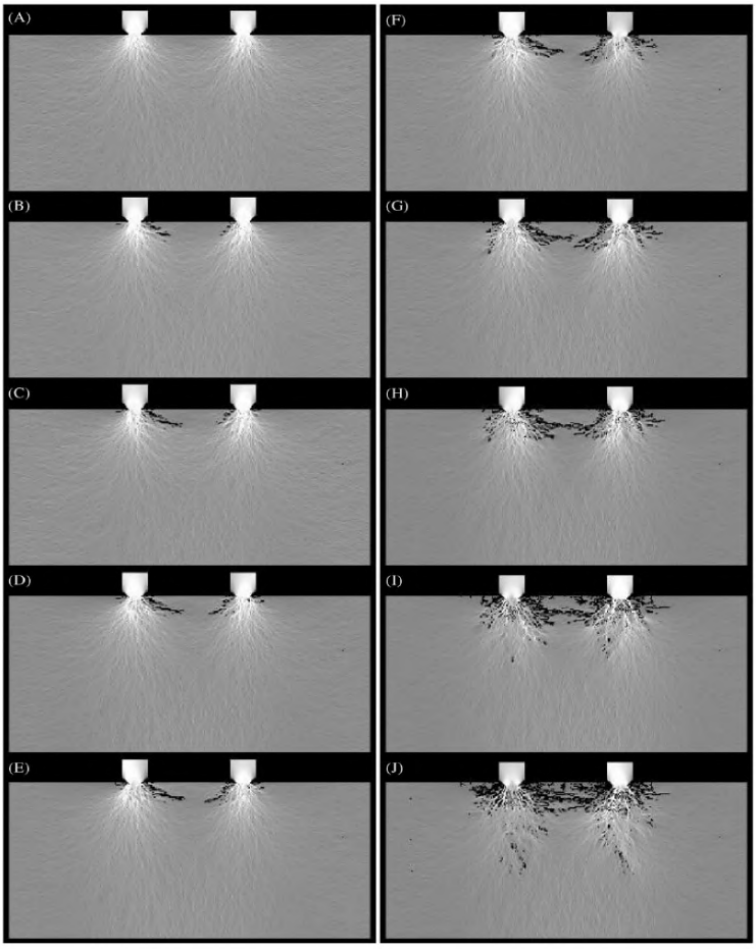

Figure 1.24: Simulated result for rock fragmentation process induced by double indenters [33].

At the first stage of loading, the respective stress fields induced by the double indenters are equal to those induced by the single indenter. The rocks immediately under the indenters are highly stressed. The stresses decrease rapidly with increasing distance from the loading points. However, with increasing loading displacement, the interference of the two stress fields induced by the two indenters are more and more obvious in the rock between the two indenters (see Fig. 1.24A). Cone cracks are initiated first around the two corners of both indenters (see Fig. 1.24B). Before the formation of the crushed zone, the cone cracks bifurcate and propagate approximately parallel to the free surface expected to form side cracks (see Fig. 1.24C). Because of the heterogeneity, the crack systems under the two indenters are not completely identical. However, similarities exist between the two crack systems. As the loading displacement increases, the crushed zones gradually come into being immediately under the indenter, and the side cracks are driven by tensile stresses associated with the expansions of the crushed zone (see Figs. 1.24D-E). With the loading displacement increasing, more and more side cracks are initiated from the two crushed zones (see Fig. 1.24F).

With a continuous loading displacement, the side cracks propagate stably forward and the subsurface cracks are richly developed under the indenters. Because of the heterogeneity, the side cracks propagate in a curvilinear path. The interactions between the side cracks are more and more obvious as the tips of the side cracks become closer and closer (see Fig. 1.24G). With the increasing loading displacement, the side cracks coalesce in a complicated manner and the rock between the two indenters is chipped (see Fig. 1.24H). The chipped rock has a complicated geometrical shape. As the loading displacement increases, the crack systems are well developed under the two indenters (see Fig. 1.24I). More cracks are initiated from the crushed zone. Some of them propagate to form side cracks and some of them dip into the rock forming subsurface cracks. At the same time, some discrete cracks are initiated under the crushed zones to form radial and median cracks. With increasing loading displacement, more and more side cracks interact and coalesce. Therefore, after the major chips, some small chips occur (see Fig. 1.24J).

When studying the effect of two indenters, the separation between the center lines of adjacent indenters is very important in the design and operation of systems to be used in rock drilling, because of the interaction between adjacent side splays of chipping grooves, [11, 33]. Figure 1.25 shows the simulated results for rock fragmentation induced by double indenters with different line spacing.

When the line spacing is small, the crack systems induced by the double indenters will behave in a manner similar to those caused by a single indenter (see Fig. 1.25B). As the line spacing increases, the indenters will act independently in the zones adjacent to the indenters and interact with each other in the zone between

the indenters (see Fig. 1.25A). With the appropriate line spacing, the interaction between the two indenters will have its full effect. At that time, the side cracks caused by the two indenters will interact and coalesce, giving a possible combined crack at great depth to form large rock chips, controlling the direction of subsurface cracks and consuming a minimum total specific energy.

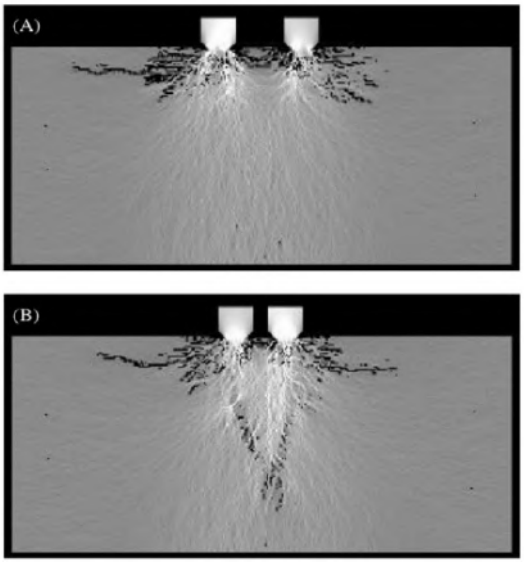

Figure 1.25: Rock fragmentation induced by double indenters with different line spacing [33].

In the design of drilling systems, the appropriate line spacing should be chosen to give the optimum performance in the practical operation of drilling machines [11].

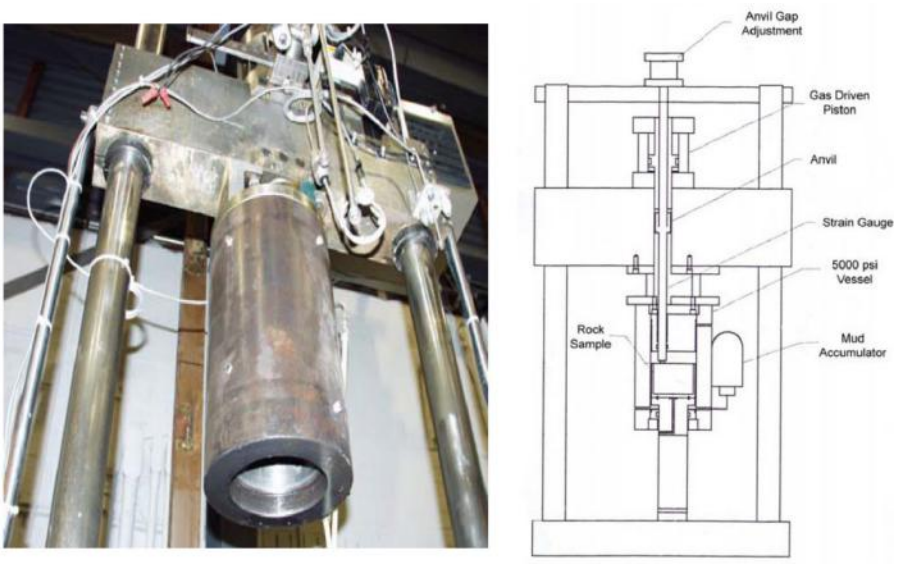

Figure 1.26: Photo and schematics of the Terratek single cutter impact test, adapted from [34].

The phenomenon of cutter-rock interaction in an impact scenario is regarded

as an intricate subject due to the high degree of complexity involved in the understanding of rock breakage mechanism and cuttings removal under the dynamic loading conditions of hammer drilling. Thus, there are limitation in the availability of experimental data of a single cutter impact testing. In that sense, GREEN *et al.* [34] explored extensive single indentation tests, which were performed at atmosphere and confined conditions, using three different rock formations, see Fig. 1.26. The results include cutter force-displacement and crater volumes for impact and quasi-static conditions.

GREEN *et al.* [34] emphasized that one important factor to consider in a hammer drilling analysis, or, in fact, in any impact testing analysis, is the energy transfer across any change in mechanical impedance. For instance, an induced change in geometry (deformation) or an induced change in materials (composite materials) affects the mechanical impedance. It is worth mentioning that the mechanical impedance, which is sometimes called acoustic impedance, is determined by the materials wave velocity, density and impact parts geometry.

The results presented by GREEN *et al.* [34] exhibited a correlation between the strain rate and the rock formation, as represented in Fig. 1.27. For calibration purposes, a T6 aluminum alloy was tested in static, rapid loading, and impact modes. The aluminum is not strain rate sensitive at room temperature and hence the static, rapid, and impact force-displacement curves should all coincide. The same methodology was applied to Carthage marble, which shows a comparison of static loading (time to peak load of about 600 seconds), rapid loadings (time to peak load of about 1.5 milliseconds), and impact loading (time to peak loading of about 150 microseconds). The rapid loading shows a slightly higher force for a given displacement, while the impact loadings exhibits the highest force for a given displacement - based on estimated strain rate sensitivity.

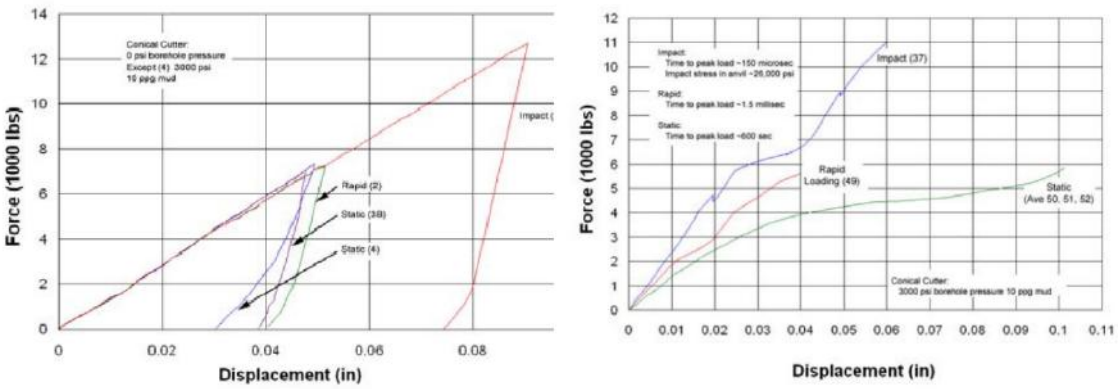

Figure 1.27: Strain rate independency of Aluminum (left) and strain rate dependency of Carthage marble (right), adapted from [34].

Varying the impact stress, i.e. varying the impact velocity of the gas driven piston

on the anvil shoulder, changes the stress magnitude of the stress wave traveling down the anvil. Thus, variation could raise or reduce the cutter force, hence increasing or decreasing the rock indentation. From the multiple indentation static tests under different rocks, see Fig. 1.28, the results reveal that the force-displacement correlation, in an initial stage, increases with an approximately constant slope, followed by a pronounced decrease in slope. The explanation for this reduction in the force-displacement slope, as explored by GREEN *et al.* [34], is probably related to the rock failure underneath the indenter. However, such statement is not clear for the Crab Orchard sandstone, since this sandstone has the highest UCS of the three tested lithologies (Crab Orchard sandstone: 25 kpsi UCS; Carthage marble: 16 kpsi UCS; Mancos shale: 6.3-9.8 kpsi UCS). Thus, the maximum indentation force could be below the required stress threshold to produce rock failure.

GREEN *et al.* [34] refer to this cutter force as the "chip formation force" and for the impact loadings, the "dynamic chip formation force" (DCF force). Further indentation leads to rapid force increase, followed by, in some cases, a second chip formation load point, and so forth. It appears that for stresses below the DCF force, the crater formed is small and considerable work is required to produce a small amount of rock destruction. And, above the DCF force, the load to produce additional indentation becomes considerably large, i.e. much work is required to produce additional rock destruction. Therefore, one could conclude that the optimum impact force should be designed to induce a stress just above the DCF force.

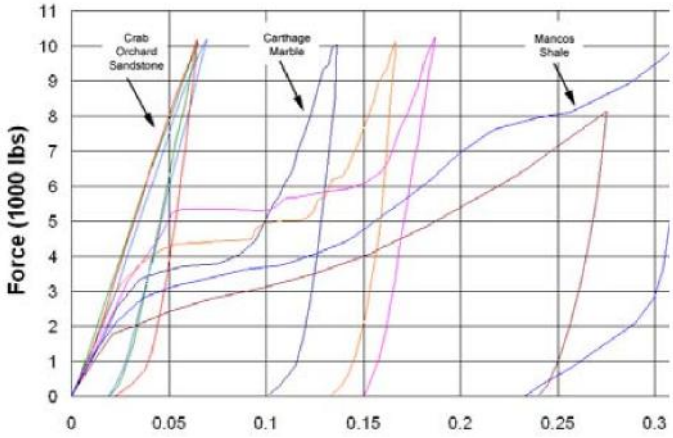

Figure 1.28: Repeated static loadings on rocks tested [34].

As conclusion, GREEN *et al.* [34] stated that the first stress wave cycle contributes most of the rock breakage for the evaluated design test. This analysis is likely to have an influence in real mud hammer designs. Additionally, the selection of impact forces that just exceed the cutter DCF force are critical, however any further increase in impacts forces seem to be less effective, since much less rock

breakage occurs for greatly increasing loads. It is expected that once the DCF force is reached, better use of energy can be made by increasing the blows per minute [11].

1.4 Summary

This literature review has shown that, in machining/drilling performance, there are advantages when superimposing a cutting mechanism with percussive movement. Such benefits may include faster penetration rates, reduction of tool wear, improvements in the surface finish and, in ductile materials, the reduction of burrs.

For percussion drilling, the optimum way to drill hard rocks would be to have high-energy loads per cutter and a rotary action that would move the cutters to "new" unfractured formation between each successive load [1]. In this literature review, no study was found regarding the optimum way of applying the impacts and its relation with the bit RPM.

In the oil industry, several vibration-assisted drilling tool prototypes were developed to be used in field applications. Although these various tools have been successfully tested in field applications, the level of understanding of the physics of vibration-assisted drilling tools is limited.

From a modeling perspective, regarding established contact force models, although the spring-dashpot model is not physically consistent, its simplicity has made it a popular choice for modeling the impact interaction in various vibro-impact models [25–29]. Thus, the spring-dashpot model seems to be an acceptable candidate for a first approach to model the impact interaction.

The numerical and experimental results of several vibro-impact models revealed that the best operating condition, or the maximum progression, coincided with the region that exhibits periodic behavior, [25–29].

A nonlinear tool was introduced to map regions of stable impact behavior in a 2D map [27]. This technique can be adapted to provide information about how certain design parameters affect the dynamic behavior of the model.

The main contributions of this thesis are:

- The development of a vibro-impact model that represents the axial dynamics of a vibration-assisted drilling prototype and the validation of this model using high-frequency field data.

- The proposed labeling process that managed to relate the impact pattern of each impact force with specific dynamic behaviors of the mathematical model. The relation between the average impacts per cycle (Z^*) for each

impact surface is used to index and map the dynamic behavior observed in the simulation results.

- The main results obtained from the parametric analysis were translated into design recommendation for the vibration-assisted drilling prototype. This information can later be used by product engineers to reevaluate the tool's design to improve the tool's performance.

This work contains a detailed description of the mathematical model and its application in chapter 2. A brief explanation of the available field data and the validation process of the proposed model is described in chapter 3. An investigation of the impact forces and its effects on the dynamic behavior of the system in done in chapter 4. The parametric analysis and the design recommendations, are described and analyzed in chapter 5. Finally, the concluding remarks are presented in chapter 6.

Chapter 2

Tool Description and Mathematical Modeling

In this chapter, a brief description of the vibration-assisted tool prototype is presented in section 2.1. Next, a detailed description of the proposed vibro-impact model is given in section 2.2.

2.1 Description of the vibration-assisted drilling tool

The vibration-assisted drilling tool analyzed in this work is based on the hammering apparatus shown in Fig. 2.1. This prototype is designed to be placed at the lower end of the drill string as a part of the bottom hole assembly (BHA) (see Fig. 2.2). The main function of this vibration apparatus is transform rotation motion of its main driving shaft into rectilinear movement [35]. This rectilinear motion is responsible for driving an impacting anvil that generates the high-energy low-frequency impacts. More information regarding this hammering apparatus can be found at POWELL *et al.* [35].

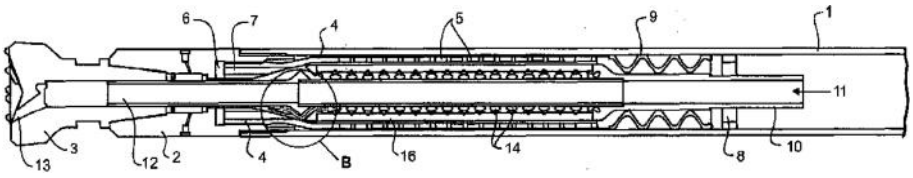

Figure 2.1: Conceptual sketch of the hammering apparatus [35].

The axial dynamics of the components inside the vibration-assisted drilling tool can be simplified into the impact interaction among four main components: the tool housing, anvil, recoil spring and bit assembly, as indicated in Fig. 2.2. The tool housing is responsible for transmitting the loads from the surface to the bit, as well

as to isolate the internal components from the drilling mud. The main purpose of the anvil, as the name suggests, is to work as an impacting mass. The recoil spring functions as an energy storage mechanism. Finally, the bit assembly is responsible for transmitting the impact loads to the rock formation, as the drill bit is a sub-component of this assembly. Additionally, the bit assembly contains a measurement sub that is responsible to record field data close to the drill bit.

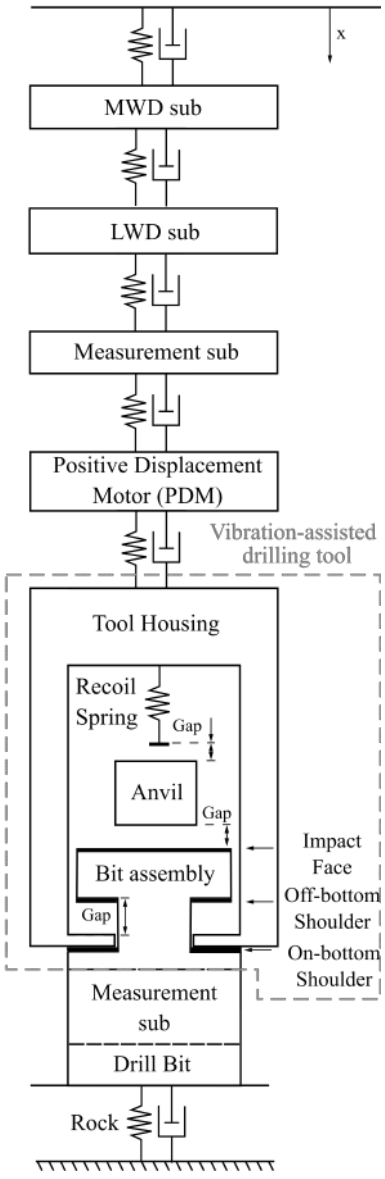

Figure 2.2: Sketch of the vibration-assisted drilling tool.

Besides these four components, other tools must be considered in the axial dynamics. These tools are: the positive displacement motor (PDM), another measurement sub, the Measurement While Drilling Tool (MWD) and the Logging While Drilling Tool (LWD). The PDM works as an inverted positive displacement pump, converting the hydraulic power of the mud fluid into mechanical power. The measurement sub is responsible for recording field data above the tool to evaluate

the axial vibration propagation through the drill string. The MWD is a responsible for the evaluation of the well path, and transmitting this information in real time by means of a pressure wave (mud pulsing). The LWD measures geological parameters, such as resistivity and porosity, and stores this downhole data to be evaluated after the tool is retrieved.

The working principle of this tool can be reduced into five steps. First, an excitation force drives the anvil towards the bit assembly. Next, the anvil makes contact with the bit assembly (impact face), which results in an impact force, transmitted to the rock by the bit assembly. In the sequence, the excitation force pushes the anvil towards the recoil spring. In the fourth step, the anvil impacts the recoil spring, which results in elastic deformation of the spring, converting the kinetic energy of the anvil into elastic potential energy for the next cycle movement. Finally, the spring and the excitation force drives the anvil in the direction of the bit assembly, restarting the cycle.

In this work, there are two sets of tools that are considered in this modeling: a 7in and a 9.5in diameter tools. Although these tools have the same working principle, they differ slightly in their application in the oilfield industry. The 7in vibration-assisted tool is designed to be used with 8.5in drill bits, while the 9.5in prototype is designed to be coupled with 12.25in drill bits. As a result, even though a single mathematical model is proposed for both tools, a unique sets of input parameters is obtained for each vibration-assisted tool.

The next step is to present a detailed description of the mathematical model that aims at representing the axial vibrations of this prototype.

2.2 Mathematical Modeling

The system analyzed in this work is sketched in Fig. 2.3. A seven degrees-of-freedom lumped parameter vibro-impact system is proposed to model the vibration-assisted drilling tool. Each component described in the sketch of the vibration-assisted drilling tool prototype (see Fig. 2.2) is represented in the sketch of the lumped parameter model (see Fig. 2.3). The MWD sub is represented by the seventh degree-of-freedom, the LWD sub is represented by the sixth degree-of-freedom, the measurement sub is represented by the fifth degree-of-freedom, the PDM is represented by the fourth degree-of-freedom, the tool housing is represented by the third degree-of-freedom, the anvil is represented by the second degree-of-freedom, and the bit assembly is represented by the first degree-of-freedom.

The system is fixed at the top, above the seventh degree-of-freedom (MWD sub), and, at the bottom, two configurations are considered: on-bottom and off-bottom. In the on-bottom configuration, shown in Fig. 2.4a, the system tool is in contact

with the rock formation at the bottom of the well (impact surface #4), where the stiffness k_R and the damping coefficient c_R emulate the rock formation. In the off-bottom configuration, shown in Fig. 2.4b, m_1 is not in contact with the rock formation, and, therefore, the rock formation is disconnected from the rest of the system.

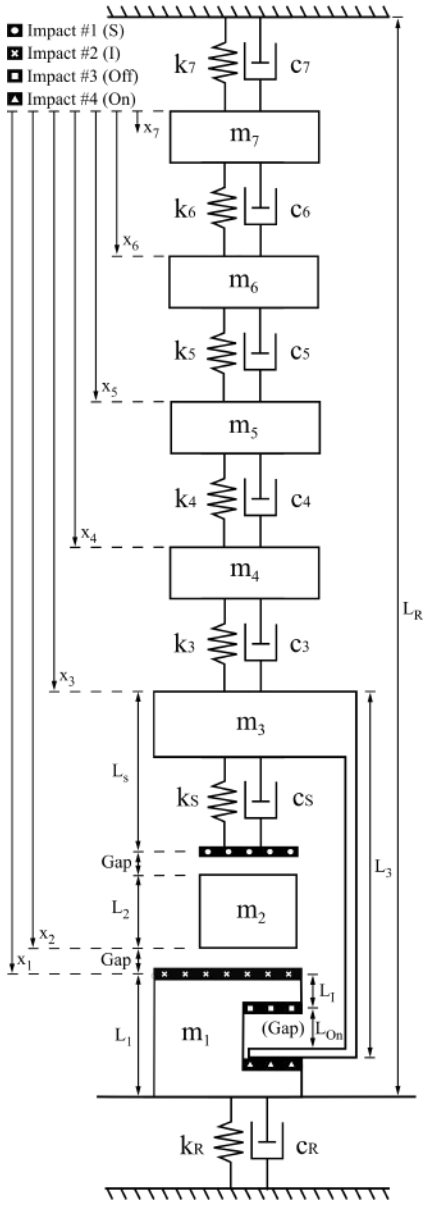

Figure 2.3: Sketch of the lumped parameter model.

Since this modeling effort focus on the description of the axial dynamics of a vibration assisted drilling tool, there are some limitations associated with the proposed model. In summary, this modeling effort will not capture rotary motion of the drill string, lateral or torsional vibration, effect of the system hydraulics, and effect of lithology on ROP.

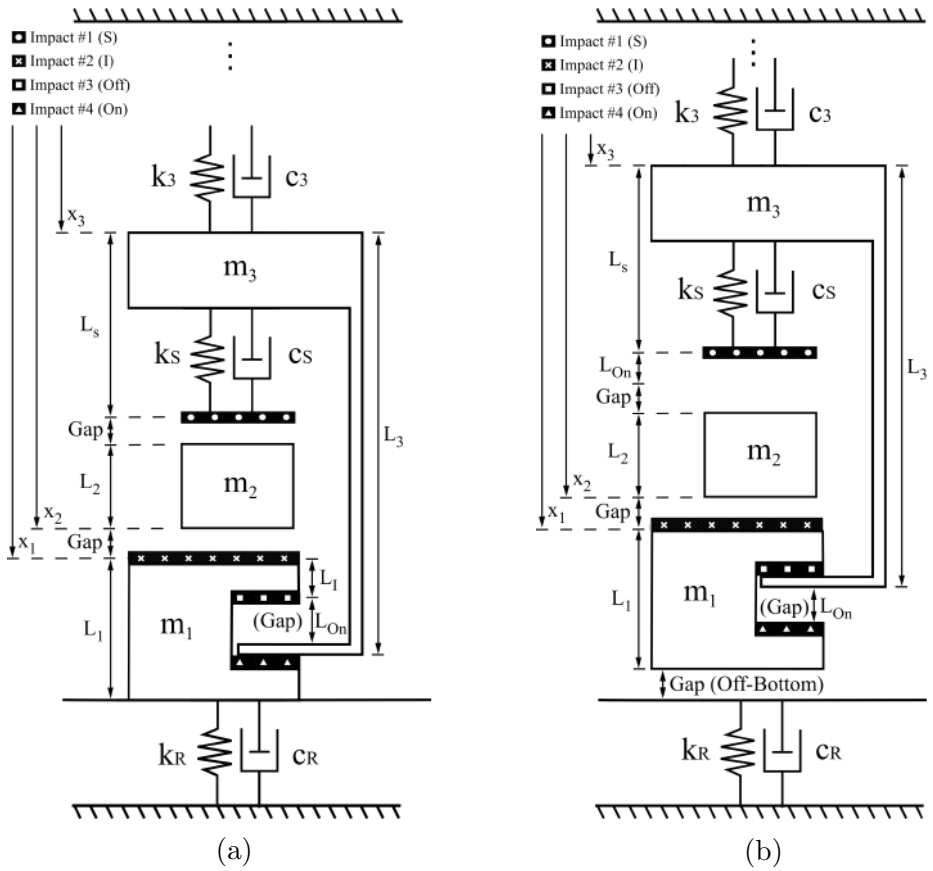

Figure 2.4: Representations of both (a) the on-bottom and (b) the off-bottom configurations for the mathematical model.

A detailed description of the axial dynamics of each degree of freedom is provided in the next section. It should be noted that the available field data, used in the validation process, contains responses for the on-bottom configuration.

2.2.1 Equations of motion

A linear modeling is pursued for the structural components, where masses (inertia), springs (stiffness), and dashpots (dissipation mechanism) are considered. The seventh degree-of-freedom (MWD sub) is connected to the rigid support by a spring-damper element, and it is coupled with the sixth degree-of-freedom (LWD sub). Therefore, the equation of motion for the seventh degree-of-freedom (MWD sub) is given in Eq. (2.1).

$$m_7\ddot{x}_7 = -k_7x_7 + k_6(x_6 - x_7) - c_7\dot{x}_7 + c_6(\dot{x}_6 - \dot{x}_7)\,, \tag{2.1}$$

where x_7, m_7, k_7 and c_7 are, respectively, the displacement, mass, stiffness and viscous damping coefficient of the seventh degree-of-freedom (MWD sub), x_6, k_6 and c_6 are, respectively, the displacement, stiffness and viscous damping coefficient of the sixth degree-of-freedom (LWD sub).

In regards to the sixth degree-of-freedom (LWD sub), this component is coupled to both the seventh (MWD sub) and the fifth degrees-of-freedom (measurement sub) by spring-damper elements. As a result, its equation of motion is given by Eq. (2.2).

$$m_6\ddot{x}_6 = -k_6(x_6 - x_7) + k_5(x_5 - x_6) - c_6(\dot{x}_6 - \dot{x}_7) + c_5(\dot{x}_5 - \dot{x}_6)\,, \tag{2.2}$$

where m_6 is the mass of the sixth degree-of-freedom (LWD sub), x_5, k_5 and c_5 are, respectively, the displacement, stiffness and viscous damping coefficient of the fifth degree-of-freedom (measurement sub).

Using the same reasoning, the equation of motion for the fifth and fourth bodies, which represent the measurement sub and the PDM, respectively, are given by Eqs. (2.3) and (2.4).

$$m_5\ddot{x}_5 = -k_5(x_5 - x_6) + k_4(x_4 - x_5) - c_5(\dot{x}_5 - \dot{x}_6) + c_4(\dot{x}_4 - \dot{x}_5)\,, \tag{2.3}$$

where m_5 is the mass of the fifth degree-of-freedom (measurement sub), x_4, k_4 and c_4 are, respectively, the displacement, stiffness and viscous damping coefficient of the fourth degree-of-freedom (PDM).

$$m_4\ddot{x}_4 = -k_4(x_4 - x_5) + k_3(x_3 - x_4) - c_4(\dot{x}_4 - \dot{x}_5) + c_3(\dot{x}_3 - \dot{x}_4)\,, \tag{2.4}$$

where m_4 is the mass of the fourth degree-of-freedom (PDM), x_3, k_3 and c_3 are, respectively, the displacement, stiffness and viscous damping coefficient of the third degree-of-freedom (tool housing).

The motion of the third degree-of-freedom (tool housing) is coupled with the fourth degree-of-freedom (PDM), and submitted to three additional forces (see detail in Fig. 2.3): the force from the recoil spring (if m_2 touches the impact surface #1), the impact force from surface #3, and the impact force from surface #4.

The maximum axial displacement of the third degree-of-freedom (tool housing) is restricted on both sides (lower and upper). Therefore, the equation of motion that describes the dynamics of the third degree-of-freedom is given in Eq. (2.5).

$$\begin{aligned} m_3\ddot{x}_3 = & -k_3(x_3 - x_4) - c_3(\dot{x}_3 - \dot{x}_4) - F_S(x_2, \dot{x}_2, x_3, \dot{x}_3) - F_{On}(x_1, \dot{x}_1, x_3, \dot{x}_3) \\ & + F_{Off}(x_1, \dot{x}_1, x_3, \dot{x}_3)\,, \end{aligned} \tag{2.5}$$

where m_3 is the mass of the third degree-of-freedom (tool housing), x_2 is the displacement of the second degree-of-freedom (anvil), x_1 is the displacement of the first degree-of-freedom (bit assembly), $F_{On}(x_1, \dot{x}_1, x_3, \dot{x}_3)$ is the impact force for the on-bottom shoulder, $F_{Off}(x_1, \dot{x}_1, x_3, \dot{x}_3)$ is the impact force from the off-bottom shoulder, and $F_S(x_2, \dot{x}_2, x_3, \dot{x}_3)$ is the force from the recoil spring. These forces are

depicted in the next section.

The axial displacement the second degree-of-freedom (anvil) is restricted by the recoil spring (impact surface #1) and the first degree-of-freedom (impact surface #2). Additionally, this component is also submitted to two additional forces: a drag force and an excitation force. The second degree-of-freedom (anvil) is inside a chamber that is filled with a low viscosity fluid to reduce the friction among components. This fluid-structure interaction force is approximated by a drag force. This force and the excitation force are depicted in the next section. The equation of motion of the second degree-of-freedom is given by Eq. (2.6).

$$m_2\ddot{x_2} = -F_I(x_1, \dot{x_1}, x_2, \dot{x_2}) + F_S(x_2, \dot{x_2}, x_3, \dot{x_3}) + F_H(x_2, x_3, t) - F_D(\dot{x_2})\,, \qquad (2.6)$$

where m_2 is the mass of the second degree-of-freedom (anvil), $F_I(x_1, \dot{x_1}, x_2, \dot{x_2})$ is the impact force from the impact face, $F_H(x_2, x_3, t)$ is the excitation force, $F_D(\dot{x_2})$ is the fluid-structure interaction force.

In regards to the axial displacement of the first degree-of-freedom (bit assembly), this component is submitted to four external forces: the force from the interaction with the flexible support (rock formation), the impact force from the on-bottom shoulder (impact surface #4), the impact force from the off-bottom shoulder (impact surface #3), and the impact force from the impact surface #2. The impact forces from the on-bottom and off-bottom shoulder are related to the interaction between the first and the third degrees-of-freedom, while the impact force from the impact surface arises from the collision between the first and second degrees-of-freedom. Thus, the equation of motion that describes the dynamics of the first degree-of-freedom is given by Eq. (2.7).

$$\begin{aligned} m_1\ddot{x_1} = & -F_R(x_1, \dot{x_1}) + F_{On}(x_1, \dot{x_1}, x_3, \dot{x_3}) - F_{Off}(x_1, \dot{x_1}, x_3, \dot{x_3}) \\ & + F_I(x_1, \dot{x_1}, x_2, \dot{x_2})\,, \end{aligned} \qquad (2.7)$$

where $F_R(x_1, \dot{x_1})$ is the bit-rock interaction force and m_1 is the mass of the first degree-of-freedom.

With the description of the axial displacement of each degree of freedom, a detailed description of the modeling of the impact forces and external forces is provided in the next section.

2.2.2 Impact Forces and External Forces

As stated by Riley and Sturges [16], impact can be defined as a complex physical interaction between two or more bodies that undergo one or more collisions among

themselves. The main properties of the impact phenomenon can be simplified into four characteristics: quasi-instantaneous interaction, high forces, rapid energy dissipation and considerable acceleration variation [17]. These characteristics vary according to the material properties of each body that undergoes an impact, as well as geometrical properties. Different models for the impact force have been developed along the history [17, 21–23, 30]. As a first approach, the spring-dashpot model is employed to describe the impact forces of the system.

In the current model, as seen in Fig. 2.3, there are four impact surfaces. The impact induces discontinuities, since the impact forces are present only if two bodies are in contact, which is introduced in the mathematical model through the Heaviside function H. The displacement of the bodies are tracked, and a variable named indentation (δ) is computed at each instant. If this variable is positive, the bodies are colliding and there is an impact force. However, a negative indentation value means that there is a gap between the bodies, hence no contact between them. The impact forces listed in Eq. (2.5), (2.6) and (2.7) are described in Eq. (2.8) to (2.15).

$$F_{On}(x_1, \dot{x_1}, x_3, \dot{x_3}) = H(\delta_{On})(k_{On}\delta_{On} + c_{On}\dot{\delta}_{On}) \,, \tag{2.8}$$

$$\delta_{On} = (x_3 + L_3) - (x_1 + L_I - L_{On}) \,, \tag{2.9}$$

where $H(\delta)$ is the Heaviside function, k_{On}, c_{On} and δ_{On} are, respectively, the stiffness, viscous damping coefficient and the indentation related to impact #4. L_3 is the length from the top to the third degree-of-freedom, L_I is the distance between impact surfaces #2 and #3, and L_{On} is the gap between the on-bottom and the off-bottom shoulders.

$$F_{Off}(x_1, \dot{x_1}, x_3, \dot{x_3}) = H(\delta_{Off})(k_{Off}\delta_{Off} + c_{Off}\dot{\delta}_{Off}) \,, \tag{2.10}$$

$$\delta_{Off} = (x_1 + L_3) - (x_3 - L_I) \,, \tag{2.11}$$

where k_{Off}, c_{Off} and δ_{Off} are, respectively, the stiffness, viscous damping coefficient and the indentation related to impact #3.

$$F_I(x_1, \dot{x_1}, x_2, \dot{x_2}) = H(\delta_I)(k_I\delta_I + c_I\dot{\delta}_I) \,, \tag{2.12}$$

$$\delta_I = (x_2 - x_1) \,, \tag{2.13}$$

where k_I, c_I and δ_I are, respectively, the stiffness, viscous damping coefficient and the indentation derived from the impact model applied to the impact face surface.

In regards to the recoil spring, this component is approximated as a spring-dashpot model, which considers a linear spring with a viscous damping component. However, due to the discontinuous interaction with the anvil, the recoil spring force is given by Eq. (2.14) and (2.15).

$$F_S(x_2, \dot{x_2}, x_3, \dot{x_3}) = H(\delta_S)(k_S\delta_S + c_S\dot{\delta}_S)\,, \tag{2.14}$$

$$\delta_S = (x_3 + L_S) - (x_2 - L_2)\,, \tag{2.15}$$

where k_S, c_S, δ_S and L_S are, respectively, the stiffness, the viscous damping coefficient, the indentation and the length of the recoil spring, and L_2 is the distance from the topt o the second degree-of-freedom.

The excitation force that drives the the second degree-of-freedom is a periodic force that considers two major parameters: the mud flow rate and the relative displacement between the second and third degrees-of-freedom. This excitation force is modeled as a combination of two harmonic functions, given by

$$F_H(x_2, x_3, t) = F_o \cos(\alpha Q t + \phi) \sin(\beta(x_2 - x_3) + \psi)\,, \tag{2.16}$$

where the first harmonic term, $\cos(\alpha Q t + \phi)$, captures the influence of the mud flow rate, and the second periodic expression, $\sin(\beta(x_2 - x_3) + \psi)$, introduces the dependency on the relative displacement between the second and third degrees-of-freedom. F_o is the maximum magnitude of the excitation force, Q is the mud flow rate in gallons per minute, α, β, ϕ and ψ are constants.

Additionally, the third degree-of-freedom (tool housing) is filled with a low viscosity fluid to reduce the friction between components. The fluid-structure interaction is simplified as an uniaxial displacement of the second body inside the fluid chamber resulting in a drag force [36], given by

$$F_D(\dot{x_2}) = c_D(\dot{x}_2)^2\,, \tag{2.17}$$

where c_D is the drag coefficient of the low viscosity fluid.

The effect of the lithology on the rate of penetration (ROP) is not considered in this model. Hence, the rock formation is modeled only as a flexible support to the entire drill string, not capturing any effect of ROP. To represent both the off-bottom and on-bottom configurations, as well as to account for possible discontinuous behavior (bit-bounce), the equation of the reaction force from the rock follows the same structure applied to the impact models' equations, as described by Eqs. (2.18) and (2.19).

$$F_R(x_1, \dot{x_1}) = H(\delta_R)(k_R\delta_R + c_R\dot{\delta}_R)\,, \tag{2.18}$$

$$\delta_R = (x_1 + L_1) - L_R\,, \tag{2.19}$$

where k_R, c_R and δ_R are, respectively, the stiffness, viscous damping coefficient and the indentation related to the displacement of m_1. L_1 is the distance from the top to the first degree-of-freedom, and L_R is the distance between the rigid support (upper boundary) and the flexible support that represents the rock formation (lower boundary).

2.2.3 Input Parameters

With the detailed description of the axial dynamics of the mathematical model, the set of input parameters obtained from the validation process is given in Tab. 2.1.

Var.	7in	9.5in	Units	Var.	7in	9.5in	Units	Var.	7in	9.5in	Units
$m^*_{1(PDC)}$	1.44	3.01	-	k^*_R	7.87E+04	1.97E+04	$Nm^{-1}kg^{-1}$	L^o_1	1.24	1.54	-
$m^*_{1(RC)}$	1.29	-	-	c^*_3	7.87E+02	2.36E+03	$N.s\,m^{-1}kg^{-1}$	L^o_2	2.16	2.18	-
m^*_2	1.00	1.63	-	c^*_4	8.66E+02	1.57E+03	$N.s\,m^{-1}kg^{-1}$	L^o_3	4.06	4.7	-
m^*_3	3.78	8.06	-	c^*_5	9.45E+02	1.24E+03	$N.s\,m^{-1}kg^{-1}$	L^o_S	1.80	2.41	-
m^*_4	7.24	17.80	-	c^*_6	7.56E+02	9.92E+02	$N.s\,m^{-1}kg^{-1}$	L^o_I	0.07	0.08	-
m^*_5	1.17	1.43	-	c^*_7	7.87E+03	1.03E+04	$N.s\,m^{-1}kg^{-1}$	L^o_{On}	0.01	0.01	-
m^*_6	4.70	5.75	-	c^*_S	16.54	58.27	$N.s\,m^{-1}kg^{-1}$	L^o_R	5.21	6.12	-
m^*_7	9.18	11.23	-	c^*_I	4.69E+02	2.12E+02	$N.s\,m^{-1}kg^{-1}$	ω_3	120.84	89.32	Hz
k^*_3	2.18E+06	2.54E+06	$Nm^{-1}kg^{-1}$	c^*_{On}	1.28E+03	3.82E+02	$N.s\,m^{-1}kg^{-1}$	ω_4	132.74	100.21	Hz
k^*_4	5.04E+06	7.06E+06	$Nm^{-1}kg^{-1}$	c^*_{Off}	1.28E+03	3.82E+02	$N.s\,m^{-1}kg^{-1}$	ω_5	887.30	949.34	Hz
k^*_5	3.62E+07	5.07E+07	$Nm^{-1}kg^{-1}$	c^*_R	3.94E+02	7.87E+01	$N.s\,m^{-1}kg^{-1}$	ω_6	181.92	194.48	Hz
k^*_6	6.14E+06	8.58E+06	$Nm^{-1}kg^{-1}$	c^*_D	2.52	2.93	$N.s^2m^{-2}kg^{-1}$	ω_7	87.20	93.30	Hz
k^*_7	2.76E+06	3.86E+06	$Nm^{-1}kg^{-1}$	$F_o{}^*$	300.47	455.12	Nkg^{-1}	ζ_3	0.14	0.26	-
k^*_S	2.50E+05	4.33E+05	$Nm^{-1}kg^{-1}$	α	0.67	0.10	rev/gallon	ζ_4	0.07	0.07	-
k^*_I	1.20E+05	4.82E+04	$Nm^{-1}kg^{-1}$	β	95.20	104.72	m^{-1}	ζ_5	0.07	0.07	-
k^*_{On}	1.34E+06	3.69E+04	$Nm^{-1}kg^{-1}$	φ	0.98	0.65	-	ζ_6	0.07	0.07	-
k^*_{Off}	1.34E+06	3.69E+04	$Nm^{-1}kg^{-1}$	ψ	-2.14	-5.86	-	ζ_7	0.78	0.78	-

Table 2.1: Input parameters for the vibration-assisted drilling tool mathematical model, where ω is the natural frequency and ζ is the damping ratio.

**Due to confidentiality agreements, the input parameters that are marked with the asterisk symbol (*) are standardized by a reference mass (m^*), while the variables marked with the degree symbol (^{o}) are normalized by a standard length (l^o).*

The mathematical model proposed describes the axial dynamics of a small section of the entire drill string, as the drill pipes are not considered in this model. In the real system, the shock waves generated by the impact interactions would be transmitted up the drill string going through the drill pipes until reaching the surface. In this mathematical model, however, the shock waves are restricted to this small section of

the drill string. Thus, these shock waves are reflected back into the system instead of being dissipated upwards the drill string, introducing disturbances in the axial dynamics of the model. In order to minimize the effects of the reflected shock waves, the viscous damping coefficient of the seventh degree-of-freedom is adjusted to mitigate these axial vibration disturbances.

With the available set of ordinary differential equations (ODE) that represent the equations of motion of the vibro-impact system, the next step is to define the simulation workflow to evaluate the computation efficiency of different numerical methods available to solve these set of ODEs.

2.2.4 Model Implementation

The proposed model was implemented in MATLAB/ Simulink platform. MATLAB (matrix laboratory) is a well-known numerical computing environment, a proprietary programming language developed by MathWorks. Simulink, developed by MathWorks, is a graphical programming environment for modeling, simulating and analyzing multi domain dynamic systems.

The model implementation in Simulink focused in a modular approach, where each sub system was organized into modules (modeling blocks), as represented in Fig. 2.5. In the current version, there are four distinct modules (axial dynamics, driller, excitation force, and observer) and three predefined inputs (set point WOB, hole depth, and mud flow rate).

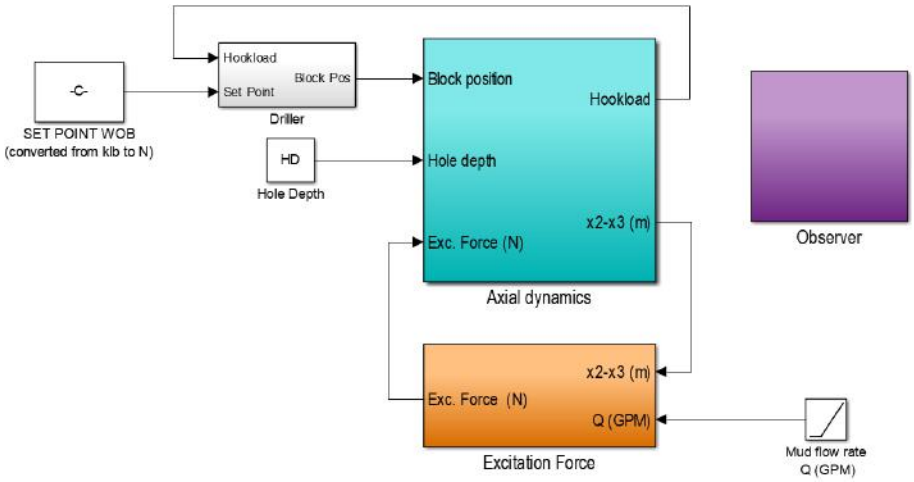

Figure 2.5: High level modeling of the mathematical model implemented on Simulink.

The axial dynamics module is responsible for solving the equations of motion. The driller modulus is responsible for applying the desired WOB. The excitation force module calculates the excitation force through the relative displacement between the anvil (x_2) and the tool housing (x_3), as well as the mud flow rate

(Q) (see Eq. (2.16)). The observer module is responsible for real-time display and exporting the simulation results.

Besides these four modules, there are three predefined inputs that are considered in the simulation. These inputs are: the set point WOB, the hole depth (HD), and the mud flow rate. The set point WOB corresponds to the desired WOB applied on the bit. The hole depth defines the initial gap between the drill bit and the rock formation, which enables the initial conditions of the simulation to start in a off-bottom configuration. The mud flow rate is used in the excitation force module to calculate the excitation force frequency.

The simulation workflow is described as follows:

1. The simulation starts with the tool in an off-bottom configuration at a predefined distance from the rock formation (see Fig. 2.4b). At this stage, the mud flow rate is zero and the vibration-assisted drilling tool is inactive.

2. Next, the simulation emulates the descent of drill string through the activation of the driller modulus. The driller modulus contains a proportional–integral–derivative controller (PID) that is responsible for controlling the relative position between the drill bit and the rock formation. As the driller module is activated, the drill string position is lowered until it bit makes contact with the rock formation.

3. After the drill bit makes contact with the rock formation, the tool changes into a on-bottom configuration (see Fig. 2.4a).

4. Further adjustment is made to the position of the drill string to ensure that the desired WOB is applied.

5. Next, as the desired WOB is achieved, PID controller inside the driller modulus is deactivated. This is ensured by fixing the relative position between the drill string and the rock formation.

6. After guaranteeing the driller modulus is inactive, the vibration-assisted drilling tool is activated by applying the desired mud flow rate.

7. After the tool is activated, the simulation runs for 400 cycles. One cycle is defined as the period of the excitation force. To ensure steady-state behavior, the simulation results are only evaluated after 200 cycles.

With the simulation workflow defined, an adequate ordinary differential equation (ODE) solver must be selected. From the available ordinary differential equations solvers in MATLAB, three ODE solvers were evaluated in relation to computational time, as shown in Tab. 2.2. This computational time is recorded by the Simulink

platform and it computes the time taken for the completion of the entire simulation workflow. For this analysis, the initial conditions of the simulations considered 4klbf of WOB and 200GPM of mud flow rate. The computation time of each ODE solver is compared with the best performing ODE solver to give a relative performance perspective. The ODE23t solver showed the best performance when compared to the fourth order ODE15s solver by a factor of 2.52. It is worth mentioning that the traditional 4^{th}-5^{th} order Runge-Kutta method implemented in ODE45 was discarded as due to computational inefficiency and convergence issues.

ODE solver	Computational time	Relative performance
ODE15s - 5^{th} order	126s	2.63
ODE15s - 4^{th} order	121s	2.52
ODE23t	48s	1.00
ODE45	—	—

Table 2.2: Performance comparison between three ordinary differential equation (ODE) solvers implemented to solve the current vibro-impact model. ODE23t shows the best performance.

Chapter 3

Field Data Analysis and Model Validation

The validation process of a mathematical model implies a detailed analysis and revision of a large amounts of experimental data. Furthermore, the entire process requires a rigorous and detailed approach to properly evaluate the simulation results. Thus, the entire procedure is reduced into separate sections to organize in a simple and efficient process. A brief explanation of the available field data is given in section 3.1, and the model calibration is done in section 3.2. The numerical results, and their comparison with field data, are analyzed in section 3.3.

3.1 Description of the Field Tests

The field tests were performed in two Schlumberger-owned and -operated drilling rigs at the Cameron Test and Training Facility (CTTF) and at the Genesis Test and Training Facility (GTTF), as shown in Fig. 3.1. The main objectives of these training facilities are to support new product development (NPD) and to perform segment system integration tests. All tests facilities are equipped with a drilling rig, as well as a flow control system that enables the driller to control the mud flow rate, the weight-on-bit and drill string rotation speed.

In total, there were three separate field tests: two tests were performed with the 7in tool at CTTF and one field test was performed with the 9.5in tool at GTTF. In these tests, the tools are submitted to drilling conditions that emulate an drilling operation, which include low WOB and constant mud flow rate for a sufficiently long time-frame to achieve steady-state behavior.

The main objective of these tests was to evaluated the dynamic response of both the 7in and 9.5in tools by varying the excitation frequency and by maintaining a constant WOB. Since the excitation frequency is related to the mud flow rate (see

Eq. 2.16), the excitation frequency range is dependent on the choice of the mud flow range that is selected for each the field test. This this choice takes into consideration the technical specifications of the PDM, which restricts the mud flow range based on power and performance curves.

The available data was recorded by measurement subs located at the bit assembly (x_1) and at the measurement sub above the PDM (x_5) . These devices are equipped with a 3-axis accelerometer, with maximum sensor range of 250g (2452 m/s^2) and measurement frequency of 1024Hz. No measurements were taken inside the vibration-assisted drilling tool because the conditions of a drilling operations do not allow further instrumentation inside the tool.

(a) (b)

Figure 3.1: (a) The Cameron Test and Training Facility (CTTF) and (b) the Genesis Test and Training Facility (GTTF) drilling rigs. Both facilities are located in Texas, USA.

A brief description of the test conditions is presented for each tool test. Furthermore, an overview of each field test is shown to identify key events that will be used in the validation process of the mathematical model.

3.1.1 Field tests at Cameron Test and Training Facility

The available data was obtained from two field tests performed with the 7in vibration-assisted tool at CTTF. One test used a 8.5in fixed cutter bit with conical diamond elements (CDE) cutters (see Fig. 3.2a), and the other used a 8.5in roller

cone bit (RC) (see Fig. 3.2b).

(a) (b)

Figure 3.2: (a) 8.5in fixed cutter bit with conical diamond elements (CDE) cutters and (b) 8.5in roller cone bit (RC) that were used in field tests performed with the 7in vibration-assisted tool at CTTF.

Field test with the 7in tool coupled with CDE drill bit

An overview of the axial vibration field data recorded during field test with the 7in tool coupled with CDE drill bit is presented in Fig. 3.3.

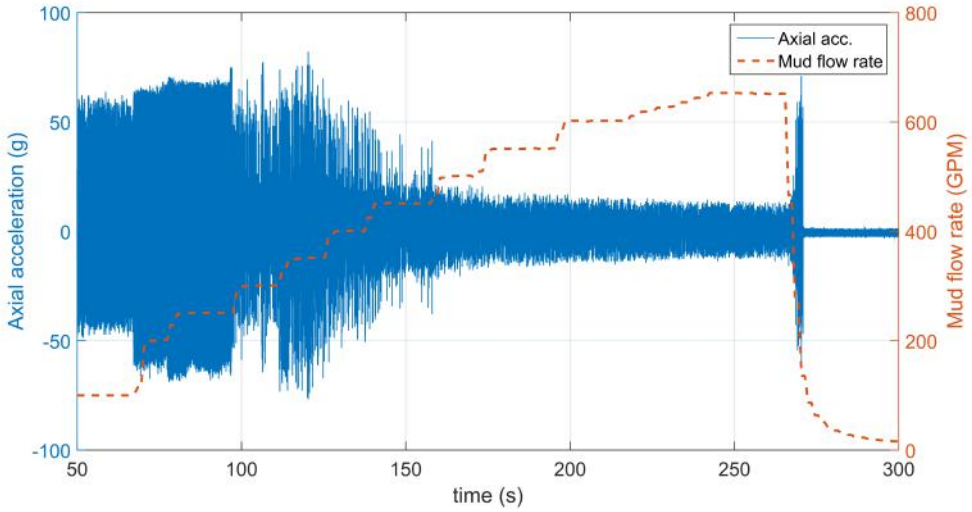

Figure 3.3: Overview of the axial vibration field data recorded by the measurement sub located at x_1 (bit assembly) during the 7in tool test (CDE bit). This test was performed with a constant weight-on-bit of 4klbf and with a varying mud flow rate from 200 to 650GPM.

The main objective of this test was to evaluated the dynamic response of the tool by varying the excitation frequency from 21.3 to 69.3Hz with a 5.3Hz increment and

by maintaining a constant weight-on-bit of 4klbf. This excitation frequency range is achieved through a mud flow sweep from 200 to 650GPM with a 50GPM increment, as the excitation frequency is related to mud flow rate (see Eq. 2.16). The axial vibration data recorded by the measurement sub located at the bit assembly (x_1) is presented in Fig. 3.3.

After analyzing the field data of 7in tool coupled with CDE drill bit (see Fig. 3.3), there were 10 events that were selected to be included in the validation process, as described in Table 3.1.

Run	Test - 7in Tool (CDE bit) @ CTTF	
Major Events	Time	Mud Flow Rate (Excitation Frequency)
1st	26/03/2015 3:03	200GPM (21.3Hz)
2nd	26/03/2015 3:03	250GPM (26.7Hz)
3rd	26/03/2015 3:04	300GPM (31.2Hz)
4th	26/03/2015 3:04	350GPM (37.3Hz)
5th	26/03/2015 3:05	400GPM (42.7Hz)
6th	26/03/2015 3:05	450GPM (48.0Hz)
7th	26/03/2015 3:06	500GPM (53.3Hz)
8th	26/03/2015 3:06	550GPM (58.6Hz)
9th	26/03/2015 3:07	600GPM (64.0Hz)
10th	26/03/2015 3:07	650GPM (69.3Hz)

Table 3.1: Major events selected from the 7in tool coupled with CDE drill bit at CTTF to be used in the validation process.

Field test with the 7in tool coupled with RC drill bit

With the experience gained from the previous test of 7in tool (see Fig. 3.3), some minor adjustments were made to the excitation frequency range applied in this test. The axial vibration data of the 7in tool with the CDE drill bit revealed that excitation frequencies above 53.3Hz (500 GPM) show similar dynamic behavior, as well as low axial acceleration peaks. Thus, the a decision was taken to reduce the excitation frequency range to cover the most relevant excitation frequency range, which translates into frequency range of 21.3Hz to 53.3Hz (200 to 500 GPM). The axial vibration data recorded by the measurement sub located at the bit assembly (x_1) is presented in Fig. 3.4.

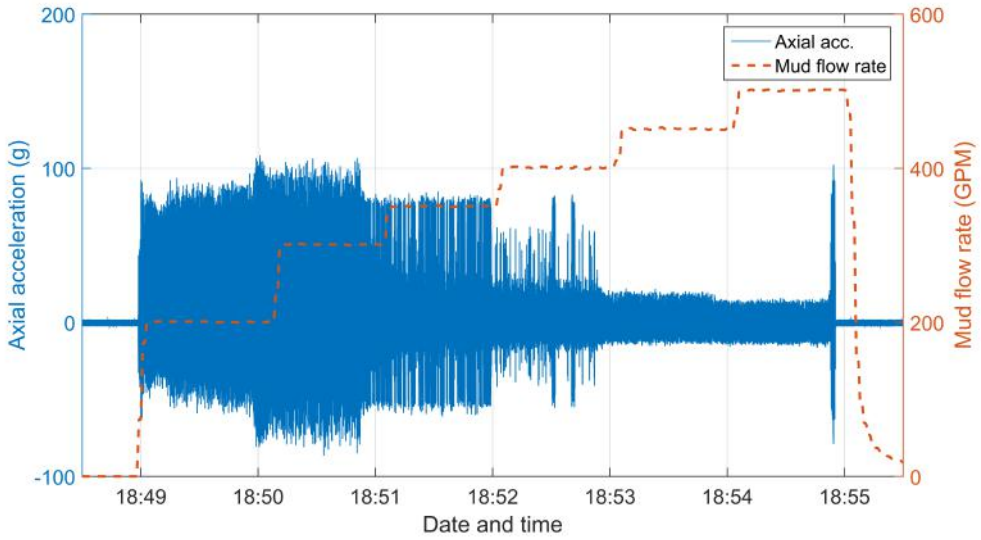

Figure 3.4: Overview of the axial vibration field data of the sensor data located at x_1 (bit assembly) during the 7in tool test (RC bit). This test was performed with a constant weight-on-bit of 4klbf and with a varying mud flow rate from 200 to 500GPM.

After analyzing the field data of 7in tool coupled with RC drill bit (see Fig. 3.4), there were 6 events that were selected to be included in the validation process, as described in Table 3.2.

Run	Test - 7in Tool (RC bit) @ CTTF	
Major Events	Time	Mud Flow Rate (Excitation Frequency)
11th	02/04/2015 18:49 - 18:50	200GPM (21.3Hz)
12th	02/04/2015 18:50 - 18:51	300GPM (31.2Hz)
13th	02/04/2015 18:51 - 18:52	350GPM (37.3Hz)
14th	02/04/2015 18:52 - 18:53	400GPM (42.7Hz)
15th	02/04/2015 18:53 - 18:54	450GPM (48.0Hz)
16th	02/04/2015 18:54 - 18:55	500GPM (53.3Hz)

Table 3.2: Major events selected from the 7in tool coupled with RC drill bit at CTTF to be used in the validation process.

3.1.2 Field tests at Genesis Test and Training Facility

The available data was obtained from one field test performed with a 12.25in fixed cutter bit with polycrystalline diamond compact (PDC) cutters coupled with the

9.5in vibration-assisted tool. The same principle applied to the field tests performed at CTTF with the 7in tool is used in the 9.5in tool field test.

Figure 3.5: 12.25 fixed cutter bit with polycrystalline diamond compact (PDC) cutters that was used in the field tests performed with the 9.5in vibration-assisted tool at Genesis Test and Training Facility.

Field test with the 9.5in tool coupled with PDC drill bit

The test was performed with a constant constant 8klbf of WOB and with a varying the excitation frequency. However, the positive displacement motor used in the 9.5in tool field test is different from the PDM used in the 7in tests. Even though the PDM used in this field test can reach higher mud flow rates, the ratio revolution per gallon is lower than the PDM used in the 7in field tests (see α in Tab. 2.1). Since the the ratio revolution per gallon (α) is also used to calculate the excitation frequency (see Eq. 2.16), the 9.5in tool exhibits a lower excitation frequency range (8.9Hz to 12.6Hz).

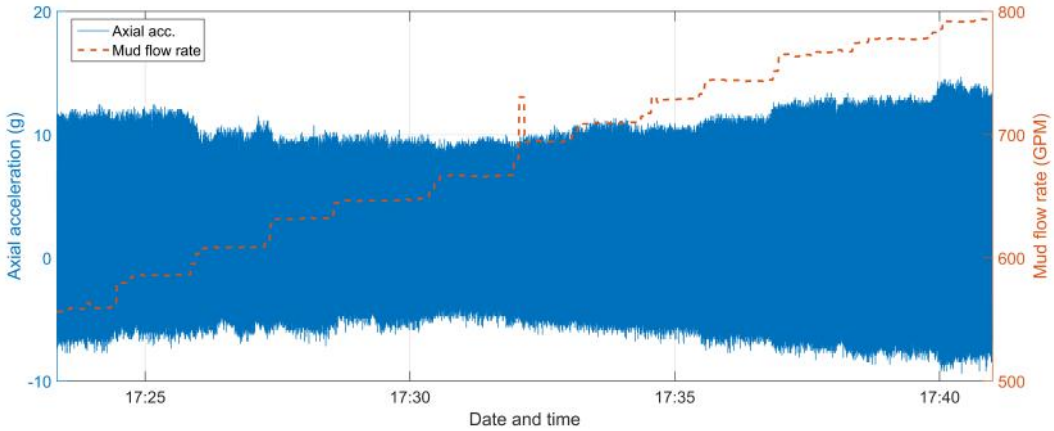

Figure 3.6: Overview of the axial vibration field data of the sensor data located at x_1 (bit assembly) during the 9.5in tool test (PDC bit). This test was performed with a constant weight-on-bit of 4klbf and with a varying mud flow rate from 560 to 790GPM.

The test evaluated the dynamic response of the tool through a mud flow sweep from 560GPM to 790GPM (8.9Hz to 12.6Hz). In general, this test was performed with mud flow increments of 20GPM (0.3Hz) with the exception of a 30GPM (0.5Hz) increase from 580 to 610GPM (9.2Hz to 9.7Hz). The axial vibration data recorded by the measurement sub located at the bit assembly (x_1) is presented in Fig. 3.6.

After analyzing the field data of 9.5in tool coupled with PDC drill bit (see Fig. 3.6), there were 12 events that were selected to be included in the validation process, as described in Table 3.3.

Run	Test - 9.5in Tool @ GTTF	
Major Events	Date & Time	Mud Flow Rate (Excitation Frequency)
1st	21/09/2016 17:23 - 17:24	560GPM (8.9Hz)
2nd	21/09/2016 17:24 - 17:25	580GPM (9.2Hz)
3rd	21/09/2016 17:26 - 17:27	610GPM (9.7Hz)
4th	21/09/2016 17:27 - 17:28	630GPM (10.0Hz)
5th	21/09/2016 17:29 - 17:30	650GPM (10.3Hz)
6th	21/09/2016 17:30 - 17:32	670GPM (10.7Hz)
7th	21/09/2016 17:32 - 17:33	690GPM (11.0Hz)
8th	21/09/2016 17:33 - 17:34	710GPM (11.3Hz)
9th	21/09/2016 17:34 - 17:35	730GPM (11.6Hz)
10th	21/09/2016 17:35 - 17:37	750GPM (11.9HZ)
11th	21/09/2016 17:37 - 17:38	770GPM (12.3Hz)
12th	21/09/2016 17:40 - 17:41	790GPM (12.6Hz)

Table 3.3: Major events selected from the 9.5in tool coupled with PDC drill bit at GTTF to be used in the validation process.

In summary, the complete set of data from all the 7in tool tests resulted in a set of 16 events to be evaluated within the validation process of the mathematical model for the 7in tool. Additionally, the complete set of data from the 9.5in tool test resulted in a set of 12 events to be evaluated within the validation process of the mathematical model for the 9.5in tool.

3.2 Model Calibration

The initial step of the validation process consists of a calibration phase, as represented by Fig. 3.7. The first step is define an event from the available field data to calibrate the mathematical model. Next, the calibrated mathematical model is employed to reproduce the other recorded events changing only the excitation frequency (mud flow rate). If the simulated results reveal a poor match with the remaining field data events, the calibration process is restarted. Another event is then used to calibrate the mathematical model, and the process is repeated. The calibrated mathematical model should be able to reproduce the other recorded events changing only the drilling parameters: weight-on-bit and mud flow rate.

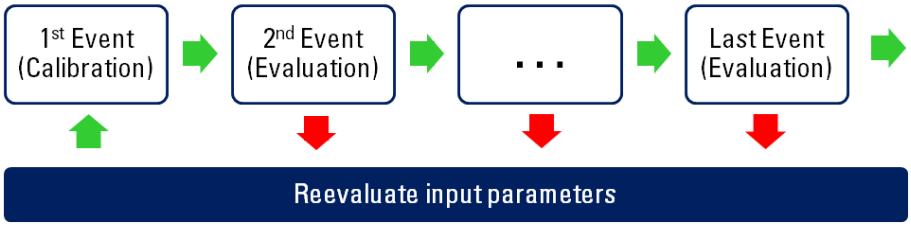

Figure 3.7: Flowchart representative of the validation process of the model

Although most of the mechanical and geometrical properties of each component of the tool are known, the impact coefficients, which are stiffness and damping derived from the impact model, are unknown. Furthermore, the viscous damping coefficient of the seventh degree-of-freedom (MWD sub) should be adjusted to mitigate the effects of the reflected shock waves caused by the impact dynamics. Therefore, the impact coefficients for each impact surface and the damping coefficient of x_7 (MWD sub) are chosen, such that the axial response of the mathematical model is close to the the field data response.

In this analysis, three parameters are selected to evaluate the main characteristics of each axial acceleration data: the average axial vibration peaks, the impact frequency and the dynamic behavior. The first parameter the uses the maximum axial vibration peaks, which are detected in fixed 200ms intervals, to obtain the average acceleration peak values correspondent to their respective excitation frequency. The impact frequency evaluates the number of impact cycles that occur in one second. The impact cycle is defined as the time window recorded between two major acceleration peaks, assuming a periodic behavior. This definition of the impact cycle is based on the hypotheses that the highest axial vibration peaks occurs in the exact moment of contact between the anvil assembly and the impact face. The investigation of the dynamic behavior analyses the periodicity of the system and evaluates the number of impacts in each impact cycle.

3.2.1 Calibration of the 7in tool model

The calibration process is performed by analyzing the axial acceleration data in a 1-second window and compare with the numerical results of the mathematical model, as shown in Fig. 3.8. For the 7in tool model, the 1st event (see Tab. 3.1) was selected for the calibration process, which corresponds to the field data of the 7in tool coupled with CDE drill bit with mud flow rate of 200GPM.

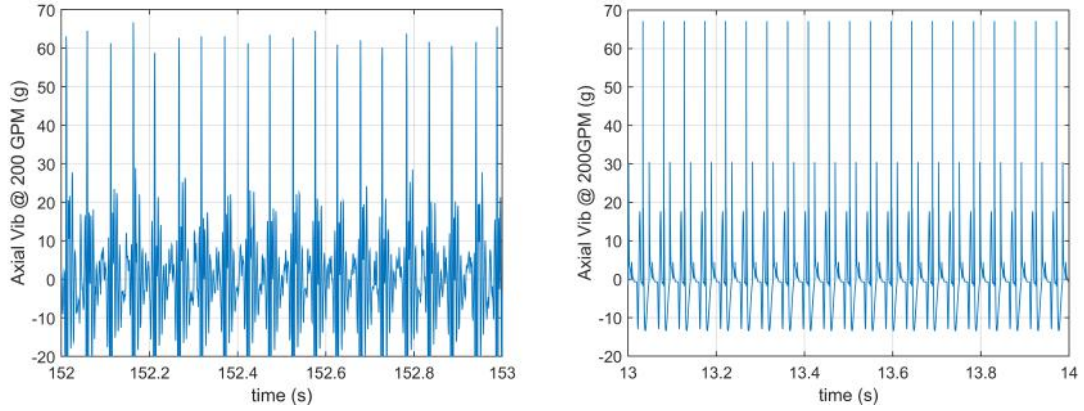

(a) (b)

Figure 3.8: (a) Axial vibration field data, and (b) simulations results, representing the sensor data located at x_1 (bit assembly), in a constant 200GPM mud flow rate scenario during the 7in tool test (CDE bit).

An analysis of the sensor data located at x_1 (bit assembly), given in Fig. 3.8a, reveals an average axial vibration peak of 65g and an impact frequency of 20Hz. The simulations results, represented in Fig. 3.8b, reveal an average axial vibration peak of 67g and an impact frequency of 21Hz.

A detailed analysis of each impact cycle, as described in Fig. 3.9a, reveals that there are three significant acceleration peaks in each cycle. In that regard, it is reasonable to assume that the highest acceleration peak is related to the impact of x_2 (anvil) into x_1 (bit assembly). However, since these measurements subs are located outside the VAD tool, it is not possible to determine the exact source that generated those other two acceleration peaks. Thus, these impacts could be related to the any of the four impact surfaces.

Furthermore, since the triaxial accelerometer inside the measurement sub is a piezoelectric transducer, the sensor dynamics could be affected by the high-energy low-frequency impacts generated by the tool. Thus, excluding the three major acceleration peaks, it is assumed that the minor acceleration oscillations in the sensor data are related to secondary factors, such as sensor dynamics, and they are not considered in this analysis.

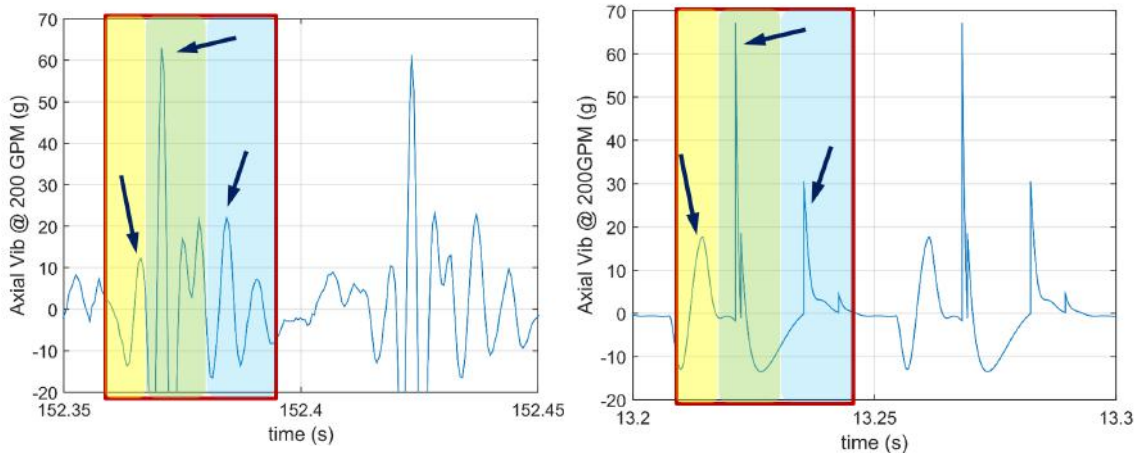

(a) (b)

Figure 3.9: Axial vibration field data (a) and simulations results (b), representing the sensor data located at x_1 (bit assembly), in a constant 200GPM mud flow rate scenario recorded in 100ms time windows - 7in tool test (CDE bit).

The simulation results, given in Fig. 3.9b, reveals that there are three significant impacts in each cycle. Furthermore, the results indicate that one of the three impacts are significantly higher than the other two. In addition, the magnitude of these secondary impacts are very similar to the ones observed in the field data. Thus, the simulation results show a good match with the field data.

3.2.2 Calibration of the 9.5in tool model

For the 9.5in tool model, the 1st event (see Tab. 3.3) was selected for the calibration process, which corresponds to the field data of the 9.5in tool coupled with PDC drill bit with mud flow rate of 560GPM.

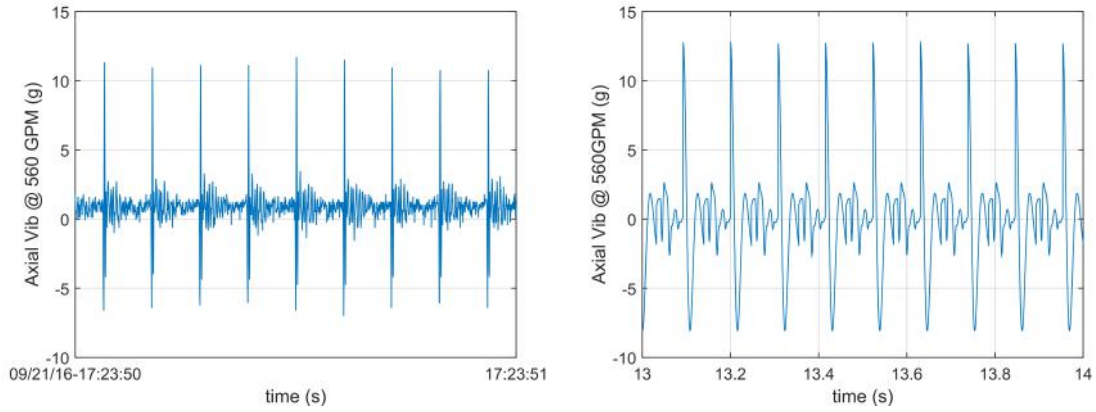

(a) (b)

Figure 3.10: (a) Axial vibration field data, and (b) simulations results, representing the sensor data located at x_1 (bit assembly), in a constant 560GPM mud flow rate scenario during the 9.5in tool test.

An analysis of the sensor data located at x_1 (bit assembly), given in Fig. 3.10a, reveals an average axial vibration peak of 11g and an impact frequency of 9Hz. The simulations results, represented in Fig. 3.10b, reveal an average axial vibration peak of 13g and an impact frequency of 9Hz.

Even though the calibration results for both 7in and 9.5in tools are qualitatively and quantitatively similar to their respective calibration events, there is an inherit limitation of available field data. Since the measurements subs (see x_1 and x_5 in Fig. 2.3) are located outside the VAD tool, it is not possible the determine the exact cause for the secondary vibration peaks with acceleration data by itself. For instance, these secondary acceleration peaks could be a related to additional impacts of the anvil (x_2) into the bit assembly (x_1), or to impacts between the anvil (x_2) and the recoil spring (located at x_3), or even a result of WOB fluctuations due to the high impact forces.

Another important aspect to consider in this analysis is the limitations associated with the sole usage of acceleration data to determine the number of impacts in each impact cycle. The triaxial accelerometer inside the measurement device is submitted to other disturbances that are not necessarily related to the axial dynamics, such as sensor dynamics. Additionally, the signal to noise ratio of the measurement device should also be taken in consideration. The accelerometers used in these field test have an maximum sensor range of 250g. Thus, the low amplitude oscillations recorded in the 9.5in tool field data are within 1-2% of the upper value of the sensor range. This results in a higher influence of the sensor dynamics in the measured data, which undermines the analysis of secondary vibration peaks.

3.3 Model Validation

The complete set of 28 events obtained from all field tests results (7in and 9.5in tools) are used in the validation process of the mathematical model. Thus, a breakdown of this data results in 16 events recorded during the field tests with the 7in tool and 12 events recorded during the field test with the 9.5in tool.

The results include an analysis of the acceleration data, in the time domain, for each flow rate to understand the relation between the dynamic behavior of the tool with the mud flow rate. Furthermore, an investigation of the relation between the axial vibration peaks and of the mud flow rate is proposed for all field tests to evaluate the overall behavior of the system. It is important to mention that the simulation results from the 7in tool test coupled with the RC drill bit are obtained by changing only the drilling parameters and the drill bit mass. Thus, the impact coefficients and other calibrated parameters remain unchanged with the exchange of drill bits.

3.3.1 Field data versus simulation results for the 7in tool coupled with CDE bit

2nd Event - axial vibration results at 250GPM (26.7Hz)

An analysis of the sensor data located at x_1 (bit assembly), given in Fig. 3.11a, reveals an average axial vibration peak of 68g and an impact frequency of 24Hz. Furthermore, an investigation of the dynamic behavior for each impact cycle seems to indicate that there are three relevant impacts per cycle. The simulation results, represented in Fig. 3.11b, reveal an average axial vibration peak of 89g, an impact frequency of 26Hz and seem to indicate that there are three relevant impacts per cycle. Thus, an evaluation of the simulation results shows a good match on the impact frequency and number of impacts per cycle, as well as a poor match on the average axial vibration peaks, when compared with the experimental data.

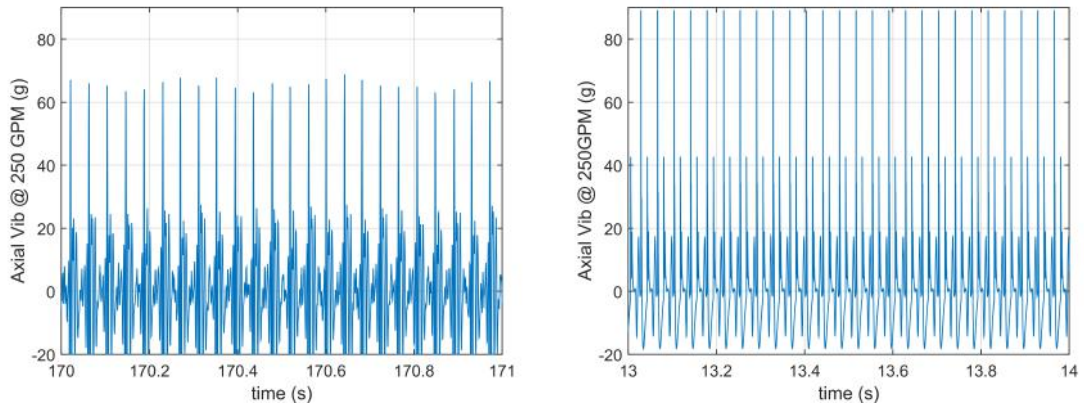

(a) (b)

Figure 3.11: Axial vibration field data (a) and simulations results (b), representing the sensor data located at x_1 (bit assembly), in a constant 250GPM mud flow rate scenario and 4klbf of weight-on-bit, during the 7in prototype test (CDE bit).

3rd Event - axial vibration results at 300GPM (31.2Hz)

An analysis of the measurement sub data located at x_1 (bit assembly), given in Fig. 3.12a, reveals an average axial vibration peak of 49g and an investigation of the dynamic behavior seems to indicate an aperiodic behavior. The simulation results, represented in Fig. 3.12b, reveal a quasi-periodic behavior with an average axial vibration peak of 69g, an impact frequency of 32Hz and seem to indicate that there are three relevant impacts per cycle. Thus, an evaluation of the simulation results shows a poor match on both the dynamic behavior and the average axial vibration peaks.

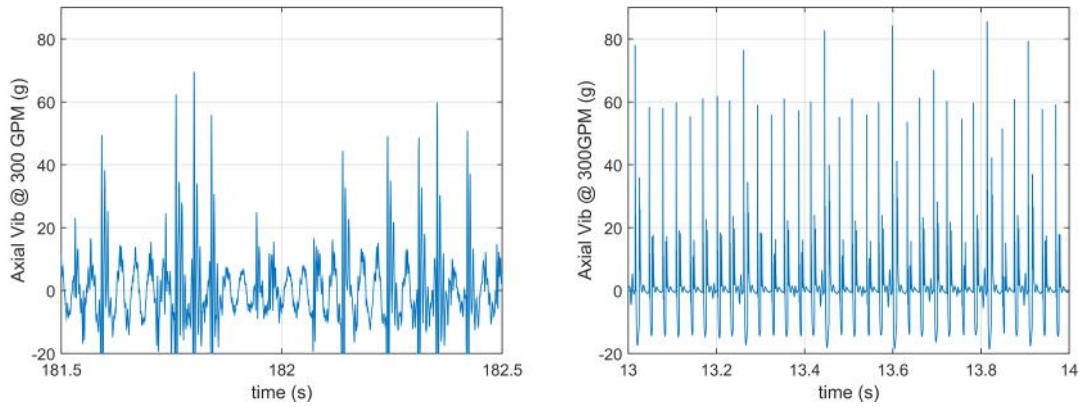

(a) (b)

Figure 3.12: Axial vibration field data (a) and simulations results (b), representing the sensor data located at x_1 (bit assembly), in a constant 300GPM mud flow rate scenario and 4klbf of weight-on-bit, during the 7in prototype test (CDE bit).

4th Event - axial vibration results at 350GPM (37.3Hz)

An analysis of the measurement sub data located at x_1 (bit assembly) for 350GPM, given in Fig. 3.13a, reveals an average axial vibration peak of 69g and an investigation of each impact cycle seems to indicate that there is a change in the dynamic behavior of the system, when compared with the calibration event (see Fig. 3.9a). The periodic behavior observed in the previous event degenerates into an aperiodic behavior. In that sense, both the impacts per cycle and impact frequency analysis loose significance in a general approach due to the irregular nature of the response.

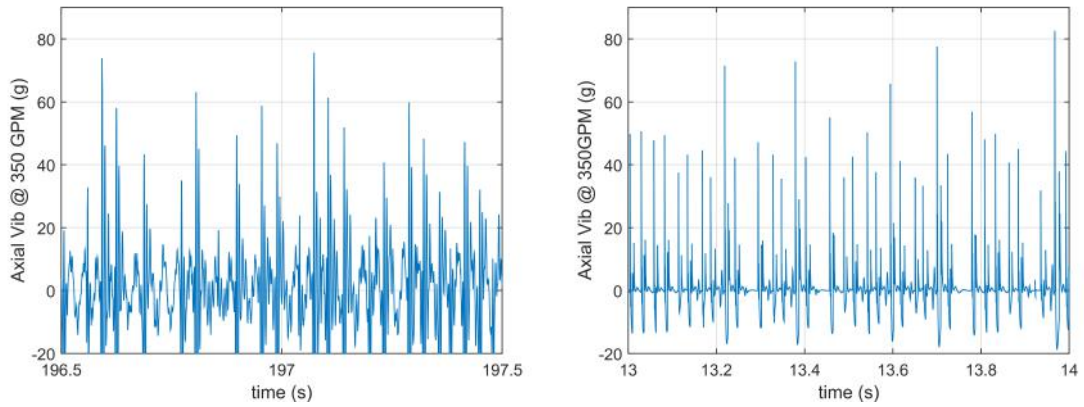

(a) (b)

Figure 3.13: Axial vibration field data (a) and simulations results (b), representing the sensor data located at x_1 (bit assembly), in a constant 350GPM mud flow rate scenario and 4klbf of weight-on-bit, during the 7in prototype test (CDE bit).

The simulation results, represented in Fig. 3.13b, reveal an average axial

vibration peak of 54g and an investigation of the dynamic behavior for each impact cycle seems to indicate an aperiodic behavior. Thus, an evaluation of the simulation results shows a good match with the field data. In addition, the axial vibration peaks dispersion observed in the experimental data is reproduced in the simulation results.

5th Event - axial vibration results at 400GPM (42.7Hz)

An analysis of the measurement sub data located at x_1 (bit assembly) for 400GPM, given in Fig. 3.14a, reveals an average axial vibration peak of 37g and an investigation of each impact cycle seems to indicate an aperiodic behavior. The simulation results, represented in Fig. 3.14b, reveal an average axial vibration peak of 40g and an investigation of the dynamic behavior for each impact cycle seems to indicate an aperiodic behavior. Thus, an evaluation of the simulation results shows a good match with the field data. In addition, the axial vibration peaks dispersion observed in the experimental data is satisfactory reproduced in the simulation results.

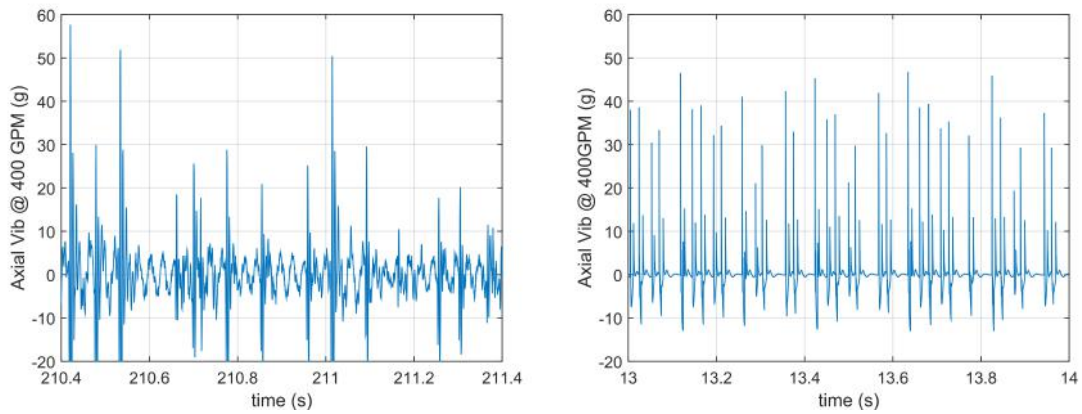

(a) (b)

Figure 3.14: Axial vibration field data (a) and simulations results (b), representing the sensor data located at x_1 (bit assembly), in a constant 400GPM mud flow rate scenario and 4klbf of weight-on-bit, during the 7in prototype test (CDE bit).

6th Event - axial vibration results at 450GPM (48.0Hz)

An analysis of the sensor data at x_1 (bit assembly), given in Fig. 3.15a, reveals an average axial vibration peak of 22g and an investigation of the dynamic behavior for each impact cycle seems to indicate an aperiodic behavior. The simulation results, represented in Fig. 3.15b, reveal an average axial vibration peak of 32g and an investigation of the dynamic behavior for each impact cycle seems to indicate an aperiodic behavior. Thus, an evaluation of the simulation results shows a satisfactory

match in dynamic behavior and a poor match regarding the average axial vibration peaks.

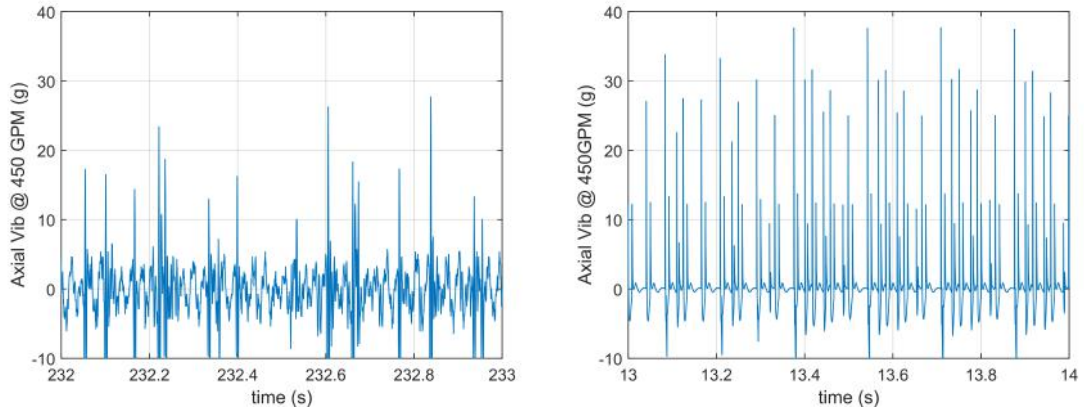

(a) (b)

Figure 3.15: Axial vibration field data (a) and simulations results (b), representing the sensor data located at x_1 (bit assembly), in a constant 450GPM mud flow rate scenario and 4klbf of weight-on-bit, during the 7in prototype test (CDE bit).

7th Event - axial vibration results at 500GPM (53.3Hz)

An analysis of the measurement sub data located at x_1 (bit assembly) for 500GPM, given in Fig. 3.16a, reveals an average axial vibration peak of 16g and an investigation of the dynamic behavior for each impact cycle seems to indicate an apparently aperiodic behavior.

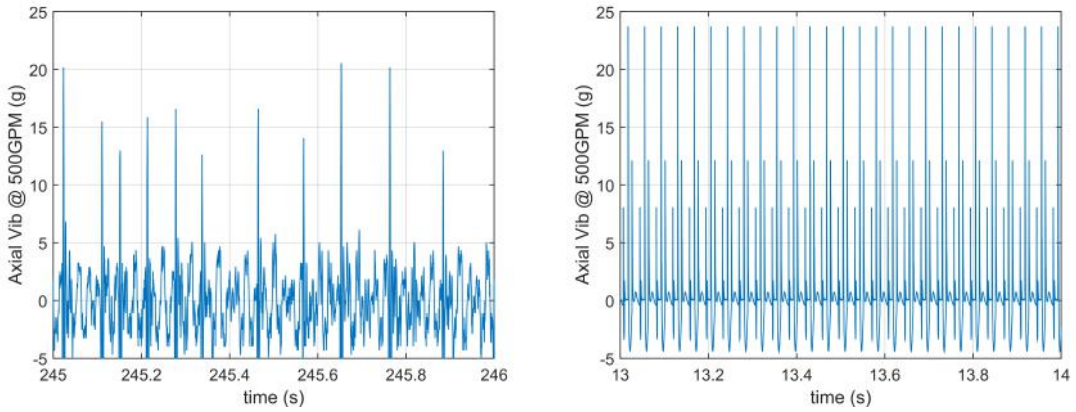

(a) (b)

Figure 3.16: Axial vibration field data (a) and simulations results (b), representing the sensor data located at x_1 (bit assembly), in a constant 500GPM mud flow rate scenario and 4klbf of weight-on-bit, during the 7in prototype test (CDE bit).

The simulation results, represented in Fig. 3.16b, reveal an average axial vibration peak of 24g, an impact frequency of 27Hz and seem to indicate that there

are two relevant impacts per cycle. The aperiodic behavior observed in the previous events returns to a periodic behavior. Moreover, this characteristic of a seemingly aperiodic behavior of the experimental data combined with the periodic behavior of the simulation results will persist at high flow rate events. Thus, an evaluation of the simulation results shows a poor match on the dynamic behavior of the system when compared with the field data.

8th Event - axial vibration results at 550GPM (58.6Hz)

An analysis of the sensor data at x_1 (bit assembly), given in Fig. 3.17a, reveals an average axial vibration peak of 14g and an investigation of the dynamic behavior for each impact cycle seems to indicate an aperiodic behavior. The simulation results, represented in Fig. 3.17b, reveal a periodic behavior with an average axial vibration peak of 25g, an impact frequency of 59Hz and seem to indicate that there are two relevant impacts per cycle. Thus, an evaluation of the simulation results shows a poor match on the dynamic behavior, as well as a poor match on the average axial vibration peaks, when compared with the experimental data.

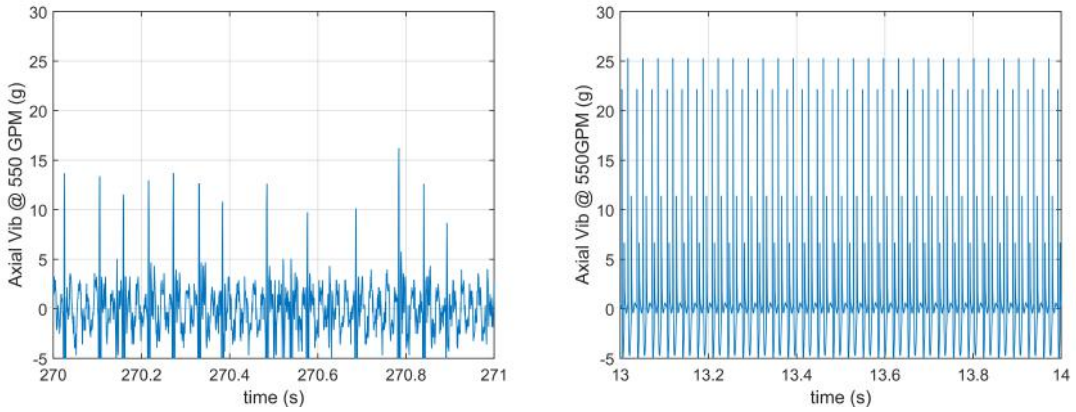

(a) (b)

Figure 3.17: Axial vibration field data (a) and simulations results (b), representing the sensor data located at x_1 (bit assembly), in a constant 550GPM mud flow rate scenario and 4klbf of weight-on-bit, during the 7in prototype test (CDE bit).

9th Event - axial vibration results at 600GPM (64.0Hz)

An analysis of the sensor data at x_1 (bit assembly), given in Fig. 3.18a, reveals an average axial vibration peak of 13g and an investigation of the dynamic behavior for each impact cycle seems to indicate an aperiodic behavior. The simulation results, represented in Fig. 3.18b, reveal a periodic behavior with an average axial vibration peak of 24g, an impact frequency of 65Hz and seem to indicate that there are two relevant impacts per cycle. Thus, an evaluation of the simulation results shows a

poor match on the dynamic behavior, as well as a poor match on the average axial vibration peaks, when compared with the experimental data.

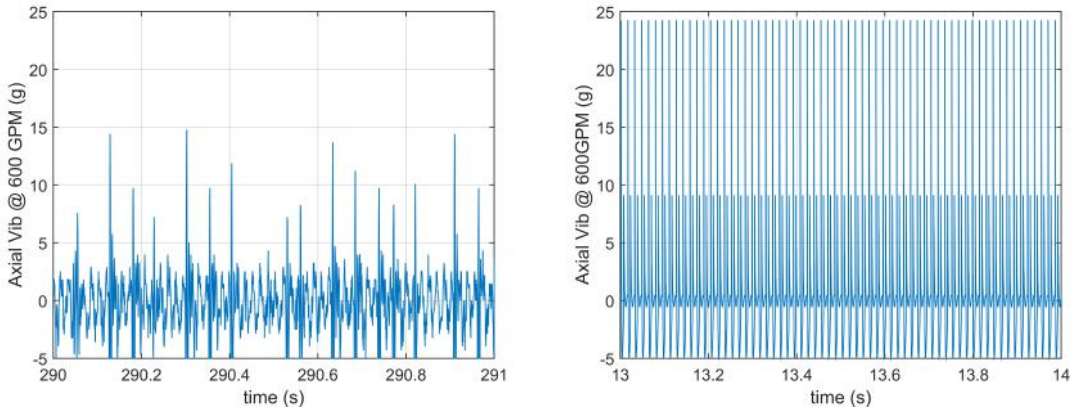

(a) (b)

Figure 3.18: Axial vibration field data (a) and simulations results (b), representing the sensor data located at x_1 (bit assembly), in a constant 600GPM mud flow rate scenario and 4klbf of weight-on-bit, during the 7in prototype test (CDE bit).

10th Event - axial vibration results at 650GPM (69.3Hz)

An analysis of the sensor data at x_1 (bit assembly), given in Fig. 3.19a, reveals an average axial vibration peak of 11g and an investigation of the dynamic behavior for each impact cycle seems to indicate an aperiodic behavior.

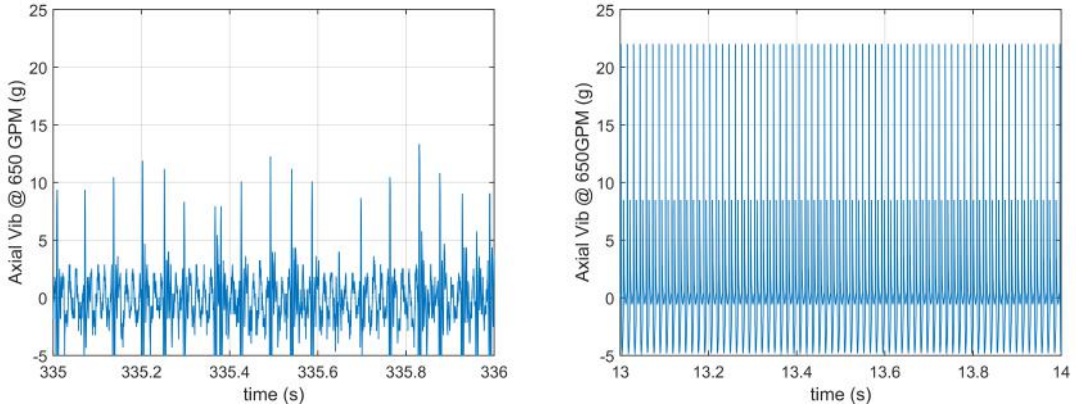

(a) (b)

Figure 3.19: Axial vibration field data (a) and simulations results (b), representing the sensor data located at x_1 (bit assembly), in a constant 650GPM mud flow rate scenario and 4klbf of weight-on-bit, during the 7in prototype test (CDE bit).

The simulation results, represented in Fig. 3.19b, reveal a periodic behavior with an average axial vibration peak of 22g, an impact frequency of 70Hz and seem to indicate that there are two relevant impacts per cycle. Thus, an evaluation of the

simulation results shows a poor match on the dynamic behavior, as well as a poor match on the average axial vibration peaks, when compared with the experimental data.

Event summary: axial vibration peaks

From Fig. 3.20a, it is possible to analyze the dispersion of the axial vibration peaks for each excitation frequency. For a given mud flow rate, each maximum acceleration peak obtained in this analysis is represented as a point in Fig. 3.20a. During the initial stages of the field test, which coincides with the low excitation frequency range (mud flow rate), the axial vibration peaks data reveals high peak amplitudes and relatively low dispersion. Next, as the excitation frequency is increased, the system exhibits an increase in the maximum peaks observed. In contrast, there is also a higher dispersion of those peaks, which, as revealed by the both the field data and simulation results, shows a lower average axial vibration peaks than the previous region. This phenomenon ends at higher excitation frequencies, where the peak amplitudes are greatly reduced and the dispersion is also reduced. The analysis of the axial vibration data of the measurement device located at x_1 (bit assembly) reveals that there is a significant reduction in the axial vibrations peaks, when compared to the acceleration data recorded at x_5 (measurement sub).

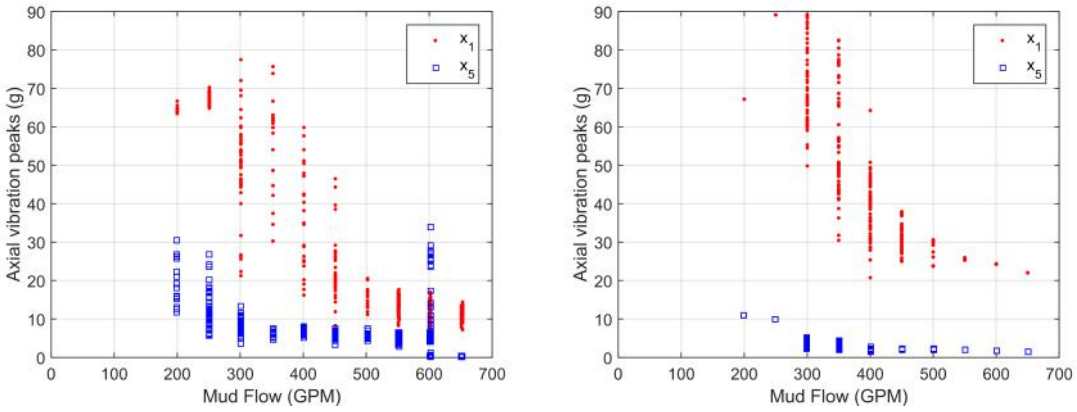

(a) (b)

Figure 3.20: Axial vibration field data (a) and simulations results (b) of the sensor located at x_1 (red dots) and the sensor located at x_5 (blue squares) obtained in a mud flow sweep scenario from 200 to 650GPM for the 7in tool test (CDE bit).

The simulation results, represented in Fig. 3.20b, show a good overall match in axial vibration peaks (average and dispersion) when compared with the data measured at x_1 (bit assembly) recorded in the field test. The mathematical model is also able to recreate the axial vibration peak levels as a function of the mud flow. Furthermore, the increase in dispersion of the axial vibration peaks occurs

between 300 and 400GPM, which is compatible with the measured field data at x_1 (bit assembly). The analysis of the axial vibration data of the measurement device located at x_5 (measurement sub) are partially in accordance to the field test data, which seems to reveals that, even though the tool is generating high levels of axial vibration close to the bit assembly (x_1), the effects of these impacts are mitigated by other components of this assembly, reducing the axial vibration levels that are transmitted to the drill pipes located above the assembly. However, the simulation results show a lower axial vibration peaks (average and dispersion) when considering the measurement device located at x_5 (measurement sub). A further analysis of the test data revealed that, during the drilling operation, severe lateral vibrations were observed, and, such severe vibrations, could affect the axial vibration measurements. Since the mathematical model does not consider the axial-lateral coupling, this could be a possible explanation for the poor match in the acceleration data recorded at x_5 (measurement sub).

Regarding the last topic, the field data from the 7in tool test coupled with CDE drill bit seems to indicate that the axial vibration peaks, given in Figure 3.21a, may be affected by the lateral vibration, given in Figure 3.21b, hence the axial-lateral coupling. Since the lateral motion is not considered in this model, the model is not able to capture the effects of the axial-lateral coupling.

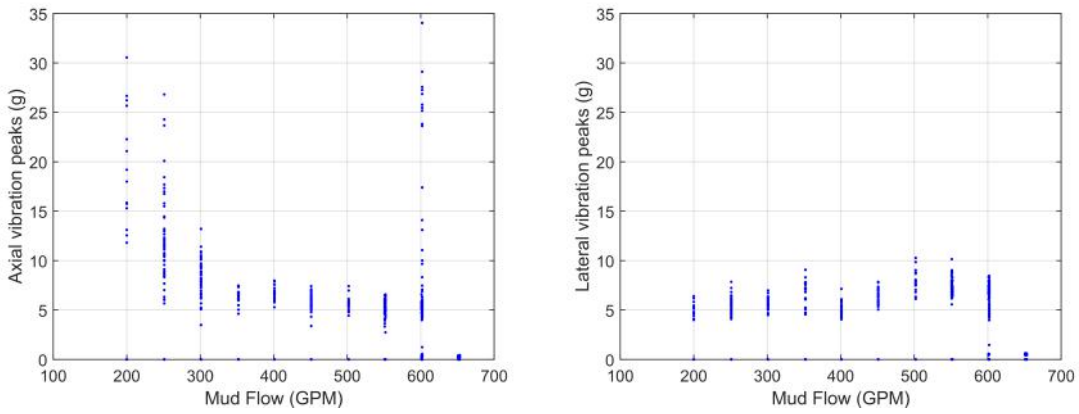

(a) (b)

Figure 3.21: Axial vibration peaks (a) and lateral vibration peaks (b) obtained from the field data at measurement sub (x_5) in a mud flow sweep scenario from 200 to 500GPM for the 7in tool test (CDE bit).

Moreover, there seems to be a relation between the dynamic behavior of the system and the the axial vibration peaks dispersion. By definition, if a system exhibits a periodic behavior, there would be no dispersion in the axial vibration peaks, as seen in the mathematical model. However, the field data exhibits a small dispersion of the axial vibration peaks. A more detailed analysis of the acceleration data shows that the low dispersion is linked with small disturbances that affect

the axial dynamics, such as sensor dynamics. If the system exhibits an aperiodic behavior, there should be a considerable variation in the axial vibration peaks. This, in turn, would translate into a high dispersion of the axial vibration peaks, which is observe in both the simulation results and field data.

3.3.2 Field data versus simulation results for the 7in tool coupled with RC bit

The main difference between the previous run and the current run is the drill bit that was used, since there is a change from a CDE bit to a roller cone bit. Thus, the input parameters of the mathematical model must be updated to accommodate this change. In that sense, the bit mass is the only parameter that is updated, since the roller cone bit is lighter than the CDE bit. It is worth mentioning that the difference in bit-rock interaction in the cutting action is not considered.

11th Event - axial vibration results at 200GPM (21.3Hz)

An analysis of the sensor data located at x_1 (bit assembly), given in Fig. 3.22a, reveals an average axial vibration peak of 82g and an impact frequency of 19Hz. The simulation results, represented in Fig. 3.22b, reveal an average axial vibration peak of 76g, an impact frequency of 21Hz.

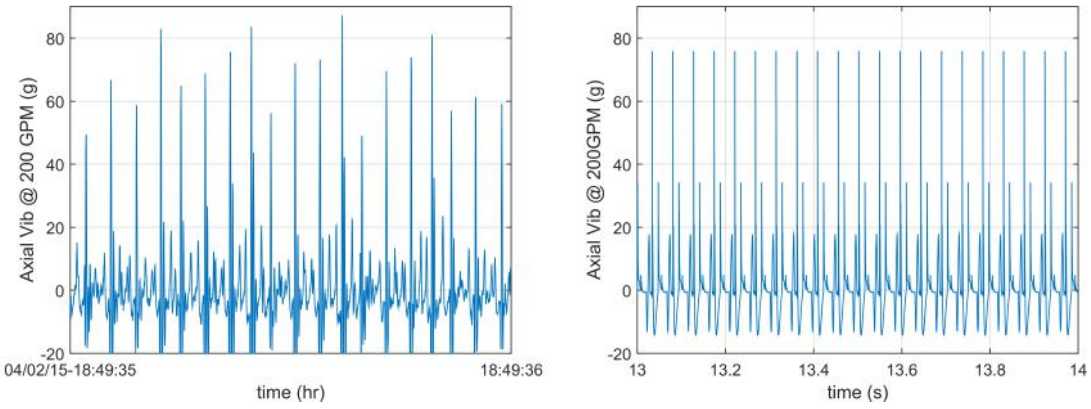

(a) (b)

Figure 3.22: Axial vibration field data (a) and simulations results (b), representing the sensor data located at x_1 (bit assembly), in a constant 200GPM mud flow rate scenario during the 7in tool test (RC bit).

A detailed analysis of each impact cycle, as described in Fig. 3.23a, reveals that there are three significant impacts in each cycle. Additionally, the experimental data indicates that one of the three impacts is significantly higher than the other two. A related point to consider is that there are further oscillations in the sensor

data that are not acknowledged as impact. The simulation results, given in Fig. 3.23b, reveals that there are three significant impacts in each cycle, and that one of the three impacts are significantly higher than the other two. Thus, an evaluation of the mathematical model shows a good match of the impact dynamics revealed in the field data.

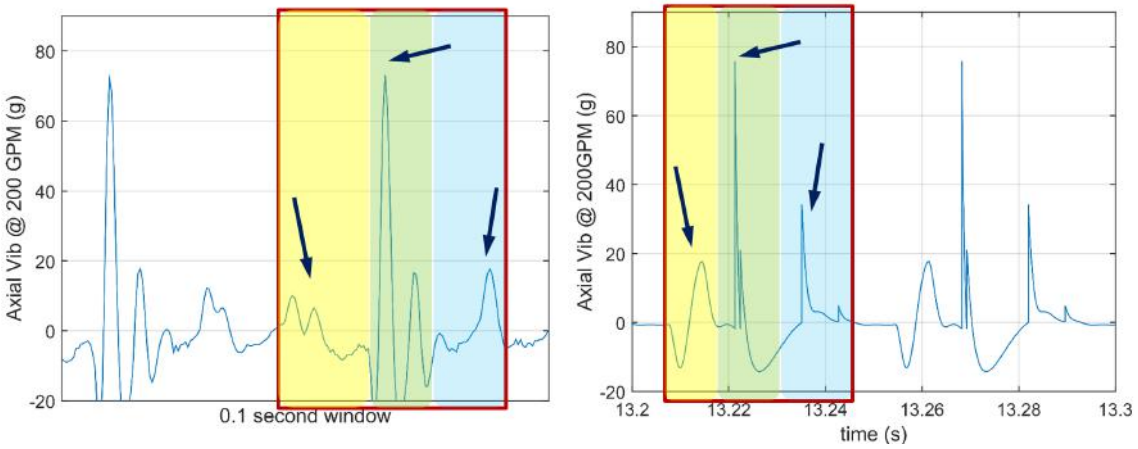

(a) (b)

Figure 3.23: Axial vibration field data (a) and simulations results (b), representing the sensor data located at x_1 (bit assembly), in a constant 200GPM mud flow rate scenario recorded in 100ms time windows - 7in tool test (RC bit).

12th Event - axial vibration results at 300GPM (31.2Hz)

An analysis of the measurement sub data located at x_1 (bit assembly), given in Fig. 3.24a, reveals an average axial vibration peak of 87g and an impact frequency of 29Hz. Furthermore, an investigation of the dynamic behavior for each impact cycle seems to indicate that there are two relevant impacts per cycle.

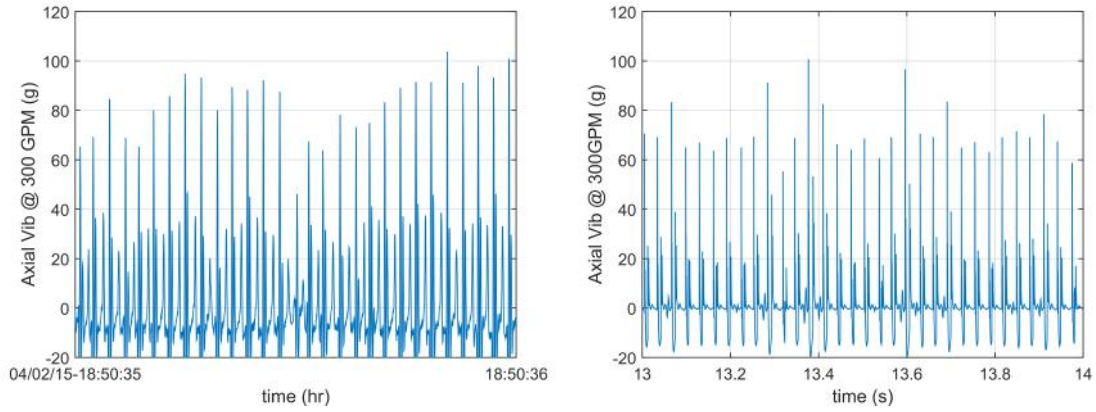

(a) (b)

Figure 3.24: Axial vibration field data (a) and simulations results (b), representing the sensor data located at x_1 (bit assembly), in a constant 300GPM mud flow rate scenario and 4klbf of weight-on-bit, during the 7in prototype test (RC bit).

The simulation results, represented in Fig. 3.24b, reveal an average axial vibration peak of 78g, an impact frequency of 32Hz and seem to indicate that there are two relevant impacts per cycle. Thus, an evaluation of the simulation results shows a good match on the impact frequency and number of impacts per cycle, as well as a satisfactory match on the average axial vibration peaks, when compared with the experimental data.

13th Event - axial vibration results at 350GPM (37.3Hz)

An analysis of the sensor data located at x_1 (bit assembly), given in Fig. 3.25a, reveals an average axial vibration peak of 61g and an investigation of the dynamic behavior for each impact cycle seems to indicate an aperiodic behavior.

The simulation results, represented in Fig. 3.25b, reveal an average axial vibration peak of 61g and an investigation of the dynamic behavior for each impact cycle seems to indicate an aperiodic behavior. Thus, an evaluation of the simulation results shows a good match on both the dynamic behavior and the average axial vibration peaks when compared with the experimental data.

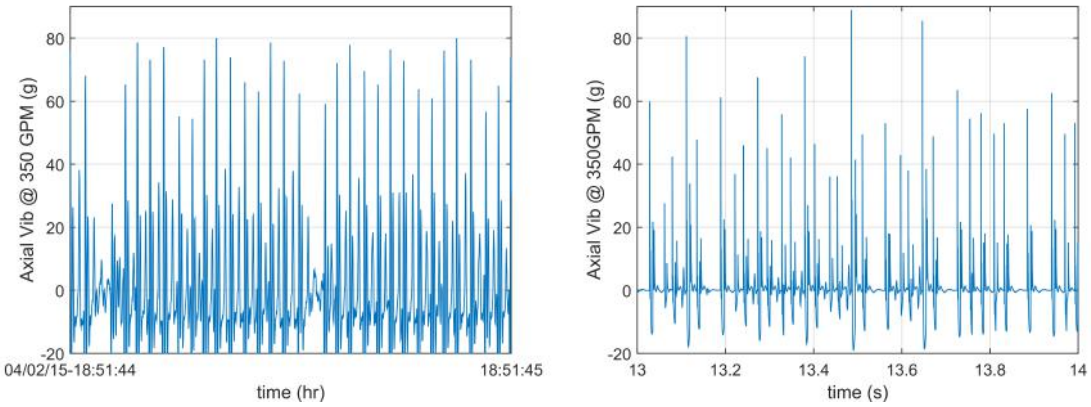

(a) (b)

Figure 3.25: Axial vibration field data (a) and simulations results (b), representing the sensor data located at x_1 (bit assembly), in a constant 350GPM mud flow rate scenario and 4klbf of weight-on-bit, during the 7in prototype test (RC bit).

14th Event - axial vibration results at 400GPM (42.7Hz)

An analysis of the sensor data at x_1 (bit assembly), given in Fig. 3.26a, reveals an average axial vibration peak of 31g and an investigation of the dynamic behavior for each impact cycle seems to indicate an aperiodic behavior. The simulation results, represented in Fig. 3.26b, reveal an average axial vibration peak of 44g and an investigation of the dynamic behavior for each impact cycle seems to indicate an aperiodic behavior. Thus, an evaluation of the simulation results shows a good

match in dynamic behavior and a poor match regarding the average axial vibration peaks. Additionally, similar to the previous test, there seems to be a relation between the dynamic behavior of the system and the the axial vibration peaks dispersion.

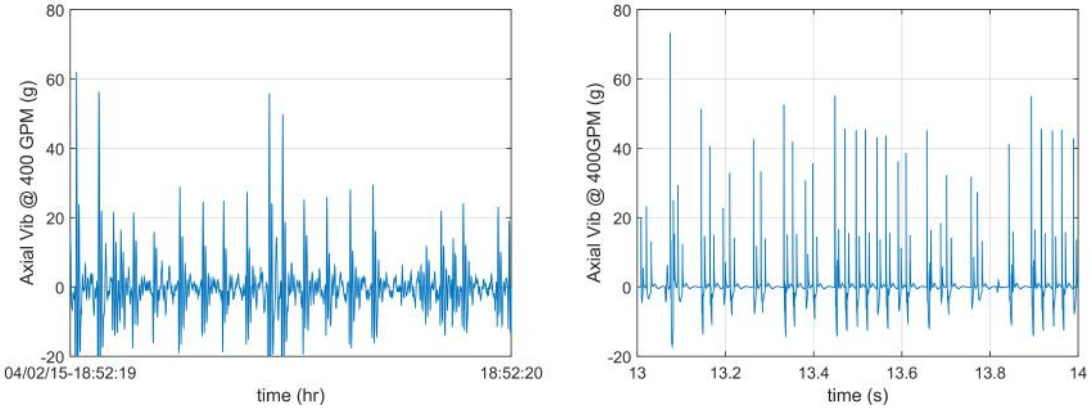

(a) (b)

Figure 3.26: Axial vibration field data (a) and simulations results (b), representing the sensor data located at x_1 (bit assembly), in a constant 400GPM mud flow rate scenario and 4klbf of weight-on-bit, during the 7in prototype test (RC bit).

15th Event - axial vibration results at 450GPM (48.0Hz)

An analysis of the sensor data at x_1 (bit assembly) is given in Fig. 3.27a, reveals an average axial vibration peak of 16g and an investigation of the dynamic behavior for each impact cycle seems to indicate an aperiodic behavior.

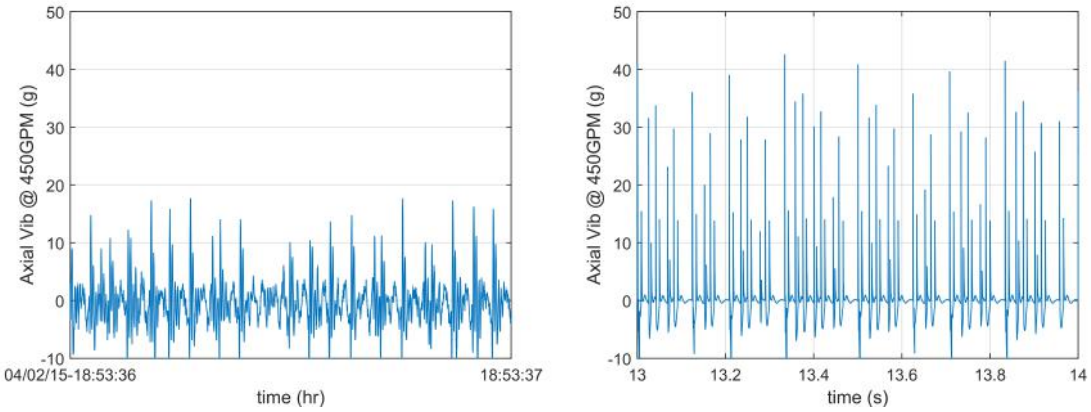

(a) (b)

Figure 3.27: Axial vibration field data (a) and simulations results (b), representing the sensor data located at x_1 (bit assembly), in a constant 450GPM mud flow rate scenario and 4klbf of weight-on-bit, during the 7in prototype test (RC bit).

The simulation results, represented in Fig. 3.27b, reveal an average axial vibration peak of 35g and an investigation of the dynamic behavior for each impact

cycle seems to indicate an aperiodic behavior. Thus, an evaluation of the simulation results shows a good match on the dynamic behavior and a poor match on the average axial vibration peaks when compared with the experimental data.

16th Event - axial vibration results at 500GPM (53.3Hz)

An analysis of the sensor data at x_1 (bit assembly), given in Fig. 3.28a, reveals an average axial vibration peak of 13g and an investigation of the dynamic behavior for each impact cycle seems to indicate an aperiodic behavior.

The simulation results, represented in Fig. 3.28b, reveal a periodic behavior with an average axial vibration peak of 27g, an impact frequency of 27Hz and seem to indicate that there are two relevant impacts per cycle. Thus, an evaluation of the simulation results shows a poor match on both the dynamic behavior and the average axial vibration peaks when compared with the experimental data.

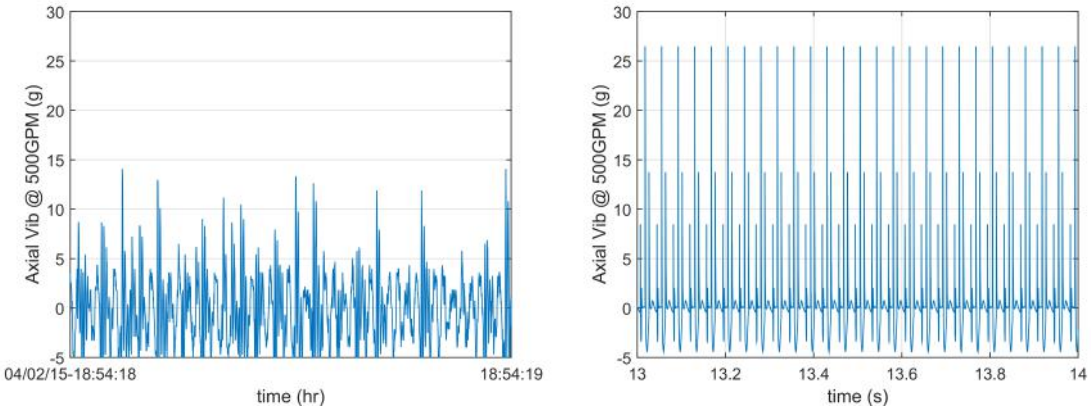

(a) (b)

Figure 3.28: Axial vibration field data (a) and simulations results (b), representing the sensor data located at x_1 (bit assembly), in a constant 500GPM mud flow rate scenario and 4klbf of weight-on-bit, during the 7in prototype test (RC bit).

Event summary: axial vibration peaks

A summary of the axial vibrations peaks in relation to the mud flow rate of the six events recorded at both sensors (x_1 and x_5) is represented in Fig. 3.29a. The results from the axial vibration data measured at x_1 (bit assembly) seem to indicate a relation between the axial vibration peak levels and dispersion as a function of the mud flow rate, as seen in the previous tool test data. The simulation results, represented in Fig. 3.29b, show a good overall match in axial vibration peaks (average and dispersion) when compared with the data measured at x_1 (bit assembly) recorded in the field test. The mathematical model is also able to recreate the axial vibration peak levels as a function of the mud flow. Furthermore, the

increase in dispersion of the axial vibration peaks occurs between 300 and 450GPM, which is compatible with the experimental data measured at x_1 (bit assembly).

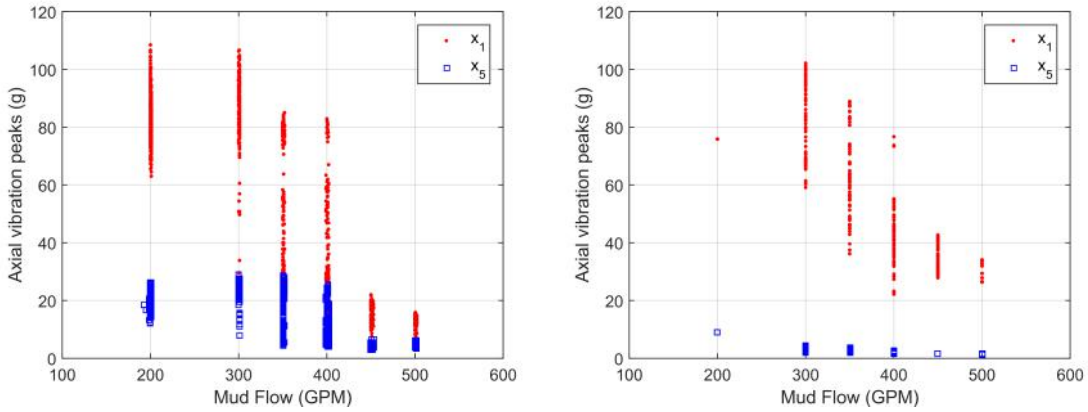

(a) (b)

Figure 3.29: Axial vibration field data (a) and simulations results (b) of the sensor located at x_1 (red dots) and the sensor located at x_5 (blue squares) obtained in a mud flow sweep scenario from 200 to 500GPM for the 7in tool test (RC bit).

As seen in the CDE test data (see Fig. 3.20), the axial vibration data of the measurement device located at x_5 (measurement sub) are partially in accordance to the field test data, as the simulation results show a lower axial vibration peaks (average and dispersion). A further analysis of the test data also revealed that severe lateral vibrations were observed, and, such severe vibrations, could affect the axial vibration measurements.

3.3.3 Field data versus simulation results for the 9.5in tool coupled with PDC bit

The calibration process of the 9.5in tool coupled with PDC bit is described in section 3.2. The main difference between the 7in and 9.5in field test is the PDM that were used. Even though the PDM used in this field test can reach higher mud flow rates, the ratio revolution per gallon is lower than the PDM used in the 7in field tests (see α in Tab. 2.1). Since the the ratio revolution per gallon (α) is also used to calculate the excitation frequency (see Eq. 2.16), the 9.5in tool exhibits a lower excitation frequency range (8.9Hz to 12.6Hz).

2nd Event - axial vibration results at 580GPM (9.2Hz)

An analysis of the sensor data located at x_1 (bit assembly), given in Fig. 3.30a, reveals an average axial vibration peak of 12g and an impact frequency of 10Hz.

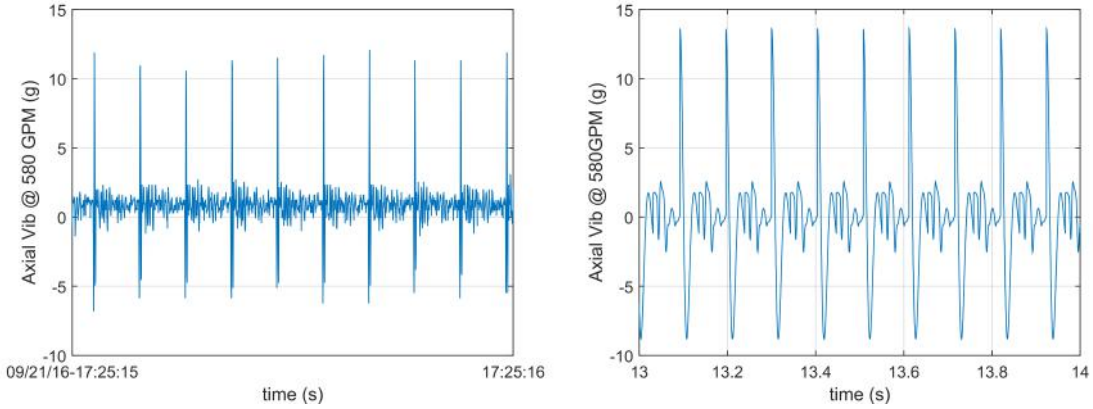

(a) (b)

Figure 3.30: Axial vibration field data (a) and simulations results (b), representing the sensor data located at x_1 (bit assembly), in a constant 580GPM mud flow rate scenario and 8klbf of weight-on-bit, during the 9.5in prototype test.

The simulation results, represented in Fig. 3.30b, reveal an average axial vibration peak of 14g and an impact frequency of 9Hz. Thus, an evaluation of the simulation results shows a good match on the impact frequency, as well as a good match on the average axial vibration peaks, when compared with the experimental data.

3rd Event - axial vibration results at 610GPM (9.7Hz)

An analysis of the sensor data located at x_1 (bit assembly), given in Fig. 3.31a, reveals an average axial vibration peak of 10g and an impact frequency of 10Hz.

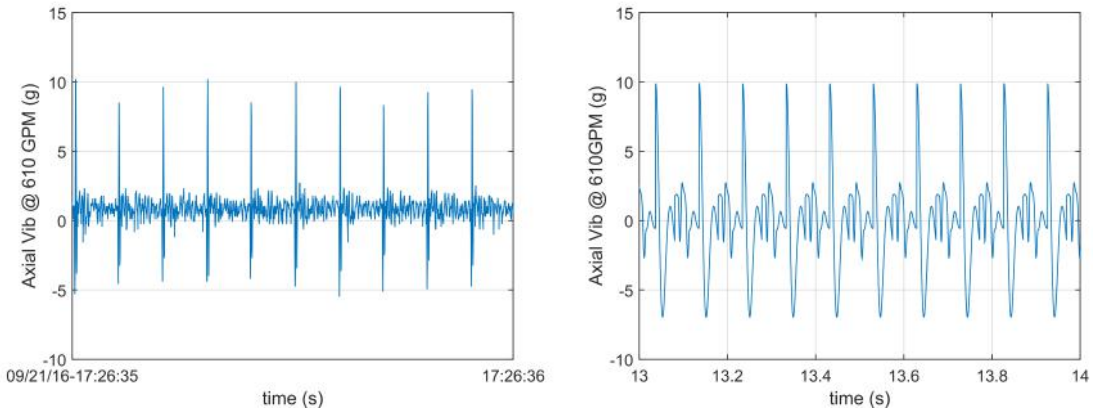

(a) (b)

Figure 3.31: Axial vibration field data (a) and simulations results (b), representing the sensor data located at x_1 (bit assembly), in a constant 610GPM mud flow rate scenario and 8klbf of weight-on-bit, during the 9.5in prototype test.

The simulation results, represented in Fig. 3.31b, reveal an average axial

vibration peak of 10g and an impact frequency of 10Hz. Thus, an evaluation of the simulation results shows a good match on the impact frequency, as well as a good match on the average axial vibration peaks, when compared with the experimental data.

4th Event - axial vibration results at 630GPM (10.0Hz)

An analysis of the sensor data located at x_1 (bit assembly), given in Fig. 3.32a, reveals an average axial vibration peak of 9g and an impact frequency of 10Hz. The simulation results, represented in Fig. 3.32b, reveal an average axial vibration peak of 8g and an impact frequency of 11Hz. Thus, an evaluation of the simulation results shows a good match on the impact frequency, as well as a good match on the average axial vibration peaks, when compared with the experimental data.

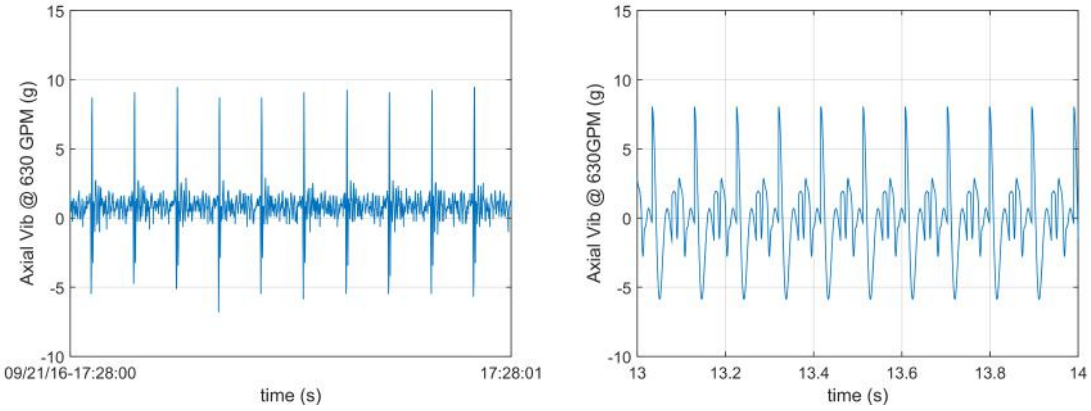

(a) (b)

Figure 3.32: Axial vibration field data (a) and simulations results (b), representing the sensor data located at x_1 (bit assembly), in a constant 630GPM mud flow rate scenario and 8klbf of weight-on-bit, during the 9.5in prototype test.

5th Event - axial vibration results at 650GPM (10.3Hz)

An analysis of the sensor data located at x_1 (bit assembly), given in Fig. 3.33a, reveals an average axial vibration peak of 9g and an impact frequency of 11Hz. The simulation results, represented in Fig. 3.33b, reveal an average axial vibration peak of 8g and an impact frequency of 11Hz. Thus, an evaluation of the simulation results shows a good match on the impact frequency, as well as a good match on the average axial vibration peaks, when compared with the experimental data.

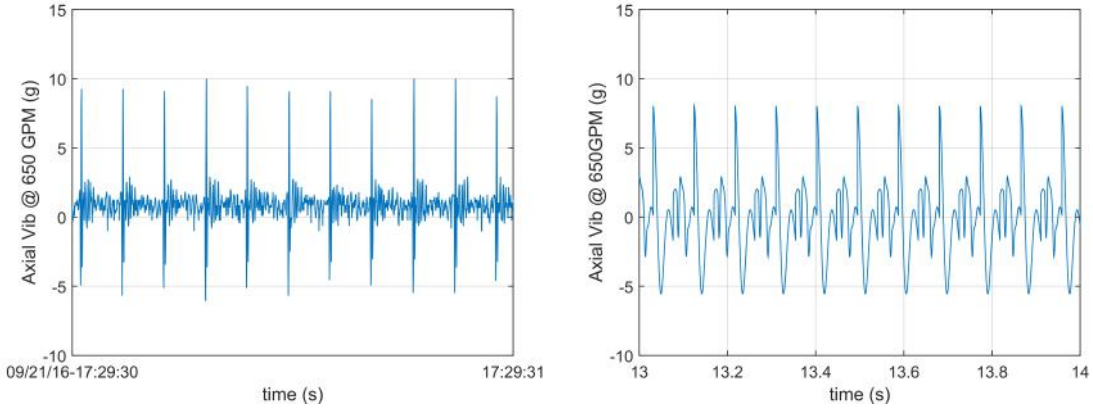

(a) (b)

Figure 3.33: Axial vibration field data (a) and simulations results (b), representing the sensor data located at x_1 (bit assembly), in a constant 650GPM mud flow rate scenario and 8klbf of weight-on-bit, during the 9.5in prototype test.

6th Event - axial vibration results at 670GPM (10.7Hz)

An analysis of the sensor data located at x_1 (bit assembly), given in Fig. 3.34a, reveals an average axial vibration peak of 9g and an impact frequency of 11Hz. The simulation results, represented in Fig. 3.34b, reveal an average axial vibration peak of 9g and an impact frequency of 11Hz. Thus, an evaluation of the simulation results shows a good match on the impact frequency, as well as a good match on the average axial vibration peaks, when compared with the experimental data.

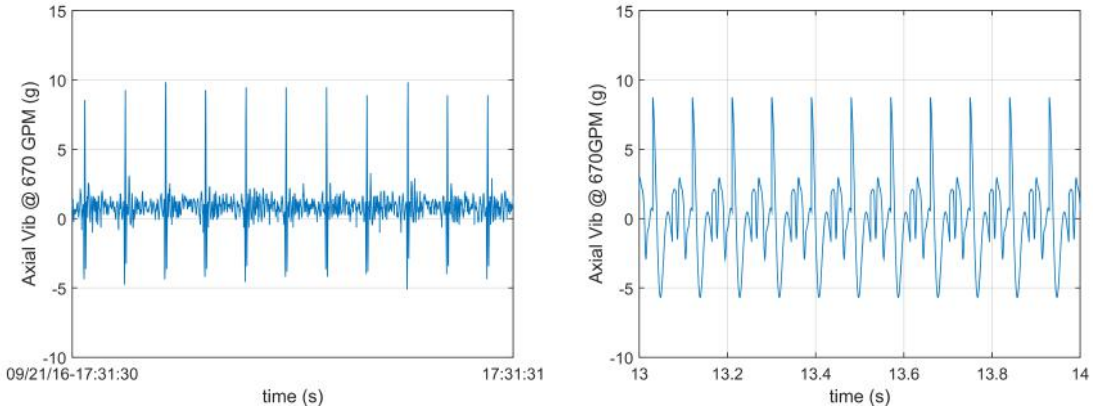

(a) (b)

Figure 3.34: Axial vibration field data (a) and simulations results (b), representing the sensor data located at x_1 (bit assembly), in a constant 670GPM mud flow rate scenario and 8klbf of weight-on-bit, during the 9.5in prototype test.

7th Event - axial vibration results at 690GPM (11.0Hz)

An analysis of the sensor data located at x_1 (bit assembly), given in Fig. 3.35a, reveals an average axial vibration peak of 10g and an impact frequency of 12Hz.

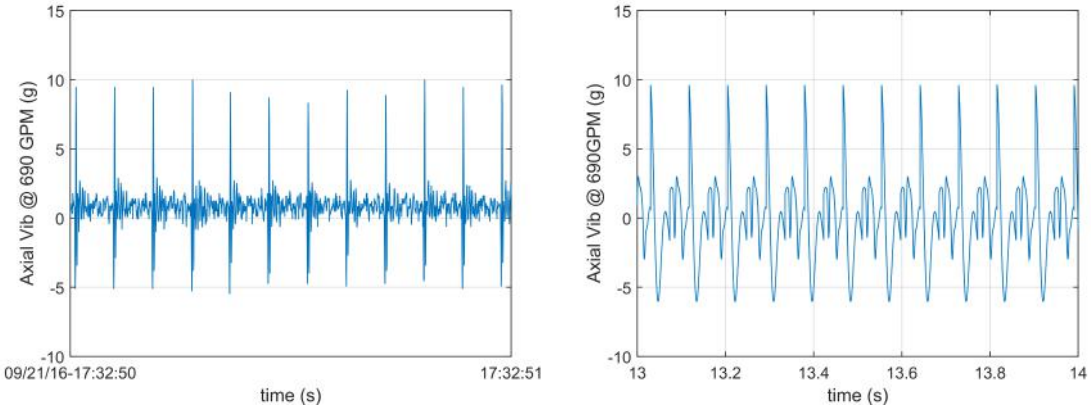

(a) (b)

Figure 3.35: Axial vibration field data (a) and simulations results (b), representing the sensor data located at x_1 (bit assembly), in a constant 690GPM mud flow rate scenario and 8klbf of weight-on-bit, during the 9.5in prototype test.

The simulation results, represented in Fig. 3.35b, reveal an average axial vibration peak of 10g and an impact frequency of 12Hz. Thus, an evaluation of the simulation results shows a good match on the impact frequency, as well as a good match on the average axial vibration peaks, when compared with the experimental data.

8th Event - axial vibration results at 710GPM (11.3Hz)

An analysis of the sensor data located at x_1 (bit assembly), given in Fig. 3.36a, reveals an average axial vibration peak of 10g and an impact frequency of 11Hz. The simulation results, represented in Fig. 3.36b, reveal an average axial vibration peak of 04g and an impact frequency of 12Hz. Thus, an evaluation of the simulation results shows a good match on the impact frequency, as well as a good match on the average axial vibration peaks, when compared with the experimental data.

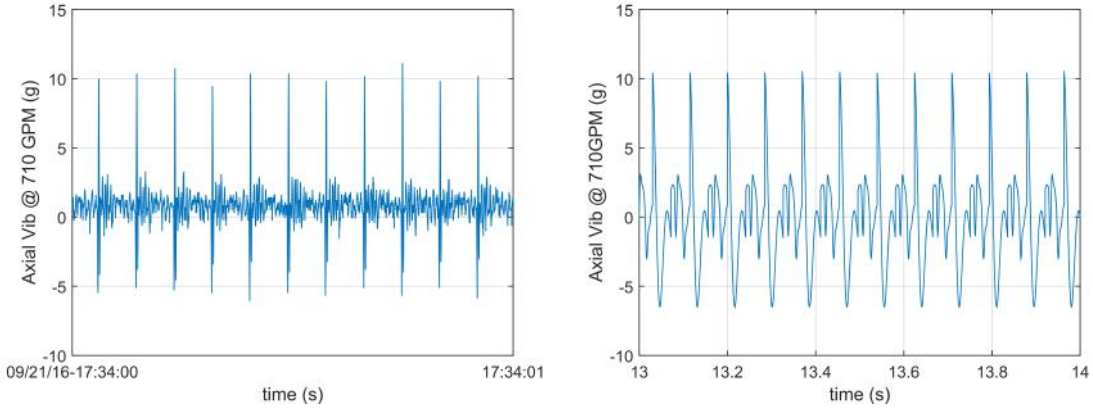

(a) (b)

Figure 3.36: Axial vibration field data (a) and simulations results (b), representing the sensor data located at x_1 (bit assembly), in a constant 710GPM mud flow rate scenario and 8klbf of weight-on-bit, during the 9.5in prototype test.

9th Event - axial vibration results at 730GPM (11.6Hz)

An analysis of the sensor data located at x_1 (bit assembly), given in Fig. 3.37a, reveals an average axial vibration peak of 10g and an impact frequency of 12Hz. The simulation results, represented in Fig. 3.37b, reveal an average axial vibration peak of 11g and an impact frequency of 12Hz. Thus, an evaluation of the simulation results shows a good match on the impact frequency, as well as a good match on the average axial vibration peaks, when compared with the experimental data.

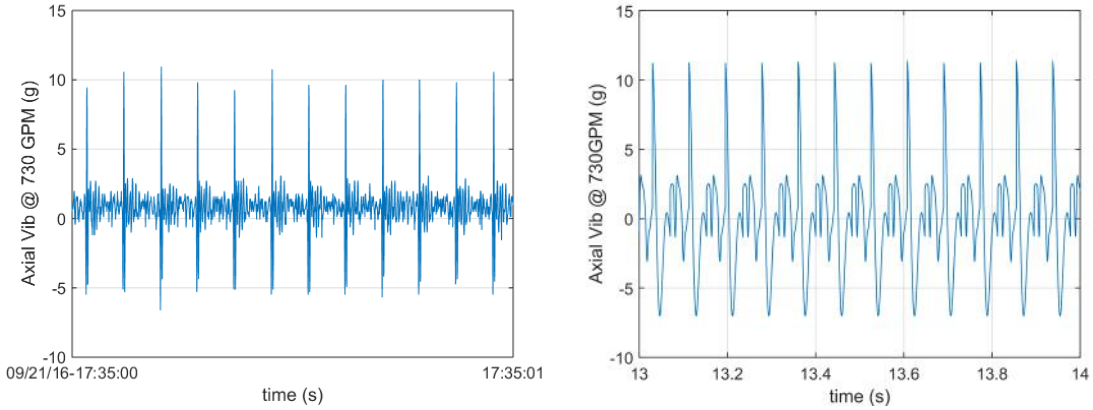

(a) (b)

Figure 3.37: Axial vibration field data (a) and simulations results (b), representing the sensor data located at x_1 (bit assembly), in a constant 730GPM mud flow rate scenario and 8klbf of weight-on-bit, during the 9.5in prototype test.

10th Event - axial vibration results at 750GPM (11.9Hz)

An analysis of the sensor data located at x_1 (bit assembly), given in Fig. 3.38a, reveals an average axial vibration peak of 11g and an impact frequency of 12Hz. The simulation results, represented in Fig. 3.38b, reveal an average axial vibration peak of 12g and an impact frequency of 13Hz. Thus, an evaluation of the simulation results shows a good match on the impact frequency, as well as a good match on the average axial vibration peaks, when compared with the experimental data.

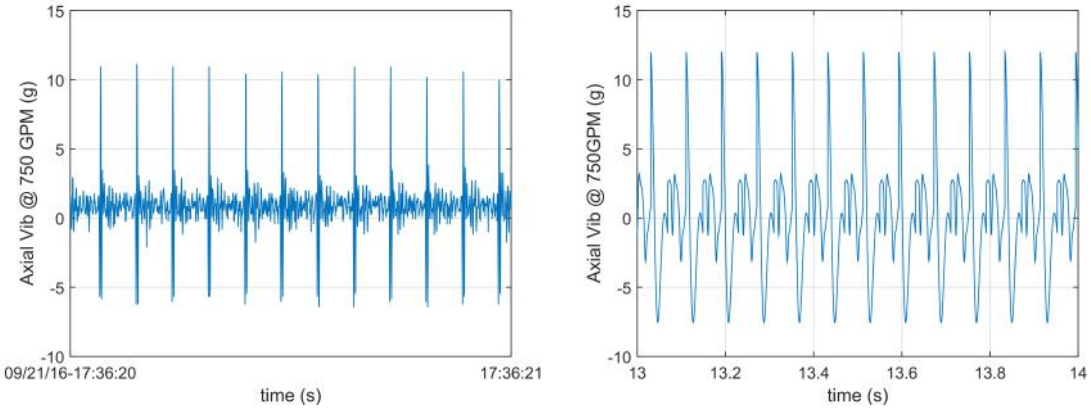

(a) (b)

Figure 3.38: Axial vibration field data (a) and simulations results (b), representing the sensor data located at x_1 (bit assembly), in a constant 750GPM mud flow rate scenario and 8klbf of weight-on-bit, during the 9.5in prototype test.

11th Event - axial vibration results at 770GPM (12.3Hz)

An analysis of the sensor data located at x_1 (bit assembly), given in Fig. 3.39a, reveals an average axial vibration peak of 12g and an impact frequency of 12Hz.

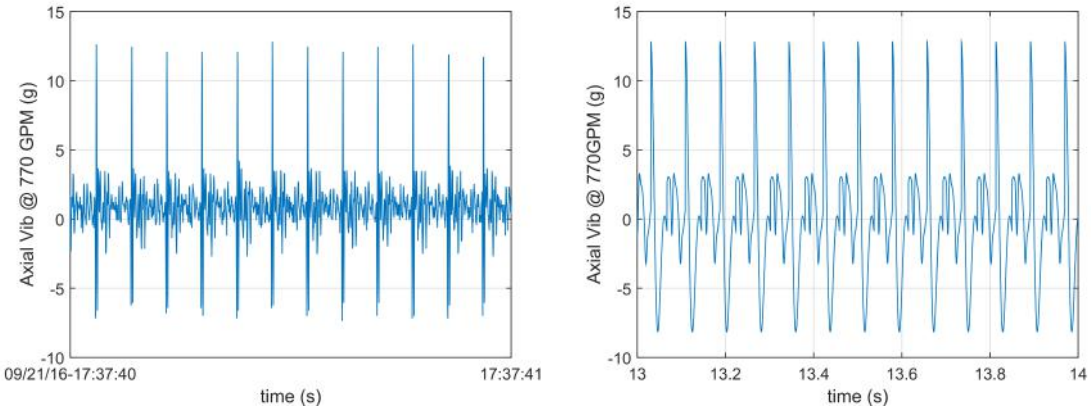

(a) (b)

Figure 3.39: Axial vibration field data (a) and simulations results (b), representing the sensor data located at x_1 (bit assembly), in a constant 770GPM mud flow rate scenario during the 9.5in tool test.

The simulation results, represented in Fig. 3.39b, reveal an average axial vibration peak of 13g, an impact frequency of 13Hz. Thus, an evaluation of the simulation results shows a good match on the impact frequency and on the average axial vibration peaks when compared with the experimental data.

12th Event - axial vibration results at 790GPM (12.6Hz)

An analysis of the sensor data located at x_1 (bit assembly), given in Fig. 3.40a, reveals an average axial vibration peak of 13g and an impact frequency of 13Hz.

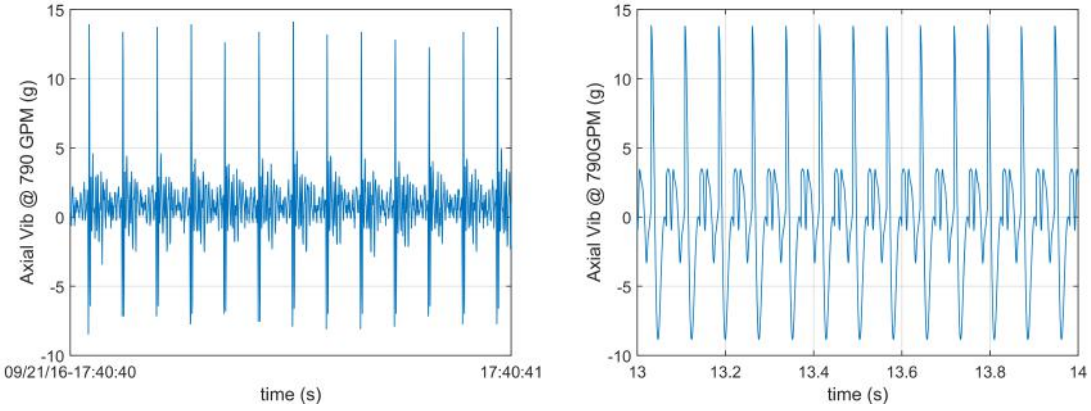

(a) (b)

Figure 3.40: Axial vibration field data (a) and simulations results (b), representing the sensor data located at x_1 (bit assembly), in a constant 790GPM mud flow rate scenario and 8klbf of weight-on-bit, during the 9.5in prototype test.

The simulation results, represented in Fig. 3.40b, reveal an average axial vibration peak of 14g and an impact frequency of 13Hz. Thus, an evaluation of the simulation results shows a good match on the impact frequency, as well as a good match on the average axial vibration peaks, when compared with the experimental data.

Event summary - axial vibration peaks

A summary of the axial vibrations peaks in relation to the mud flow twelve events recorded at both sensors (x_1 and x_5) is represented in Fig. 3.41a. The results from the axial vibration data measured at x_1 (bit assembly) seem to indicate a relation between the axial vibration peak levels as a function of the mud flow rate. The simulation results, represented in Fig. 3.41b, show a good overall match in the average axial vibration peaks when compared with the data measured at both locations (x_1 and x_5) in the field test. The mathematical model is also able to recreate the axial vibration peak levels as a function of the mud flow. The axial vibration data of the for both measurement devices are partially in accordance to

the field test data, as the simulation results show a good match in the axial vibration peaks and a poor match in axial vibration peak dispersion. Moreover, the axial vibration peaks dispersion seem to be independent of the mud flow rate, as well as sensor location. Similar to the previous tests, an analysis of the test data also revealed that, during the drilling operation, severe lateral vibrations were observed, and, such severe vibrations, could affect the axial vibration measurements.

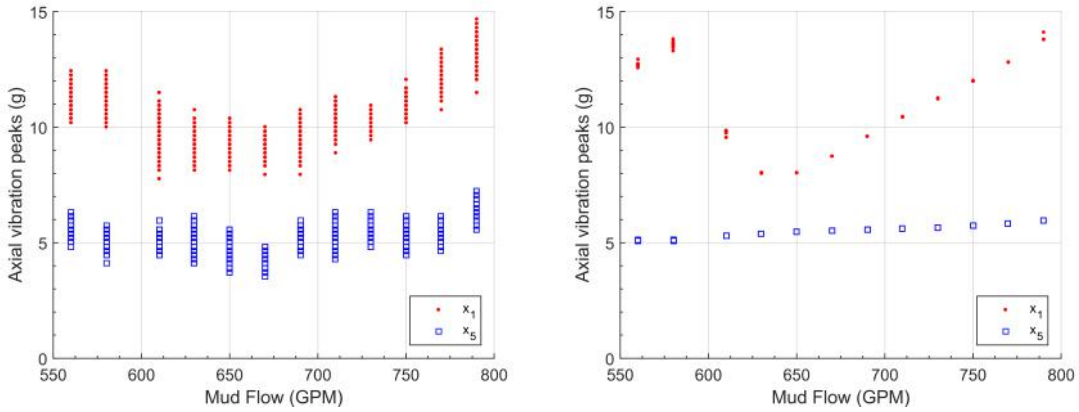

(a) (b)

Figure 3.41: Axial vibration field data (a) and simulations results (b) of the sensor located at x_1 (red dots) and the sensor located at x_5 (blue squares) obtained in a mud flow sweep scenario from 560 to 790GPM for the 9.5in tool test.

In contrast to the results obtained from the 7in tool, the field data and experimental results of the 9.5in tool show an strict periodic behavior with one relevant impacts per cycle. One factor that might have contributed for this result is the low excitation frequency range of the 9.5in tool, as the the intermittent behavior in the 7in tool results is observed around 30Hz. Although the mud flow rate range in the current test (560 to 790GPM) is higher than the mud flow sweep performed in the 7in tool tests (200 to 600GPM), the actual excitation frequency range is lower when compared with the axial acceleration field data and numerical results of the 7in tool. Thus, the resulting excitation frequency range for the 9.5in test is below 15Hz, which is significantly lower than both 7in tools tests.

3.3.4 Summary

After analyzing the data from the 16 events that were considered in the validation process of the 7in tool model and the 12 events that comprised the validation process of the 9.5in tool model, both models are considered validated in the operational conditions that were presented in the selected events. The main highlights of the models include:

- Overall good match of axial accelerations amplitudes at the bit assembly (x_1).

- Overall good match of impact frequencies.
- Overall satisfactory match of dynamical behavior.
- Model can reproduce the change in dynamic behavior observed in the field tests.

The validation process also revealed limitations of the mathematical model, as described by the lowlights below:

- Poor match of axial accelerations at bit assembly (x_1) during high flow rate.
  - Higher influence of system hydraulics – not included in the model.
- Not possible to match axial accelerations at the measurement sub above PDM (x_5).
  - Axial-lateral coupling not considered.

Additionally, the results from the mathematical model of 7in tool revealed that there is a relation between the dynamic behavior of the model and the the axial vibration peaks dispersion, as shown in Fig. 3.42.

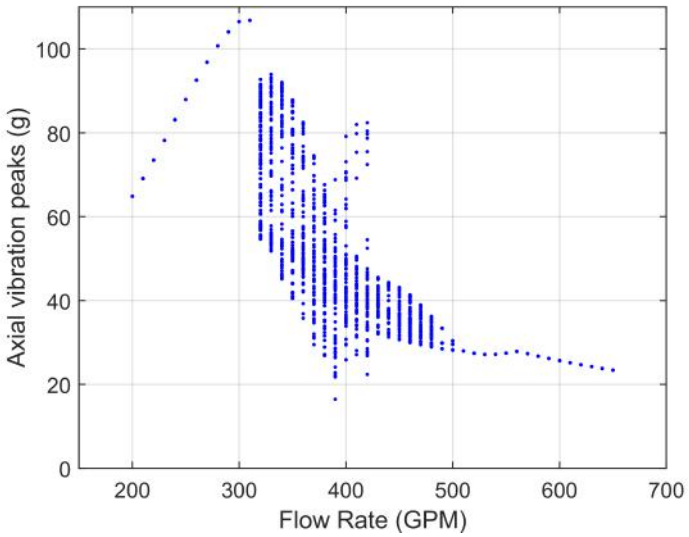

Figure 3.42: Simulation results of the axial vibration peaks at the bit assembly (x_1) obtained from a flow sweep analysis with 200- to 650-GPM mud flow rate in 10GPM increments (21.3 to 69.3Hz in 1.1Hz increments).

In summary, if a system exhibits a periodic behavior, there would be no dispersion in the axial vibration peaks. By contrast, if the system exhibits an aperiodic behavior, there would be a high dispersion of the axial vibration peaks.

Although the mathematical model shows promising results, there is a need for a deeper understanding of the main physical phenomena that influence the dynamical response of the tool. This topic is the focus of the next chapter.

Chapter 4

Analysis of the dynamic behavior of the mathematical model

In this chapter, an investigation is performed to better understand how the change in excitation frequency affect the dynamic behavior of the model. This chapter focuses on the analysis of the mathematical model of 7in tool to understand the physics behind the model. The results presented in section 4.1 explores the influence of each impact force in the dynamic behavior of the system. Next, section 4.2 focuses on the classification of the dynamic behaviors of the tool based on the results presented in the analysis of the impact forces. Finally, section 4.3 introduces a performance parameter, named impulse per second (J^*), that is proposed to evaluate and compare the tool's performance as the excitation frequency varies.

4.1 Analysis of the impact forces of the mathematical model

This analysis focuses on evaluating the relation between the dynamic behavior of the model and the impact forces as the excitation frequency is varied. This analysis considers the same excitation frequency range evaluated in the model validation: 200-650 GPM mud flow rate (21.3 to 69.3Hz). For each analysis, the methodology is as follows:

1. Simulate the mathematical model for a given excitation frequency, considering 200 impact cycles after the response achieves steady-state behavior.

2. Capture the outputs:

    - Impact forces for each impact surface (see Fig. 4.1)
    - Relative displacement between the anvil (x_2) and the impact surfaces.

- Acceleration of the bit assembly ($\ddot{x}_1$)

3. Plot the results in snapshots of 5 consecutive impact cycles to visualize the impact pattern for each impact force.

4. Extract the impact pattern for each impact surface

   - Regular impacts
   - Intermittent impacts
   - No impacts

5. Summarize the results into a flowchart, which shows the sequence of events that occurs in the analyzed time window.

6. Investigate the root cause of the impact pattern by analyzing the relative displacement between the anvil and the impact surfaces #1 and #2 (see Fig. 4.1).

7. Relate all these results with the acceleration of the bit assembly ($\ddot{x}_1$)

The proposed mathematical model allows four possible impacts, as shown in Fig. 4.1, impact #1, impact #2, impact #3, and impact #4. For each impact surface, three impact patterns are considered; i.e., regular impacts, intermittent impacts, and no impacts. If the analysis of the impact forces shows an impact pattern with regular time intervals, the impact pattern is considered regular; otherwise, the impact pattern is considered intermittent.

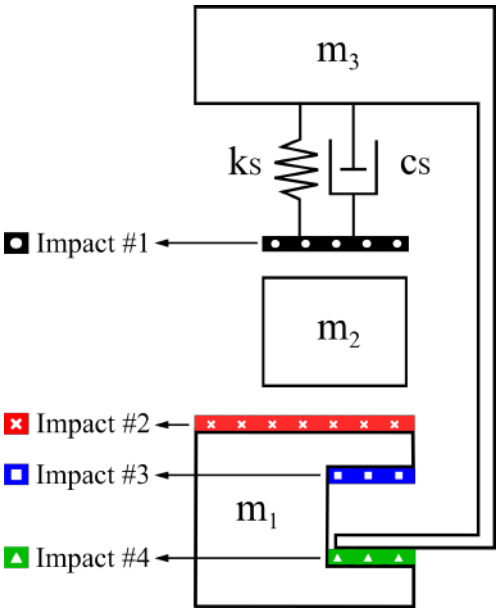

Figure 4.1: Sketch of the tool model representing the impact surfaces.

The impact surface #1 represents the contact surface between the recoil spring and the impacting anvil (m_2). In the description of the mathematical model (see section 2.2), this force was referred to as recoil spring force ($F_S(x_2, \dot{x_2}, x_3, \dot{x_3})$). To simplify the visualization of the impact pattern, this impact force will be referred as $F_{\#1}$.

The impact surface #2 represents the contact surface between the impacting anvil (m_2) and the bit assembly (m_1). In the description of the mathematical model, this force was referred to as impact face force ($F_I(x_1, \dot{x_1}, x_2, \dot{x_2})$). To simplify the visualization of the impact pattern, this impact force will be referred as $F_{\#2}$.

The impact surface #3 represents the contact surface between the tool housing (m_3) and the bit assembly (m_1). In the description of the mathematical model, this force was referred to as off-bottom shoulder force ($F_{Off}(x_1, \dot{x_1}, x_3, \dot{x_3})$). To simplify the visualization of the impact pattern, this impact force will be referred as $F_{\#3}$.

The impact surface #4 represents the contact surface between the tool housing (m_3) and the bit assembly (m_1). In the description of the mathematical model, this force was referred to as on-bottom shoulder force ($F_{On}(x_1, \dot{x_1}, x_3, \dot{x_3})$). To simplify the visualization of the impact pattern, this impact force will be referred as $F_{\#4}$.

The results are presented in snapshots of five consecutive impact cycles, which are used to visualize the overall impact pattern. The color scheme used to describe the forces in this analysis is the same as represented in the tool's sketch that indicates the impact surfaces (see Fig. 4.1).

For the current model design, during one full flow sweep procedure (mud flow ranging from 200 to 650 GPM), five different scenarios are observed from the simulation results. Each impact scenario shows a unique impact pattern.

- 1st scenario: excitation frequency from 21.3 to 33.1 Hz (200 to 310 GPM)
- 2nd scenario: excitation frequency from 34.1 to 35.2 Hz (320 to 330 GPM)
- 3rd scenario: excitation frequency from 36.3 to 44.8 Hz (340 to 420 GPM)
- 4th scenario: excitation frequency from 45.9 to 53.3 Hz (430 to 500 GPM)
- 5th scenario: excitation frequency from 54.4 to 69.3 Hz (510 to 650 GPM)

Even though the impact forces provide valuable information about the impact pattern, this analysis by itself does not provide enough information to fully describe the dynamic behavior of the model. Thus, the root causes of the impact pattern are investigated by analyzing the relative displacement between the anvil and the impact surfaces, as shown in Fig. 4.4. This analysis enables the investigation of the impact interaction from a different perspective by analyzing the relative position between the colliding bodies.

In this analysis, an impact interaction is represented by an intersection between the lines that represent the relative displacement between the colliding bodies, as represented by the points A, B, C, and D in Fig. 4.4. The point A represents the initial point of contact between the anvil (m_2) and the bit assembly (m_1) at the impact surface #2. The point B represents the loss of contact between the colliding bodies, hence the end of the impact interaction. Thus, the time window between points A and B is the length of the impact interaction. The same representation is applied to points C and D. Finally, these results are compared with the acceleration results to give a better understanding on the dynamic behavior of the model.

4.1.1 1st scenario: analysis of the impact forces between 21.3 and 33.1 Hz (200 - 310 GPM)

The first scenario considers the impact forces at 200-GPM mud flow rate (21.3 Hz), as shown in Fig. 4.2. The simulations results show that the impact forces $F_{\#1}$ and $F_{\#2}$ exhibit a consistent impact pattern with regular time. This result is in accordance with the conclusions presented in the model validation, which showed that the acceleration results at 200-GPM mud flow rate (21.3 Hz) indicated a periodic behavior (see Fig. 3.8b).

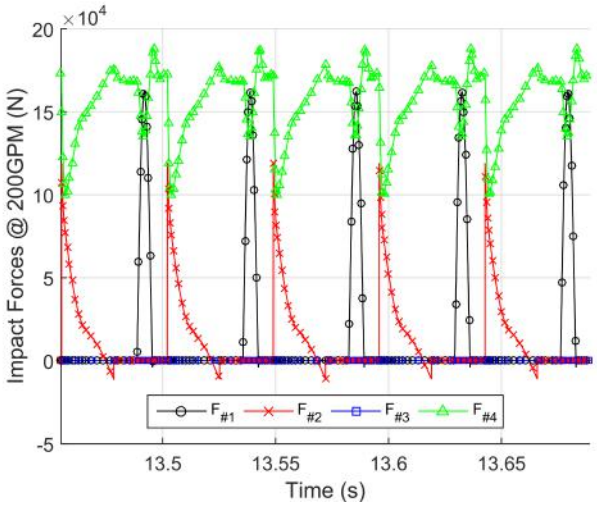

Figure 4.2: Simulation results of impact forces for five impact cycles for the 7in tool model evaluated at an excitation frequency of 21.3 Hz (200GPM mud flow rate).

In relation to $F_{\#4}$, the results shown in Fig. 4.2 can be related to the initial conditions considered in the model implementation. The initial conditions consider that the model is in the on-bottom configuration (WOB > 0), since the tool is in contact with the rock formation at the bottom of the well at the impact surface #4 (see Fig. 2.4). Since the WOB is applied at impact surface #4, $F_{\#4}$ can be seen

as WOB fluctuations that are caused by the high impact forces observed at both surfaces #1 and #2.

By definition, if the impact force is always greater than zero, this indicates that the bodies are in always in contact; hence, no impact is detected. Following this definition, the oscillation on $F_{\#4}$ are not acknowledged as impact. There is no loss of contact between the bit assembly (m_1) and the tool housing (m_3) at the impact surface #4, as $F_{\#4}$ is always greater than zero. In practical terms, this means that even though this interaction is modeled as an impact force, this force works as a contact force.

The sequence of events for this scenario can be summarized in the following steps, as represented by the flowchart shown in Fig. 4.3. First, the anvil (m_2) impacts the bit assembly (m_1) at surface #2, which is immediately followed by oscillations at $F_{\#4}$. Next, the anvil impacts (m_2) the tool housing (m_3) at surface #1, which is again followed by oscillations in $F_{\#4}$. No impact are detected at surface #3 ($F_{\#3} = 0$). This impact pattern is repeated for the following five cycles.

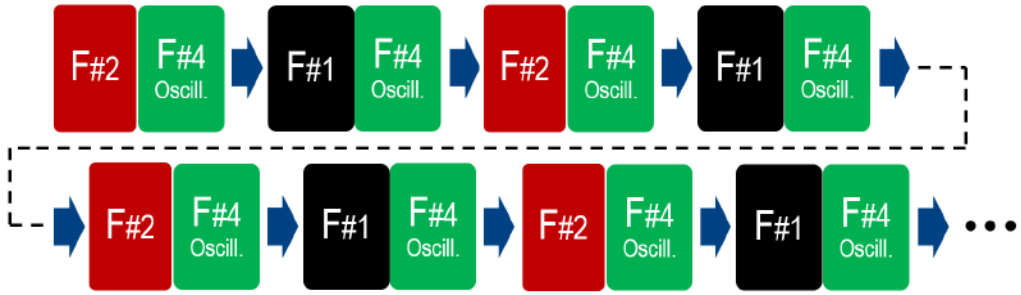

Figure 4.3: Flowchart that represents the sequence of events for five impact cycles at 200GPM (21.3 Hz).

In regards to the impact pattern, the results from Figs. 4.2 and 4.3 show that there are regular impacts at surfaces #1 and #2. In addition, no impacts were observed at surfaces #3 and #4.

Further investigation regarding the dynamic behavior of the model is performed by analyzing the relative position between the anvil and the impact surfaces #1 and #2, as shown in Fig. 4.4.

The simulations results show that there are 2 intersections between the anvil (x_2) and the impact surface #2 (points A and B) and 2 intersections between the anvil (x_2) and the impact surface #1 (points C and D) for every impact cycle. These results can be simplified by the following sequence of events:

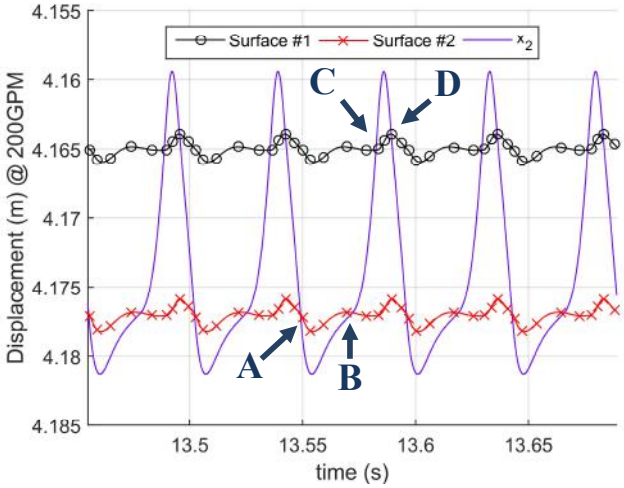

Figure 4.4: Simulation results of the relative position between the anvil and the impact surfaces #1 and #2 for five impact cycles for the 7in tool model evaluated at an excitation frequency of 21.3 Hz (200GPM mud flow rate).

1. Interval $A \rightarrow B$: Impact occurs at the impact surface #2.
   - Point A: Anvil (m_2) makes contact with the bit assembly (m_1) at the impact surface #2.
   - Point B: Anvil (m_2) loses contact with the bit assembly (m_1) at the impact surface #2.
2. Interval $B \rightarrow C$: Anvil travels towards the impact surface #1.
3. Interval $C \rightarrow D$: Impact occurs at the impact surface #1.
   - Point C: Anvil (m_2) makes contact with the recoil spring (m_1) at the impact surface #1.
   - Point D: Anvil (m_2) loses contact with the bit assembly (m_1) at the impact surface #1.
4. Interval $D \rightarrow A$: Anvil travels towards the impact surface #2.

The next step is to superimpose the points of interest obtained from the analysis of the relative position between the anvil and the impact surfaces #1 and #2 on the results of impact forces, as shown in Fig. 4.5.

The results show that the moment the anvil makes contact with the bit assembly (Point A) coincides with the maximum value of $F_{\#2}$. Additionally, the results show that the loss of contact in between the colliding bodies results in hysteresis in the impact forces, as observed in points B and D. Although this hysteresis is undesirable, this effect was already expected in the current results, since it is related to limitations regarding the spring-dashpot impact model (see section 1.3.2).

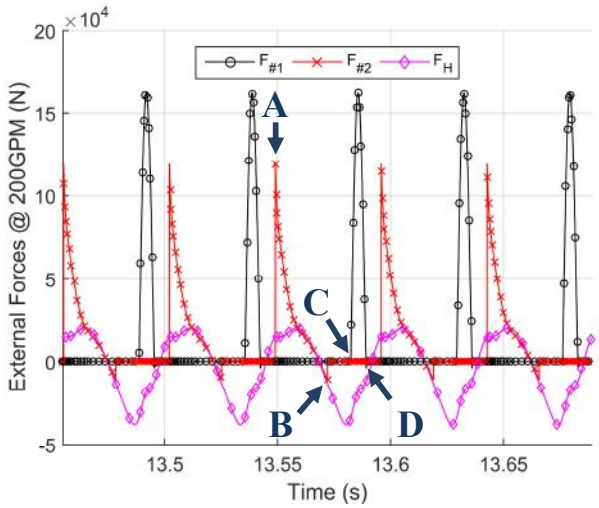

Figure 4.5: Simulation results of the excitation force and the impact forces at surfaces #1 and #2 for five impact cycles for the 7in tool model evaluated at an excitation frequency of 21.3 Hz (200GPM mud flow rate).

Finally, to understand how the impact dynamics affects the axial vibration results, the results shown in Fig. 4.4 and Fig. 4.5 are compared with the axial acceleration results for the same time window, as shown in Fig. 4.6.

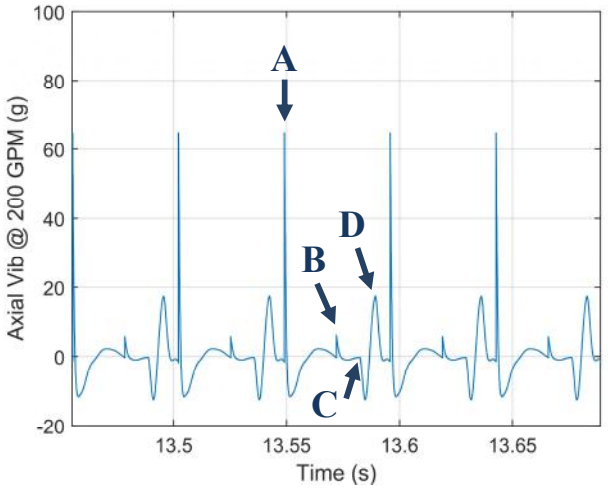

Figure 4.6: Simulation results of axial acceleration at x_1 for five impact cycles for the 7in tool model evaluated at an excitation frequency of 21.3 Hz (200GPM mud flow rate).

The simulations results presented in Fig. 4.6 seems to indicate a periodic behavior, which is consistent with the results presented in the previous chapter (see Fig. 3.8b). Furthermore, the results show that the point A coincides with the highest axial vibration peak in each cycle. This in accordance with the assumption proposed in the model validation (see section 3.3), in which assumed that the highest

axial vibration peak coincides with the impact of the anvil (m_2) at the bit assembly (m_1) at the impact face (surface #2).

Additionally, the second axial vibration peak, represented by the point B in Fig. 4.6, is related to the hysteresis of the impact force $F_{\#2}$. Similarly, the small oscillation observed at the point D is related to the hysteresis of the impact force $F_{\#1}$. This hysteresis effect is related to the contact force history of the spring-dashpot model. For further information see Fig. 1.11 at section 1.3.2.

Even though these secondary axial vibration peaks (points B and D) are related to a limitation of the spring-dashpot model, the model is able to represent the real system. For the purposes of this work, this physical inconsistency is seen a limitation, but it does not undermines the current results, as this model is the first attempt to model the dynamic behavior of the tool. With additional data available for the model, the impact model used could be revisited and improved.

4.1.2 2nd scenario: analysis of the impact forces between 34.1 and 35.2 Hz (320 - 330 GPM)

The second scenario considers the impact forces at 320-GPM mud flow rate (34.1 Hz), as shown in Fig. 4.7. The simulations results show that the impact force $F_{\#2}$ shows a consistent impact pattern with regular time interval, however $F_{\#2}$ exhibit an inconsistent impact pattern. Thus, the simulations results seem to indicate an aperiodic behavior because no consistent pattern is observed through the analyzed cycles. Additionally, these intermittent impacts at the surface #1 appear to be related to the increase in axial vibration peak dispersion observed at 320 GPM in Fig. 3.42.

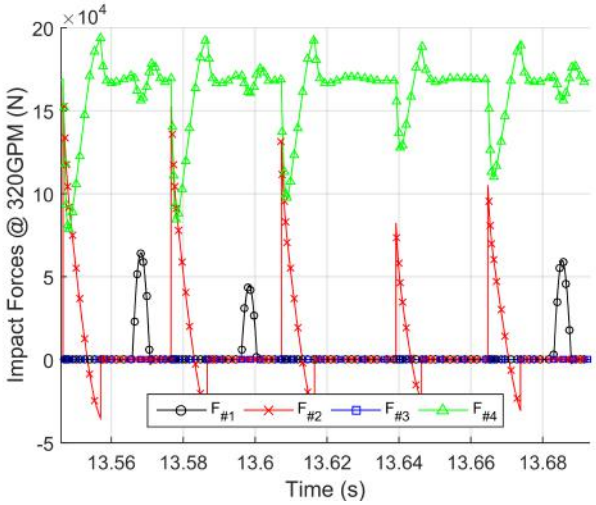

Figure 4.7: Simulation results of impact forces for five impact cycles for the 7in tool model evaluated at an excitation frequency of 34.1 Hz (320GPM mud flow rate).

The sequence of events for this scenario can be summarized in the following steps, as represented by the flowchart shown in Fig. 4.8. For the first two cycles, the anvil (m_2) impacts the bit assembly (m_1) at surface #2, which is immediately followed by oscillations at $F_{\#4}$. Next, the anvil impacts (m_2) the tool housing (m_3) at surface #1, which is again followed by oscillations in $F_{\#4}$. No impact are detected at surface #3 ($F_{\#3} = 0$). However, this impact pattern is not consistent throughout for the following five cycles, as there are some cycles that no impact are detected at impact surface #1. Thus, the results from Figs. 4.7 and 4.8 show that there are regular impacts at surface #2 and intermittent impacts at surface #1. Furthermore, no impacts are observed at surfaces #3 and #4.

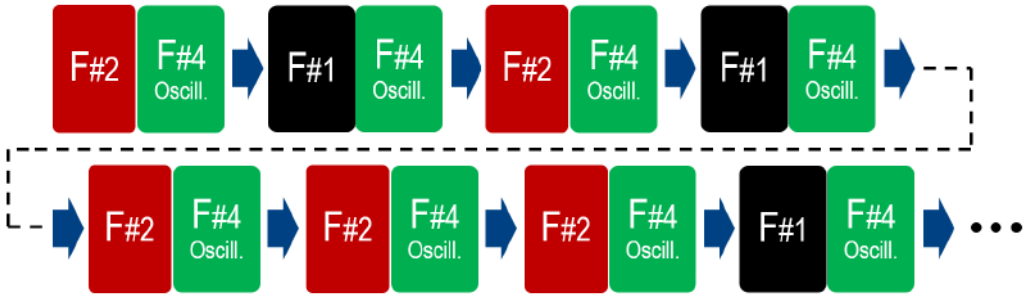

Figure 4.8: Flowchart that represents the sequence of events for five impact cycles at 320GPM (34.1 Hz).

Further investigation regarding the dynamic behavior of the model is performed by analyzing the relative position between the anvil and the impact surfaces #1 and #2, as shown in Fig. 4.9.

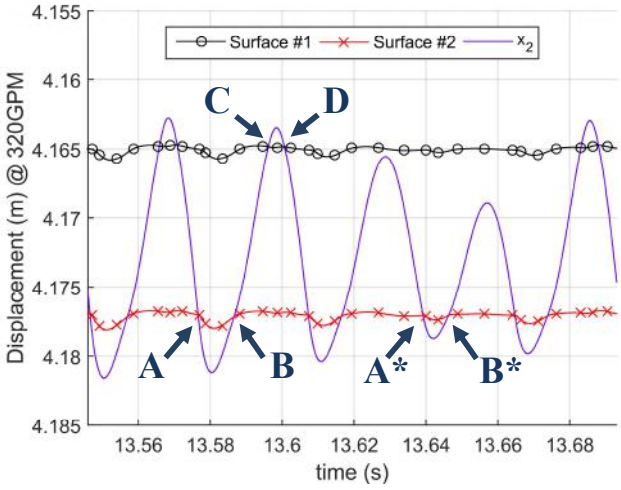

Figure 4.9: Simulation results of the relative position between the anvil and the impact surfaces #1 and #2 for five impact cycles for the 7in tool model evaluated at an excitation frequency of 34.1 Hz (320GPM mud flow rate).

The results show that there are two possibilities for the relationship between the

trajectory of the anvil (x_2) and the impact surfaces #1 and #2. For some cycles, the simulations results show that there are 2 intersections between the anvil (x_2) and the impact surface #2 (points A and B) and 2 intersections between the anvil (x_2) and the impact surface #1 (points C and D) for every impact cycle. These results can be simplified by the following sequence of events:

1. Interval $A \rightarrow B$: Impact occurs at the impact surface #2.
2. Interval $B \rightarrow C$: Anvil travels towards the impact surface #1.
3. Interval $C \rightarrow D$: Impact occurs at the impact surface #1.
4. Interval $D \rightarrow A$: Anvil travels towards the impact surface #2.

However, the simulations results show that there are cycles with 2 intersections between the anvil (x_2) and the impact surface #2 (points A* and B*) and no intersections between the anvil (x_2) and the impact surface #1. These results can be simplified by the following sequence of events:

1. Interval $A* \rightarrow B*$: Impact occurs at the impact surface #2.
    - Point A*: Anvil (m_2) makes contact with the bit assembly (m_1) at the impact surface #2.
    - Point B*: Anvil (m_2) loses contact with the bit assembly (m_1) at the impact surface #2.
2. Interval $B* \rightarrow A*$: Anvil travels towards the the impact surface #1. However, the anvil changes its direction before reaching the impact surface #1. Next, anvil is pushed towards the impact surface #2.

The next step is to superimpose the points of interest obtained from the analysis of the relative position between the anvil and the impact surfaces #1 and #2 on the results of impact forces, as shown in Fig. 4.10. For each cycle, the results show that the maximum values of $F_{\#2}$ coincide with the moment the anvil makes contact with the bit assembly (points A or A*). Additionally, the results show that the loss of contact in between the colliding bodies results in hysteresis in the impact forces, as observed in points B, B*, and D. In contrast to point A, the point C is not related to the point of maximum amplitude of $F_{\#1}$.

This analysis reveals that the dispersion in the values of $F_{\#2}$ are related to the presence of impact at the recoil spring (surface #1). The presence of intermittent impact at surface #1 means that different levels of energy will be store at the recoil spring. This translates into a greater variation in the maximum values of $F_{\#2}$

possible for each cycle. This is in accordance to the idea that that the recoil spring functions as a energy-storage mechanism.

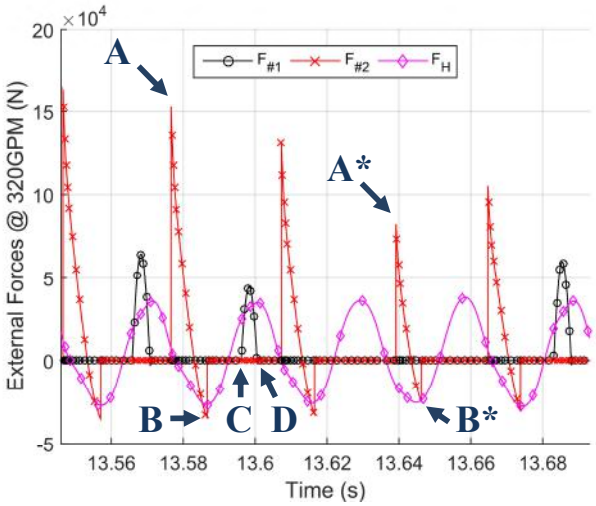

Figure 4.10: Simulation results of the excitation force and the impact forces at surfaces #1 and #2 for five impact cycles for the 7in tool model evaluated at an excitation frequency of 34.1 Hz (320GPM mud flow rate).

Furthermore, the results show that there seems to be a direct relation between maximum values of $F_{\#2}$ and the maximum axial vibration peak. An increase in the dispersion in the values of $F_{\#2}$ results in an increase in the axial vibration peaks dispersion, which is consistent with the results presented at Fig 3.42.

Finally, to understand how the impact dynamics affects the axial vibration results, the results shown in Fig. 4.9 and Fig. 4.10 are compared with the axial acceleration results for the same time window, as shown in Fig. 4.11.

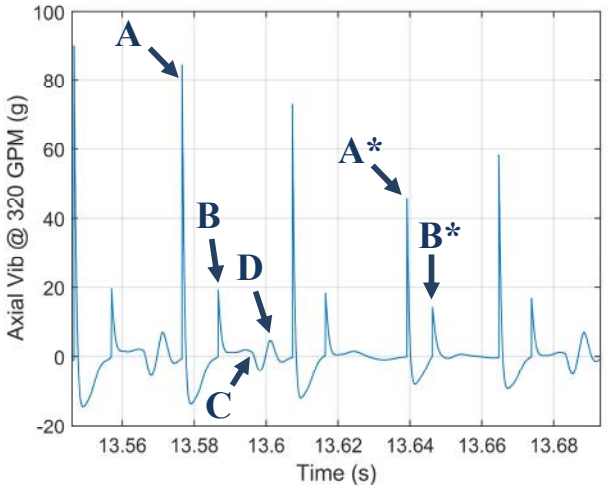

Figure 4.11: Simulation results of axial acceleration at x_1 for five impact cycles for the 7in tool model evaluated at an excitation frequency of 34.1 Hz (320GPM mud flow rate).

The simulations results presented in Fig. 4.11 seems to indicate an aperiodic behavior. Furthermore, the results reinforces that the variation in the axial vibration peaks (points A or A*) can be related to the dispersion in the maximum values of $F_{\#2}$. Additionally, the results show that the oscillations in acceleration observed at the interval $C \rightarrow D$ are related to the impact at surface #1 (recoil spring), since no fluctuations in the axial vibration are observed after $A* \rightarrow B*$.

4.1.3 3rd scenario: analysis of the impact forces between 36.3 and 44.8 Hz (340 - 420 GPM)

The third scenario considers the impact forces at 350-GPM mud flow rate (37.3 Hz), as shown in Fig. 4.12. The simulations results show that the impact forces $F_{\#2}$ and $F_{\#2}$ exhibit an inconsistent impact pattern. Thus, the simulations results seem to indicate an aperiodic behavior because no consistent pattern is observed through the analyzed cycles. Additionally, these intermittent impacts at both surfaces #1 and #2 also appear to be related to the axial vibration peak dispersion observed at 350 GPM in Fig. 3.42.

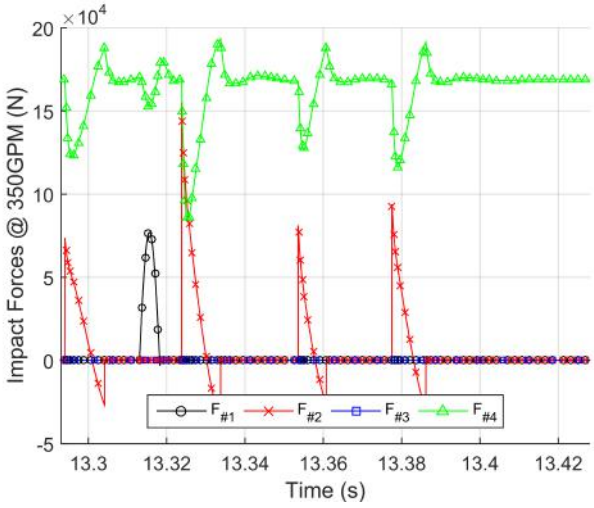

Figure 4.12: Simulation results of impact forces for five impact cycles for the 7in tool model evaluated at an excitation frequency of 37.3 Hz (350GPM mud flow rate).

The sequence of events for this scenario can be summarized in the following steps, as represented by the flowchart shown in Fig. 4.13. For the first cycle, the anvil (m_2) impacts the bit assembly (m_1) at surface #2, which is immediately followed by oscillations at $F_{\#4}$. Next, the anvil impacts (m_2) the tool housing (m_3) at surface #1, which is again followed by oscillations in $F_{\#4}$. No impact are detected at surface #3 ($F_{\#3} = 0$). However, this impact pattern is not consistent throughout for the following five cycles, as there are some cycles that no impact are detected at impact surfaces #1 and #2. Thus, the results from Figs. 4.12 and 4.13 show that there

are and intermittent impacts at surfaces #1 and #2. Furthermore, no impacts are observed at surfaces #3 and #4.

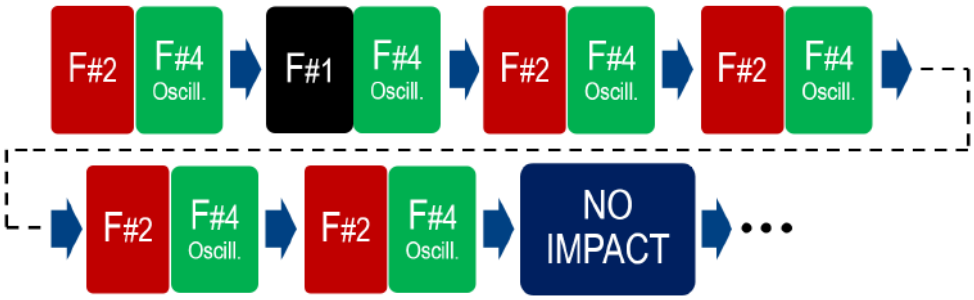

Figure 4.13: Flowchart that represents the sequence of events for five impact cycles at 350GPM (37.3 Hz).

Further investigation regarding the dynamic behavior of the model is performed by analyzing the relative position between the anvil and the impact surfaces #1 and #2, as shown in Fig. 4.14.

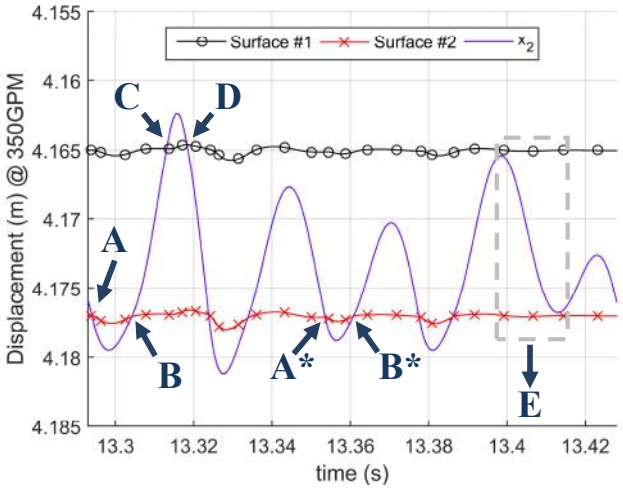

Figure 4.14: Simulation results of the relative position between the anvil and the impact surfaces #1 and #2 for five impact cycles for the 7in tool model evaluated at an excitation frequency of 37.3 Hz (350GPM mud flow rate).

The results seem show that there are three possibilities for the relationship between the trajectory of the anvil (x_2) and the impact surfaces #1 and #2. For the first cycle, the simulations results show that there are 2 intersections between the anvil (x_2) and the impact surface #2 (points A and B) and 2 intersections between the anvil (x_2) and the impact surface #1 (points C and D) for every impact cycle. These results can be simplified by the following sequence of events:

1. Interval $A \rightarrow B$: Impact occurs at the impact surface #2.

2. Interval $B \rightarrow C$: Anvil travels towards the impact surface #1.

3. Interval $C \rightarrow D$: Impact occurs at the impact surface #1.

4. Interval $D \rightarrow A$: Anvil travels towards the impact surface #2.

Additionally, the simulations results show that there are cycles with 2 intersections between the anvil (x_2) and the impact surface #2 (points A* and B*) and no intersections between the anvil (x_2) and the impact surface #1. These results can be simplified by the following sequence of events:

1. Interval $A* \rightarrow B*$: Impact occurs at the impact surface #2.

2. Interval $B* \rightarrow A*$: Anvil travels towards the the impact surface #1. However, the anvil changes its direction before reaching the impact surface #1. Next, anvil is pushed towards the impact surface #2.

Finally, the simulations results show that there are cycles with no intersections between the anvil (x_2) and the impact surfaces #1 and #2 (points E). These results can be simplified by the following sequence of events:

1. Interval $A* \rightarrow B*$: Impact occurs at the impact surface #2.

    - Point A*: Anvil (m_2) makes contact with the bit assembly (m_1) at the impact surface #2.
    - Point B*: Anvil (m_2) loses contact with the bit assembly (m_1) at the impact surface #2.

2. Interval $B* \rightarrow E$: Anvil travels towards the the impact surface #1. However, the anvil changes its direction before reaching the impact surface #1. Next, anvil is pushed towards the impact surface #2. However, the anvil changes its direction before reaching the impact surface #2.

    - Point E: The anvil does not makes contact with both impact surfaces #1 and #2. Thus, there are no impacts in this cycle.

The next step is to superimpose the points of interest obtained from the analysis of the relative position between the anvil and the impact surfaces #1 and #2 on the results of impact forces, as shown in Fig. 4.15. For each cycle, the results show that the maximum values of $F_{\#2}$ coincide with the moment the anvil makes contact with the bit assembly (points A or A*). Additionally, the results show that the loss of contact in between the colliding bodies results in hysteresis in the impact forces, as observed in points B, B*, and D. In contrast to point A, the point C is not related to the point of maximum amplitude of $F_{\#1}$.

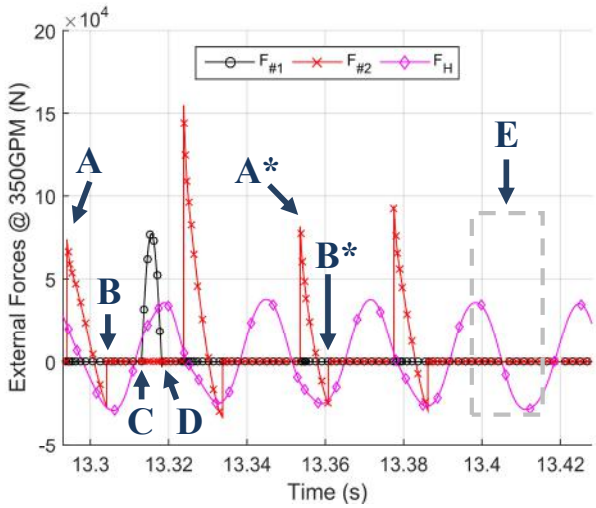

Figure 4.15: Simulation results of the excitation force and the impact forces at surfaces #1 and #2 for five impact cycles for the 7in tool model evaluated at an excitation frequency of 37.3 Hz (350GPM mud flow rate).

In accordance to the results obtained at the second scenario (see Fig. 4.10), this analysis also reveal that the dispersion in the values of $F_{\#2}$ are related to the presence of impact at the recoil spring (surface #1).Moreover, the results show that there are no impact at the point E, since there the anvil does not makes contact with both impact surfaces #1 and #2.

Finally, to understand how the impact dynamics affects the axial vibration results, the results shown in Fig. 4.14 and Fig. 4.15 are compared with the axial acceleration results for the same time window, as shown in Fig. 4.16.

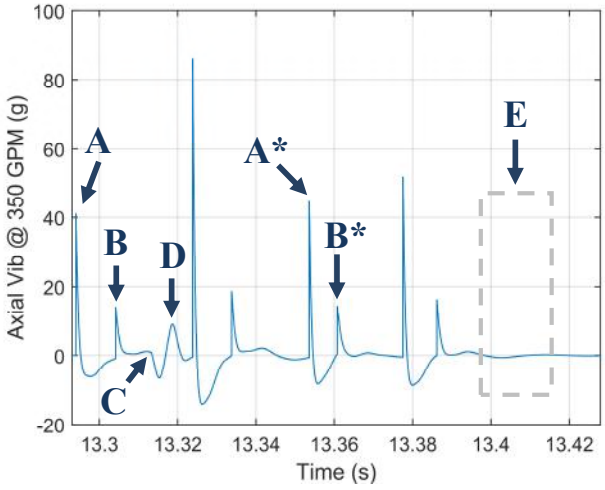

Figure 4.16: Simulation results of axial acceleration at x_1 for five impact cycles for the 7in tool model evaluated at an excitation frequency of 37.3 Hz (350GPM mud flow rate).

The simulations results presented in Fig. 4.16 seems to indicate an aperiodic

behavior. Furthermore, the results reinforces that the variation in the axial vibration peaks (points A or A*) can be related to the dispersion in the maximum values of $F_{\#2}$, which is consistent with the results presented at Fig 3.42. Additionally, the results show that the oscillations in acceleration observed at the interval $C \rightarrow D$ are related to the impact at surface #1 (recoil spring), since no fluctuations in the axial vibration are observed after $A* \rightarrow B*$. Moreover, the results show that there are no acceleration oscillation observed at the point E, since there are no impacts detected at both impact surfaces #1 and #2.

4.1.4 4th scenario: analysis of the impact forces between 45.9 and 53.3 Hz (430 - 500 GPM)

The fourth scenario considers the impact forces at 500-GPM mud flow rate (53.3 Hz), as shown in Fig. 4.17. The simulations results show that the impact forces $F_{\#2}$ exhibit an inconsistent impact pattern, however no impacts observed at the impact surface #1 ($F_{\#1} = 0$). Thus, the simulations results seem to indicate an aperiodic behavior because no consistent pattern is observed through the analyzed cycles.

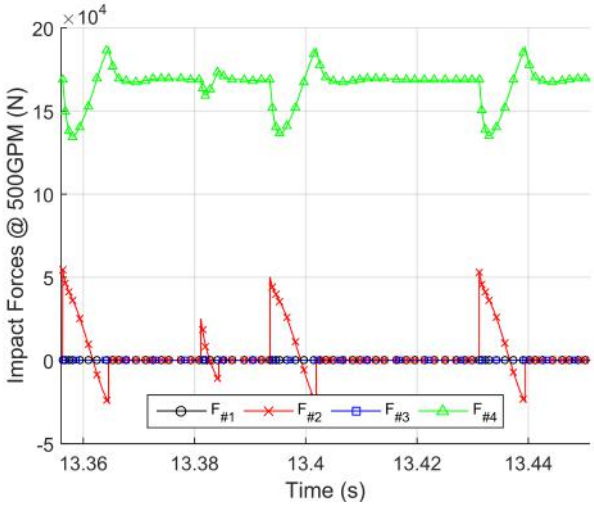

Figure 4.17: Simulation results of impact forces for five impact cycles for the 7in tool model evaluated at an excitation frequency of 53.3 Hz (500GPM mud flow rate).

Furthermore, the results show an approximately 60% reduction in the maximum amplitude of the impact force $F_{\#2}$ when compared with the results of the first scenario (see Fig. 4.2). According to the working principle of the tool, the recoil spring functions as a energy storage mechanism by converting the kinetic energy of the anvil into elastic potential energy for the next cycle movement. Thus, if there are no impact at the recoil spring (surface #1), no energy will be stored for the next cycle. Consequently, this results in severe reduction in the maximum amplitude of the impact force $F_{\#2}$. This phenomenon can also be related to the sudden reduction

in axial acceleration peaks observed at the transition from 420 to 430 GPM in Fig. 3.42. More information on this phenomenon is presented in sections 4.2 and 4.3.

The sequence of events for this scenario can be summarized in the following steps, as represented by the flowchart shown in Fig. 4.18. For the first three cycles, the anvil (m_2) impacts the bit assembly (m_1) at surface #2, which is immediately followed by oscillations at $F_{\#4}$. No impact are detected at surfaces #1 and #3 ($F_{\#1} = F_{\#3} = 0$). However, this impact pattern is not consistent throughout for the following five cycles, as there are some cycles that no impact are detected at impact surfaces #2. Thus, the results from Figs. 4.17 and 4.18 show that there are and intermittent impacts at surfaces #2 and no impacts are observed at surfaces #1, #3, and #4.

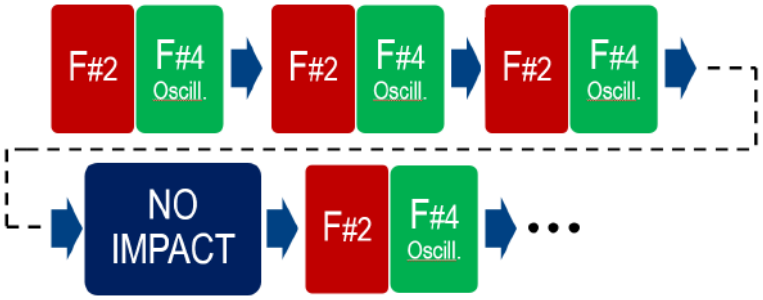

Figure 4.18: Flowchart that represents the sequence of events for five impact cycles at 500GPM (53.3 Hz).

Further investigation regarding the dynamic behavior of the model is performed by analyzing the relative position between the anvil and the impact surfaces #1 and #2, as shown in Fig. 4.19.

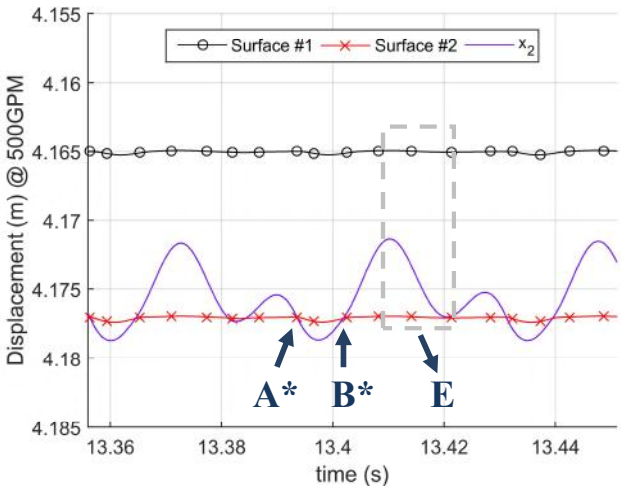

Figure 4.19: Simulation results of the relative position between the anvil and the impact surfaces #1 and #2 for five impact cycles for the 7in tool model evaluated at an excitation frequency of 53.3 Hz (500GPM mud flow rate).

The results show that there are two possibilities for the relationship between the trajectory of the anvil (x_2) and the impact surfaces #1 and #2. For some cycles, the simulations results show that there are cycles with 2 intersections between the anvil (x_2) and the impact surface #2 (points A* and B*) and no intersections between the anvil (x_2) and the impact surface #1. These results can be simplified by the following sequence of events:

1. Interval $A* \rightarrow B*$: Impact occurs at the impact surface #2.
2. Interval $B* \rightarrow A*$: Anvil travels towards the the impact surface #1. However, the anvil changes its direction before reaching the impact surface #1. Next, anvil is pushed towards the impact surface #2.

However, the simulations results also seems to indicate that there are cycles with no intersections between the anvil (x_2) and the impact surfaces #1 and #2 (points E). These results can be simplified by the following sequence of events:

1. Interval $A* \rightarrow B*$: Impact occurs at the impact surface #2.
2. Interval $B* \rightarrow E$: Anvil travels towards the the impact surface #1. However, the anvil changes its direction before reaching the impact surface #1. Next, anvil is pushed towards the impact surface #2. However, the anvil changes its direction before reaching the impact surface #2.

The next step is to superimpose the points of interest obtained from the analysis of the relative position between the anvil and the impact surfaces #1 and #2 on the results of impact forces, as shown in Fig. 4.20.

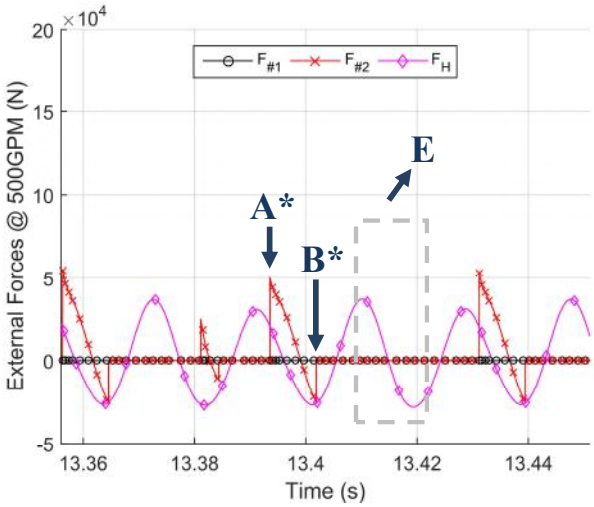

Figure 4.20: Simulation results of the excitation force and the impact forces at surfaces #1 and #2 for five impact cycles for the 7in tool model evaluated at an excitation frequency of 53.3 Hz (500GPM mud flow rate).

For each cycle, the results show that the maximum values of $F_{\#2}$ coincide with the moment the anvil makes contact with the bit assembly (points A*). Additionally, the results show that the loss of contact in between the colliding bodies results in hysteresis in the impact forces, as observed in points B*. Furthermore, the results show that there are no impact at the point E, since there the anvil does not makes contact with both impact surfaces #1 and #2.

Finally, to understand how the impact dynamics affects the axial vibration results, the results shown in Fig. 4.19 and Fig. 4.20 are compared with the axial acceleration results for the same time window, as shown in Fig. 4.21.

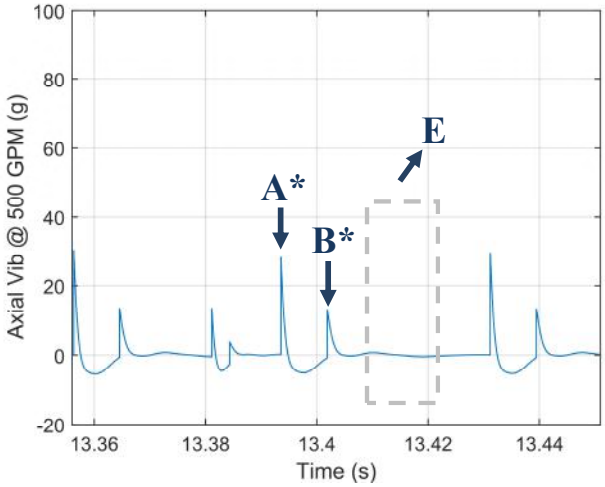

Figure 4.21: Simulation results of axial acceleration at x_1 for five impact cycles for the 7in tool model evaluated at an excitation frequency of 53.3 Hz (500GPM mud flow rate).

The simulations results presented in Fig. 4.21 seems to indicate an aperiodic behavior. Furthermore, the results reinforces that the variation in the axial vibration peaks (points A*) can be related to the dispersion in the maximum values of $F_{\#2}$, which is consistent with the results presented at Fig 3.42. Moreover, the results show that there are no acceleration oscillation observed at the point E, since there are no impacts detected at both impact surfaces #1 and #2.

4.1.5 5th scenario: analysis of the impact forces 54.4 and 69.3 Hz (510 - 650 GPM)

The fifth scenario considers the impact forces at 600-GPM mud flow rate (64.0 Hz), as shown in Fig. 4.22. The simulations results show that the impact force $F_{\#2}$ exhibit a consistent impact pattern with regular time, however no impacts observed at the impact surface #1 ($F_{\#1} = 0$). This result is in accordance with the conclusions

presented in the model validation, which showed that the acceleration results at 600-GPM mud flow rate (64.0 Hz) indicated a periodic behavior (see Fig. 3.18b).

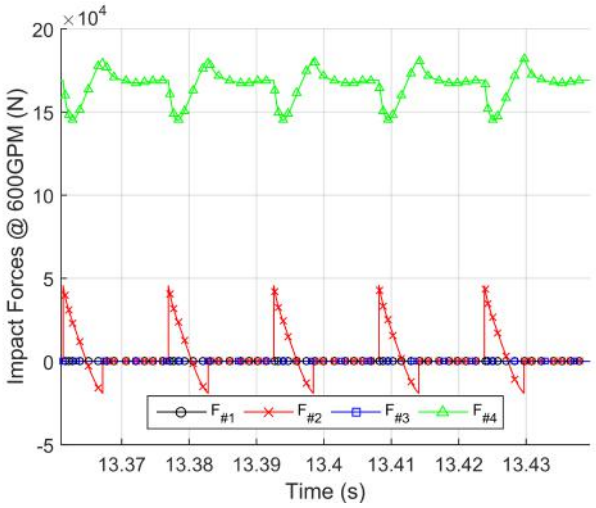

Figure 4.22: Simulation results of impact forces for five impact cycles for the 7in tool model evaluated at an excitation frequency of 64.0 Hz (600GPM mud flow rate).

Additionally, the results also show an approximately 60% reduction in the maximum amplitude of the impact force $F_{\#2}$ when compared with the results of the first scenario (see Fig. 4.2). This is in accordance to the assumption that if there are no impact at the recoil spring (surface #1), there will be a severe reduction in the maximum amplitude of the impact force $F_{\#2}$, as shown in Fig. 4.17.

The sequence of events for this scenario can be summarized in the following steps, as represented by the flowchart shown in Fig. 4.23. First, the the anvil (m_2) impacts the bit assembly (m_1) at surface #2, which is immediately followed by oscillations at $F_{\#4}$. No impact are detected at surfaces #1 and #3 ($F_{\#1} = F_{\#3} = 0$). This impact pattern is repeated for the following five cycles.

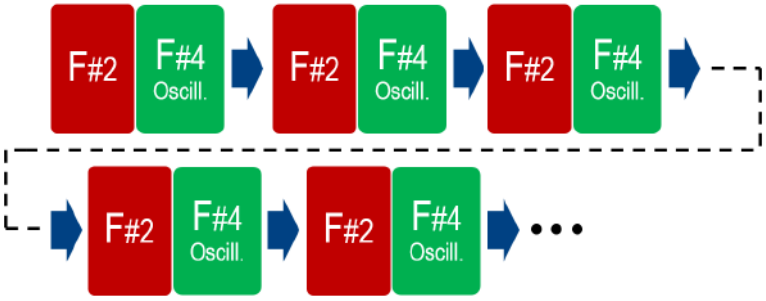

Figure 4.23: Flowchart that represents the sequence of events for five impact cycles at 600GPM (64.0 Hz).

In regards to the impact pattern, the results from Figs. 4.22 and 4.23 show that there are regular impacts at surface #2, and there are no impacts on the impact surfaces #1, #3, and #4.

Further investigation regarding the dynamic behavior of the model is performed by analyzing the relative position between the anvil and the impact surfaces #1 and #2, as shown in Fig. 4.24.

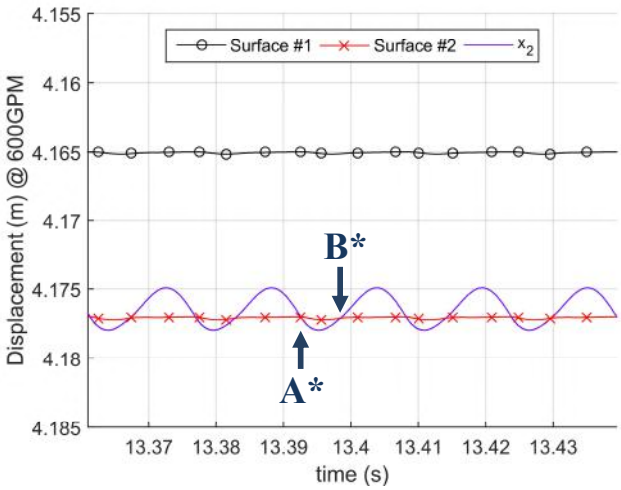

Figure 4.24: Simulation results of the relative position between the anvil and the impact surfaces #1 and #2 for five impact cycles for the 7in tool model evaluated at an excitation frequency of 64.0 Hz (600GPM mud flow rate).

The simulations results seems to indicate that there are cycles with 2 intersections between the anvil (x_2) and the impact surface #2 (points A* and B*) and no intersections between the anvil (x_2) and the impact surface #1. These results can be simplified by the following sequence of events:

1. Interval $A* \rightarrow B*$: Impact occurs at the impact surface #2.

2. Interval $B* \rightarrow A*$: Anvil travels towards the the impact surface #1. However, the anvil changes its direction before reaching the impact surface #1. Next, anvil is pushed towards the impact surface #2.

The next step is to superimpose the points of interest obtained from the analysis of the relative position between the anvil and the impact surfaces #1 and #2 on the results of impact forces, as shown in Fig. 4.25. For each cycle, the results show that the maximum values of $F_{\#2}$ coincide with the moment the anvil makes contact with the bit assembly (points A*). Additionally, the results show that the loss of contact in between the colliding bodies results in hysteresis in the impact forces, as observed in points B*.

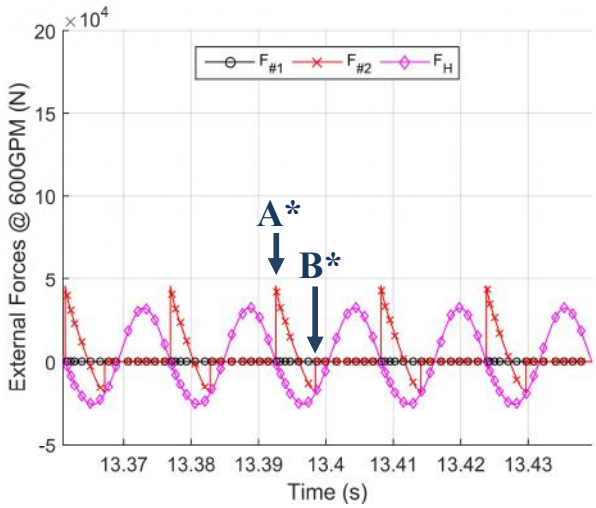

Figure 4.25: Simulation results of the excitation force and the impact forces at surfaces #1 and #2 for five impact cycles for the 7in tool model evaluated at an excitation frequency of 64.0 Hz (600GPM mud flow rate).

Finally, to understand how the impact dynamics affects the axial vibration results, the results shown in Fig. 4.24 and Fig. 4.25 are compared with the axial acceleration results for the same time window, as shown in Fig. 4.26.

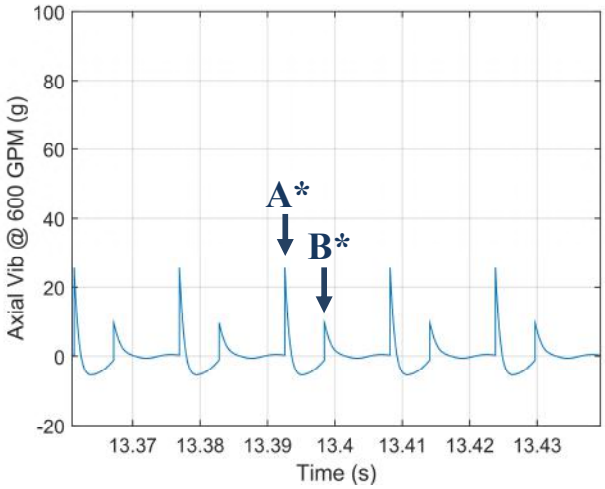

Figure 4.26: Simulation results of axial acceleration at x_1 for five impact cycles for the 7in tool model evaluated at an excitation frequency of 64.0 Hz (600GPM mud flow rate).

The simulations results presented in Fig. 4.26 seems to indicate a periodic behavior. Furthermore, the results reinforces that the variation in the axial vibration peaks (points A*) can be related to the dispersion in the maximum values of $F_{\#2}$, which is consistent with the results presented at Fig 3.42.

4.1.6 Overview of the impact pattern for all scenarios

An overview of the analysis of the impact pattern extracted from the impact force analysis is presented in Tab. 4.1.

Impact Surface	Mud Flow Rate				
	200GPM	320GPM	350GPM	500GPM	600GPM
Impact #1 (S)	Regular	Intermittent	Intermittent	No Impact	No Impact
Impact #2 (I)	Regular	Regular	Intermittent	Intermittent	Regular
Impact #3 (Off)	No Impact	No Impact	No Impact	No Impact	No Impact
Impact #4 (On)	No Impact	No Impact	No Impact	No Impact	No Impact

Table 4.1: Summary of the impact behavior for the respective impact surface for five different mud flow rates.

These results reveal that the dynamic behavior of the model can be related to the impact patterns at surfaces #1 and #2, which correspond to 2 of the 4 possible impact surfaces. Additionally, the results show that under certain conditions, there are scenarios that exhibit no impacts at the surface #1 (see Tab. 4.1). In these scenarios, the impacting anvil (m_2) does not impact the recoil spring (surface #1), which means that no energy is stored by the by elastic deformation of the spring (see section 2.1). Furthermore, this fact can be related with the severe reduction in the maximum amplitude of the impact force $F_{\#2}$ seen in Figs. 4.17 and 4.22, which are observed in the scenarios that exhibit no impacts at surface #1.

In summary, the impact dynamic analysis of the model revealed that in the current set of parameters for the tool, the impacts are registered in only two of the four impact surfaces (#1 and #2). Thus, the next section focuses on the classification of the dynamic behaviors of the tool based on the analysis of the impact forces of these two impact surfaces.

4.2 Classification of the dynamic behavior of the system

The classification associates the dynamic behavior observed in the simulation results (regular and intermittent impact behavior) with a dynamic label. This procedure requires the selection of a dynamic parameter (e.g., number of impacts in a given surface) that is affected by the change in the system's dynamic behavior. In addition, this parameter must exhibit distinct values or patterns for each dynamic behavior to be able to classify the simulation results.

Based on the assumption that similar dynamic behaviors are associated under a single dynamic label, the characterization process can be automated through a

computational routine. This routine should be able to simulate the mathematical model, process the available data, and classify each simulation result with its associated dynamic label.

In this work, the dynamic label is defined as the number of impacts in a given surface divided by the total number of impact cycles, as given in Eq. (4.1). This parameter, referred to as average impacts per cycle (Z^*) simplifies the detection and indexing process of regular and intermittent impact behaviors because it evaluates the consistency of each impact pattern in multiple impact cycles as follows:

$$Z_i^* = \frac{p_i}{n} \quad | \quad i = 1, 2, 3, 4 \tag{4.1}$$

where the subscript i represents an impact surface, p_i is number of impacts registered in a given impact surface evaluated in a determined number of impact cycles, which is represented by the variable n.

Implementing this dynamic parameter results in three major scenarios for each impact surface: a regular impact behavior with an average of one impact per cycle ($Z^* = 1$), an intermittent behavior ($0 < Z^* < 1$), and a scenario without impacts ($Z^* = 0$). This work proposes the analysis of the relation between each Z^* calculated for each impact surfaces to map the different dynamic behavior of this system. The simulations reveals that this dynamic label is associated with two impact surfaces, impact #1 and impact #2. Out of the nine possible combinations, the simulation results reveal that only six different dynamic behaviors were observed, as summarized in Tab. 4.2.

Impact Surface	1st Impact Scenario	2nd Impact Scenario	3rd Impact Scenario	4th Impact Scenario	5th Impact Scenario	6th Impact Scenario
Surface #1	$Z_1^* = 1$	$0 < Z_1^* < 1$	$0 < Z_1^* < 1$	$Z_1^* = 0$	$Z_1^* = 0$	$Z_1^* = 1$
Surface #2	$Z_2^* = 1$	$Z_2^* = 1$	$0 < Z_2^* < 1$	$0 < Z_2^* < 1$	$Z_2^* = 1$	$0 < Z_2^* < 1$

Table 4.2: Description of each dynamic behavior with their respective dynamic labels associated with the parameter Z^*.

This classification process is applied to the current set of input parameters of the mathematical model, as summarized in Tab 2.1. In this analysis, the relation between the dynamic behavior and the excitation frequency was investigated by observing the average impact per second (dynamic label) for each impact surface as a function of the mud flow rate as shown in Fig. 4.27a.

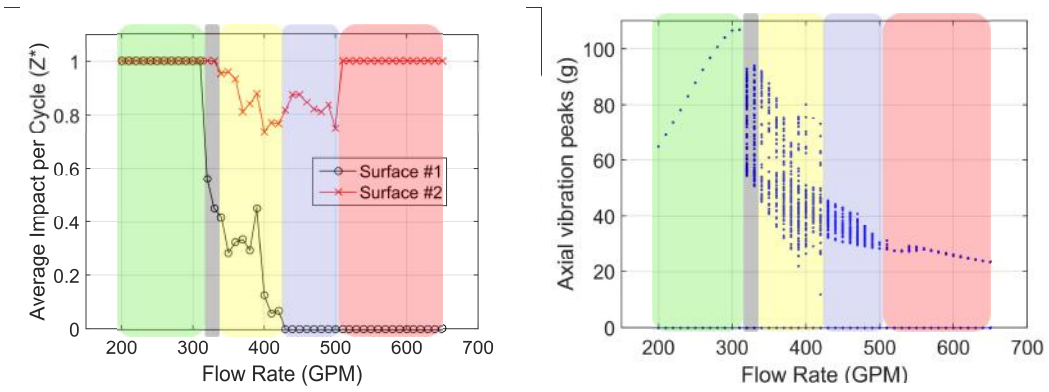

(a) (b)

Figure 4.27: Simulation results of (a) the dynamic label Z^* associated with their respective impact force scenarios for the impact surfaces #1 and #2 and (b) the axial vibration peaks and their associated impact force scenarios in a flow sweep analysis from 200- to 650-GPM mud flow rate.

The simulation results of the axial vibration peaks for the first degree of freedom as a function of the excitation frequency (mud flow rate) are shown in Figure 4.27b. This analysis divides the acceleration peaks in five different impact scenarios; indicating five unique dynamic behaviors (see Tab. 4.1).

The simulation results shown in Fig. 6.1 indicate that the first impact force scenario, represented by the green color, is associated with the region having high-average axial acceleration peaks and low-vibration peaks dispersion. In this impact force scenario, there is a direct relation between the increase of the excitation frequency and the increase of the axial vibration peaks.

The next region, which corresponds to the second impact scenario (black color), and shows an increase in the axial vibration peaks dispersion when compared with the previous scenario. Furthermore, the following two regions that represent the third (yellow color) and the fourth (blue color) impact force scenarios also present a high axial vibration peak dispersion.

The final scenario corresponds to the fifth impact force scenario (red color), which shows relatively low-axial vibration peak dispersion when compared to the other impact force scenarios. Thus, the increase in axial vibration peaks dispersion appears to be related the impact force scenarios that exhibit intermittent impact behavior on at least one impact surface. This observation is further supported by the fact that the first and fifth impact scenarios, which are the only scenarios that do not present intermittent impacts, show low-axial vibration peak dispersion.

4.3 Performance analysis

To evaluate and compare the performance of these impact behaviors (or dynamic labels), an additional parameter is proposed. This parameter is defined as a time average of the impulse, named impulse per second (J^*), as follows:

$$J^* = \frac{1}{\Delta t} \int_{t_0}^{t_1} F dt, \tag{4.2}$$

where J^* is the impulse per second, and F is the impact force applied in the time interval $[t_0, t_1]$.

This dynamic parameter allows the quantification of the performance of the tool because the time normalization enables a reliable and repeatable comparative analysis at different impact frequencies. The analysis of the impulse per second with respect to the mud flow rate is shown in Fig. 4.28.

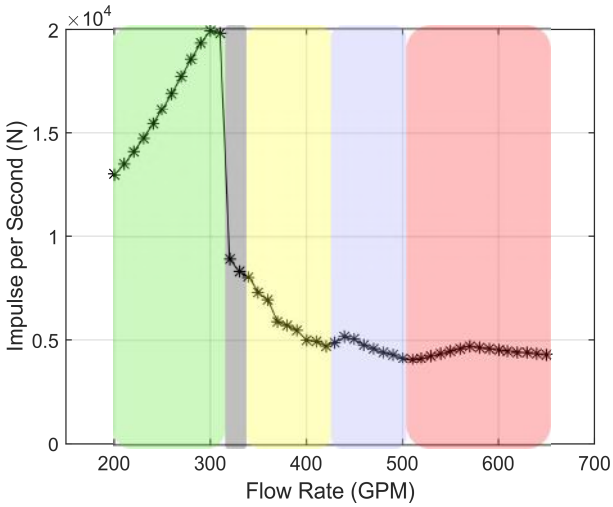

Figure 4.28: Simulation results of the impulse per second and their associated impact force scenarios in a flow sweep analysis from 200- to 650-GPM mud flow rate.

The results shows that the increase in the dispersion in axial acceleration peaks is related to an decrease in tool's performance. Further analysis reveals that the first impact force scenario (green color) contains the highest impulse per second when compared with the other impact force scenarios. Therefore, this analysis indicates that the best operating condition for the tool is within the first impact force scenario, which coincides with the region that exhibits periodic behavior. As a result, the parametric analysis presented in the next chapter will be focused on this first impact force scenario.

4.4 Summary

The results presented in section 4.1 explores the influence of each impact force in the dynamic behavior of the system. The main highlights of this section include:

- The analysis of the impact forces of the model reveals that the dynamic behavior of the model can be related to the impact patterns at surfaces #1 and #2, which correspond to 2 of the 4 possible impact surfaces (see Fig. 4.1).
- This analysis reveals that the dispersion in the values of impact force at the impact face (surface #2) are related to the presence of impact at the recoil spring (surface #1). The presence of intermittent impact at surface #1 means that different levels of energy will be store at the recoil spring. This translates into a greater variation in the maximum values of $F_{\#2}$ possible for each cycle. This is in accordance to the idea that that the recoil spring functions as a energy-storage mechanism.
- The results show that there seems to be a direct relation between maximum values of $F_{\#2}$ and the maximum axial vibration peak. An increase in the dispersion in the values of $F_{\#2}$ results in an increase in the axial vibration peaks dispersion, which is consistent with the results presented at Fig 3.42.

Next, section 4.2 focuses on the classification of the dynamic behaviors of the tool based on the results presented in the analysis of the impact forces. The main highlights of this section include:

- The relation between the average impacts per cycle (Z^*) for each impact surface is used to index and map the dynamic behavior observed in the simulation results.
- This analysis divides the acceleration peaks in five different impact scenarios; indicating five unique dynamic behaviors (see Tab. 4.1).
- The simulation results shown in Fig. 6.1 indicate that the first impact force scenario, represented by the green color, is associated with the region having high-average axial acceleration peaks and low-vibration peaks dispersion. In this impact force scenario, there is a direct relation between the increase of the excitation frequency and the increase of the axial vibration peaks.
- The next region, which corresponds to the second impact scenario (black color), and shows an increase in the axial vibration peaks dispersion when compared with the previous scenario. Furthermore, the following two regions that represent the third (yellow color) and the fourth (blue color) impact force scenarios also present a high axial vibration peak dispersion (see Fig. 6.1).

- The final scenario corresponds to the fifth impact force scenario (red color), which shows relatively low-axial vibration peak dispersion when compared to the other impact force scenarios. Thus, the increase in axial vibration peaks dispersion appears to be related the impact force scenarios that exhibit intermittent impact behavior on at least one impact surface. This observation is further supported by the fact that the first and fifth impact scenarios, which are the only scenarios that do not present intermittent impacts, show low-axial vibration peak dispersion (see Fig. 6.1).

Finally, section 4.3 introduces a performance parameter, named impulse per second (J^*), that is proposed to evaluate and compare the tool's performance as the excitation frequency varies. The main highlights of this section include:

- The performance parameter, named impulse per second (J^*) accounts for the average force being transmitted from the impacting mass into the bit assembly; therefore, to the rock formation.

- The analysis of the performance parameter shows that the increase in the dispersion in axial acceleration peaks is related to an decrease in tool's performance (see Fig. 4.28).

- Further analysis reveals that the first impact force scenario (green color) contains the highest impulse per second when compared with the other impact force scenarios (see Fig. 4.28). Therefore, this analysis indicates that the best operating condition for the tool is within the first impact force scenario, which coincides with the region that exhibits periodic behavior.

Chapter 5

Parametric Analysis

In this chapter, an investigation is performed to better understand how the design parameters affect the dynamic behavior of the model. Based on the previous steps, the purpose here is to run the mathematical model under different design parameters and understand how and in what way each one affects the dynamical behavior of the system. This analysis will be extended to the point of proposing possible design modifications to future prototypes.

Each parametric analysis focuses on evaluating the behavior of the model, and its performance as each parameter is varied individually. The three parameters selected for this analysis are the recoil spring stiffness, the gap between the impacting mass and the recoil spring, and the magnitude of the excitation force. For each analysis, the methodology is as follows:

1. Define the range of each of the three parameters based on the tool mechanical design
2. Simulate the mud flow sweep test for each parameter value (excitation frequency from 21.3 to 69.3Hz in 0.5Hz increments) considering 200 impact cycles after the response achieves steady-state behavior.
3. Capture the outputs
    - Impulse per second (J^*)
    - Impact force scenarios (Z^*)
4. Plot maps to show how the change of the chosen parameter affects each output.

The analysis of the dynamic behavior of the system is performed by using a nonlinear tool that enables the visualization of the different impact scenarios in a 2D map [27]. This map provides information about the characteristic of the impact force (impact scenarios) as a function of a given parameter of the parametric analysis

(e.g., recoil spring stiffness) and the mud flow rate as shown in Fig. 5.1. The color scheme used in this map is the same as discussed previously for the impact scenarios (see Tab. 4.2). It is important to emphasize that each point in this map corresponds to one numerical simulation obtained with a different combination of mud flow rate and investigated parameter values.

Although this map provides valuable information about the impact condition, this map does not provide information regarding the performance of the tool. To overcome this problem, a slight variance of this map is suggested, which exchanges the dynamic label (Z^*) for the impulse per second as the mapped variable as shown in Fig. 5.2. In this map variation, only he first impact scenario is addressed because it contains the highest impulse per second values. Additionally, the upper and lower limits of the impulse per second shown in Figs. 5.2, 5.4 and 5.6 are bounded to the maximum and minimum values obtained from all three parametric analysis.

5.1 Spring stiffness

The analysis of the impact force scenario mapping obtained through parametric analysis of the recoil spring stiffness is presented in Fig. 5.1.

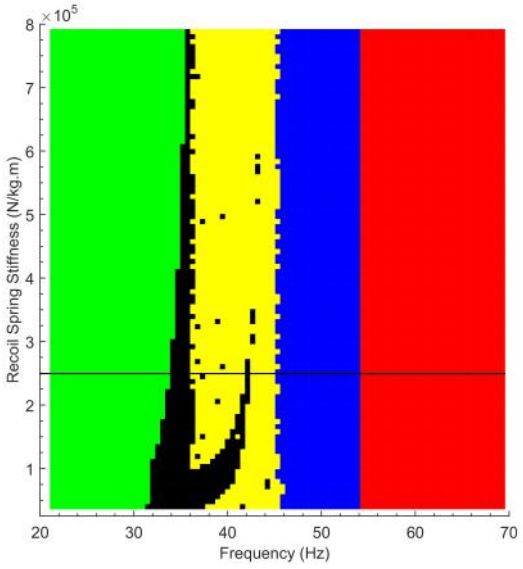

Figure 5.1: Impact force scenario mapping obtained through parametric analysis of the recoil spring stiffness (39.37 to 787.4 kN/kg.m). The color scheme used in this map is the same discussed for the impact scenarios (see Tab. 4.2)

The recoil spring stiffness range selected in this parametric analysis extends from 39.37 to 787.4 kN/kg.m in 0.79-kN/kg.m increments. The choice for this interval is related to the structural integrity of the recoil spring because the design recommendation of this component imposes a maximum elastic deformation

threshold to avoid permanent deformation. Therefore, a balance between the recoil spring stiffness and deformation is necessary to guarantee that this component meets the design requirements.

An analysis of the map shown in Fig. 5.1 reveals five impact behavior scenarios. Additionally, these results show that except for the second impact scenario (black color), there is minimal influence of this parameter in the impact scenario boundaries (see Fig. 5.1). It is important to observe that there is no change in the boundaries from the blue region to the red zone, which indicates that the change in the dynamic behavior is independent of the recoil spring stiffness. The basis for this assumption relies on the fact that both regions share the same characteristic because neither one of them impacts the recoil spring. Hence, the independence of the dynamic behavior in relation to the recoil spring stiffness is physically consistent.

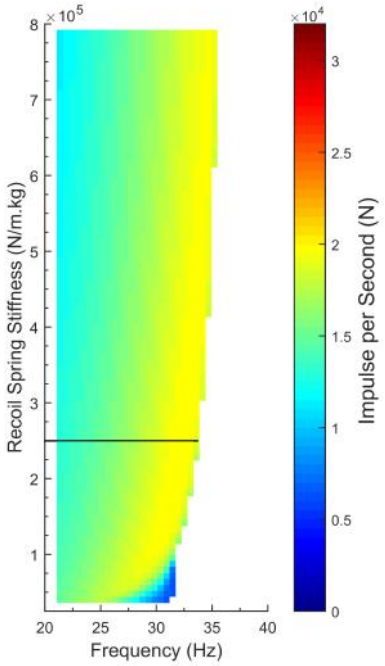

Figure 5.2: Impulse per second distribution within first impact force scenario region obtained through parametric analysis of the recoil spring stiffness (39.37 to 787.4 kN/kg.m).

The analysis of the impulse per second shown in Fig. 5.2 indicates a variation from approximately 5 to 20 kN within the first impact force region. Additionally, for a fixed recoil spring stiffness, the results indicate a gradual increase in the impulse per second values as the frequency increases. The variation in the recoil spring stiffness does appear to affect the maximum value of the impulse per second for the considered frequency range. However, there is a slight tendency to shift the region that exhibits the highest impulse per second toward higher frequencies. In summary, the recoil spring stiffness parametric analysis does not indicate a significant impact

in the overall dynamic behavior of the model. Thus, the recoil spring stiffness is not considered as being a fundamental parameter in a performance perspective.

5.2 Gap between the impacting mass and the recoil spring

The gap between the impacting mass and the recoil spring was evaluated in terms of the original gap value (see Eq. 5.1 and Fig. 2.3); hence, the name gap ratio, as defined by Eq. (5.2).

$$L_{gap} = L_3 - (L_2 + L_S + L_I + L_{On}), \tag{5.1}$$

where L_{gap} is the gap between the impacting mass and the recoil spring.

$$\text{gap ratio} = \frac{L^*_{gap}}{L_{gap}}, \tag{5.2}$$

where L^*_{gap} is the new gap between the impacting mass and the recoil spring proposed for every simulation.

The gap values analyzed in the current work were provided by a supporting engineering team, which ensured that these gap values are within the mechanical restrictions of the tool. Thus, the minimum value considered for this analysis assumes a 15% reduction of the gap between impacting mass and recoil spring (85% gap ratio), while the upper limit considers a 50% increase in this gap (150% gap ratio). This analysis considers an increase of 0.77% between each gap ratio.

An analysis of the map shown in Fig. 5.3 reveals six impact behavior scenarios as opposed to the previous parametric analysis in which only five impact scenarios were identified. The sixth impact scenario indicates intermittent impacts on the impact face and regular impacts on the recoil spring (see Tab. 4.2). This scenario appears only in 4 out of the 7,826 analyzed cases (0.05% of the total number of cases); hence, this scenario is not within the interests of this present work. In relation to the dynamic behavior, the analysis of the first impact scenario (green color) shows an expansion of its boundaries for higher flow rates. This extension of the first impact scenario is beneficial for analyzing the performance of the prototype because it allows the tool to operate over a wider range of mud flow rates without compromising tool performance.

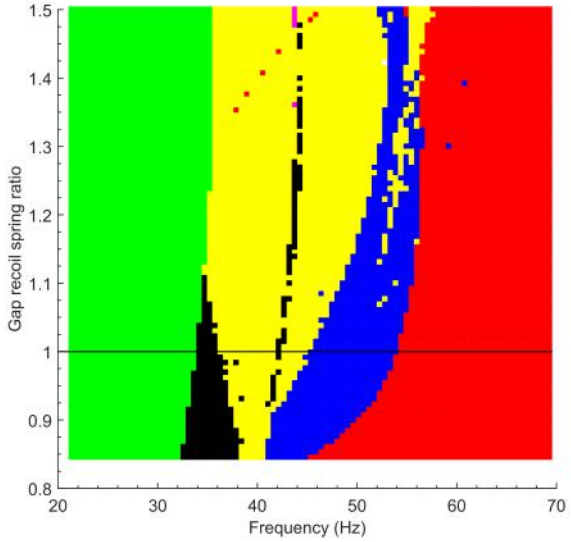

Figure 5.3: Impact force scenario mapping obtained through parametric analysis of the gap between the impacting mass and the recoil spring (85% to 150% of the original value). The color scheme used in this map is the same discussed for the impact scenarios (see Tab. 4.2)

The analysis of the impulse per second shown in Fig. 5.4 indicates that, for a fixed gap value, there is a gradual increase in the impulse per second values as the frequency increases.

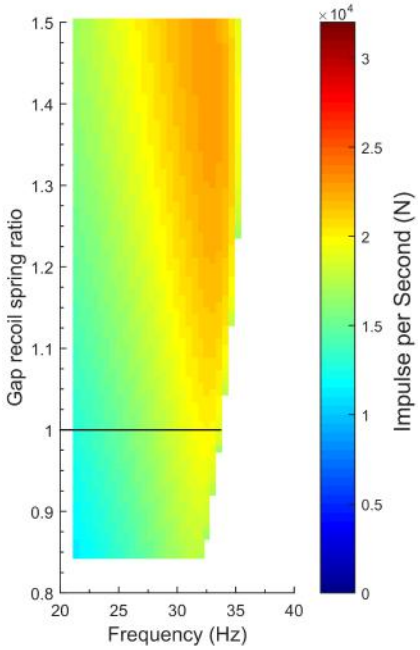

Figure 5.4: Impulse per second distribution within first impact force scenario region obtained through parametric analysis of the gap between impacting mass and recoil spring (85% to 150% of the original value).

Furthermore, there is also an increase in impulse per second as the gap increases from the maximum of 20 kN in the original design (100% gap ratio) to 22.8 kN in the best scenario (150% gap ratio), which corresponds to a 14% improvement. Therefore, the best operating range within this parametric analysis of this parameter requires a rotary frequency of 30 Hz to 34 Hz and a 50% increase in the gap between impacting mass and recoil spring.

5.3 Magnitude of the excitation force

The magnitude of the excitation force was evaluated from 133.54 to 534.17 N/kg in 6.677-N/kg increments. The choice for this interval was provided by a supporting engineering team that ensured the structural integrity of certain components of the tool . An analysis of the map of the magnitude of the excitation force shown in Fig 5.5 indicates five impact behavior scenarios. In reference to the first impact scenario (green zone), the increase in the excitation force magnitude results in the most significant expansion of the frequency range when compared with the parametric analysis of the other four parameters (34 Hz at 300.5 N/kg to 39 Hz at 534.17 N/kg). Although there are complex behavioral changes in the boundaries of each impact scenario, represented by the change in color, the analysis focused on the first impact scenario (green zone) because this region exhibits the highest impulse per second values.

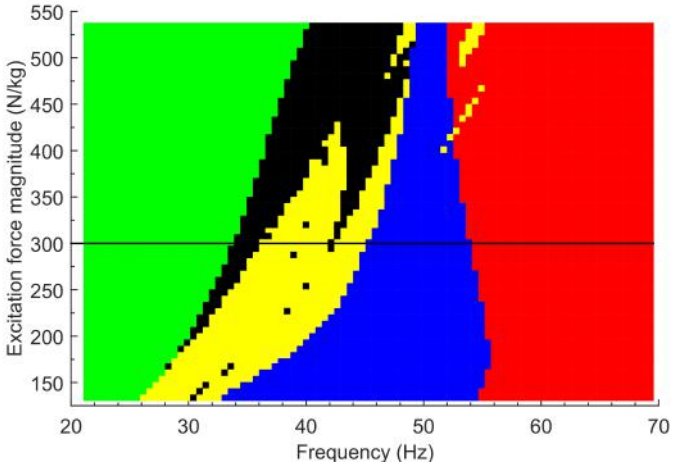

Figure 5.5: Impact force scenario mapping obtained through parametric analysis of the magnitude of the excitation force (133.54 to 534.17 N/kg). The color scheme used in this map is the same discussed for the impact scenarios (see Tab. 4.2)

In reference to the impulse per second, the results shown in of Fig. 5.6 indicate that when comparing the current design (black line) with the most excellent scenario obtained in this map, there is a 56% increase in impulse per second (from 20 to 31.2

kN) as the excitation force magnitude increases 78% (from 300.5 to 534.17 N/kg).

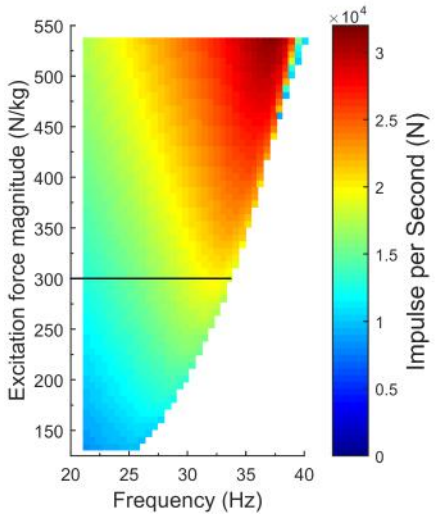

Figure 5.6: Impulse per second distribution within first impact force scenario region obtained through parametric analysis of the magnitude of the excitation force (133.54 to 534.17 N/kg).

5.4 Design recommendations

With the available results from the parametric analysis, the selection of the recommended design considers the best performance scenario in each of the sensitivities analysis. Therefore, the proposed improved design includes 472.4 kN/kg.m of recoil spring stiffness, a 50% increase in the gap between impacting mass and recoil spring, and 534.17-N/kg of excitation force. Furthermore, a performance comparison (impulse per second) between the recommended design and the original prototype is shown in Fig. 5.7.

The simulation results of impulses per second of the original and the recommended designs showed an increase in the impulse per second from 20 to 37 kN, which translates to an 85% increase from the original design (see Fig. 5.7). To evaluate the ideal operating range for this tool, the criteria defined for an acceptable performance assumes a 10% variation in the maximum impulse per second. Thus, the original design ideal operating range consists of mud flow rates from 270 to 310 GPM (impulse per second greater than 18 kN). The recommended design exhibits an ideal operating range from 300 to 390 GPM (impulse per second greater than 33.3kN), which translates to a 125% increase in excitation frequency range when compared with the original design.

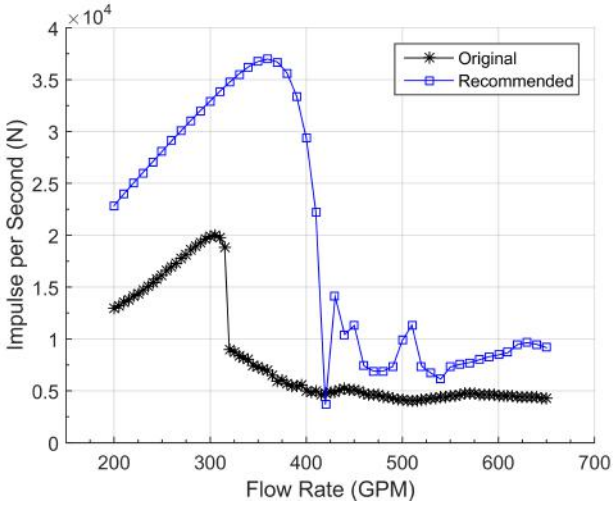

Figure 5.7: Simulation results of the impulses per second in a flow sweep analysis from 200- to 650-GPM mud flow rate for the original and the recommended design.

It is important to emphasize that the combination of the parameters showing the best performance in their separate parametric analysis does not translate into the optimal design for the prototype. Thus, in a future analysis, a multi parametric analysis would be a valid alternative for improving the current results. Moreover, there appears to be a relation between the phase differences among the excitation force, the impact force from the recoil spring, and the impact force from the impact face and the dynamic behavior of the tool. In that sense, additional analysis is required to understand the effects of this relation on the performance of the prototype.

Chapter 6

Concluding Remarks

This work proposes vibro-impact mathematical model to investigate the axial vibration inside a vibration-assisted drilling tool. The validation process of this model included acceleration field data in high acquisition frequency, and in two locations of the vibration-assisted drilling tool. This model is composed of seven degree-of-freedom, with four impact surfaces, and is able to reproduce complex dynamic behavior with small computational cost.

The analysis of the relation between the axial vibration peaks and the excitation force frequency reveals that the mathematical model is capable of capturing and reproducing the main dynamic behavior of the vibration-assisted drilling tool. The simulation results show an overall good match between field data and model outputs for the axial accelerations. The dynamic model is also able to reproduce the relation between the axial vibration peaks and the mud flow rate.

The comparison between the simulation results and the acceleration data, which was recorded for several excitation frequencies, introduces a more detailed analysis of the impact dynamics of the tool. The results show an overall good match between field data and model outputs for the impact frequencies and the dynamic behavior for low to medium mud flow rates. In general, the dynamic model shows a satisfactory match of dynamical behavior throughout the entire frequency range that is available.

The validation process also revealed limitations of the mathematical model. The results show a poor match of axial accelerations measured close to the drill bit (x_1) at high excitation frequencies scenarios. A possible explanation for this phenomenon could be related to the higher influence of system hydraulics, which is not considered in the current dynamic model of the tool. Additionally, the model was not able to match axial accelerations measured above the positive displacement motor (x_5), which might be a limitation of this model, as the axial-lateral coupling is not considered.

In relation to the axial nonlinear dynamics of the vibro-impact system, the relation between the average impacts per cycle (Z^*) for each impact surface is

used to index and map the dynamic behavior observed in the simulation results. Additionally, a performance parameter, named impulse per second (J^*), is proposed to quantify the tool's performance. This parameter accounts for the average force being transmitted from the impacting mass into the bit assembly; therefore, to the rock formation.

The parametric analysis of the recoil spring stiffness did not reveal a significant influence of this parameter on the overall dynamic behavior of the model. Thus, this parameter is not considered essential from a performance perspective. Alternatively, the analysis of the gap between the second degree of freedom and the recoil spring indicates a gradual increase in the impulse per second values as the frequency increases within the first impact scenario (green region). Furthermore, the simulation results showed an increase in impulse per second as the gap increases. The analysis of the magnitude of the excitation force indicated that there is a possible 56% increase in impulse per second. A second benefit from the simulation results of this impact scenario is the increase in frequency range (mud flow rate) when the magnitude of the excitation force increases.

With the available results from the parametric analysis, the selection of the recommended design considered the best performance scenario in each of the sensitivities analysis. A comparison between the simulation results of the original and the recommended designs showed an increase in the impulse per second from 20 to 37 kN, which translates into a 85% increase in impulse per second when compared with the original design. The recommended design exhibits an ideal operating range from 300 to 390 gal/min mud flow rate, which translates to a 125% increase in mud flow range when compared to the original design.

In regards to future projects, the following analysis are proposed:

- The analysis of the dynamic behavior of the model revealed that the variation in the excitation frequency affects the impact pattern of the impact forces. Based on the current results, there appears to be a relation between the dynamic behavior of the tool and the the phase differences among the excitation force and the impact forces. Further investigation is required to explore the root cause of this relationship.

- The characterization of the dynamic behavior of the model showed that in there are a total of six unique dynamic behaviors for the current set of input parameters for the model. In that regard, further analysis can be performed with a wider range of input parameters to investigate the presence of other possible dynamic behaviors. For instance, by reducing the increment of the excitation frequency range from 1.1 Hz to 0.1 Hz (see Fig. 6.1a), the results show different values of Z^* that were not observed in the current set of input

parameters (see Fig. 6.1b). This indicate that there are other unique dynamic behavior that can be further analysed in a future work.

- It is important to emphasize that the combination of the parameters showing the best performance in their separate parametric analysis does not translate into the optimal design for the prototype. Thus, a multi parametric analysis would be a valid alternative for improving the current results.

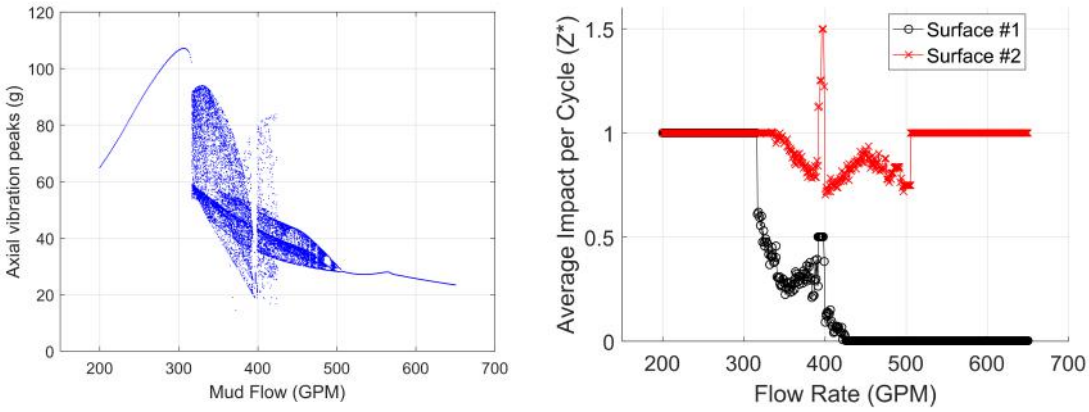

(a) (b)

Figure 6.1: Simulation results of (a) the axial vibration peaks and (b) the dynamic label Z^* associated with their respective impact force scenarios for the impact surfaces #1 and #2 in a flow sweep analysis from 200- to 650-GPM mud flow rate with 1GPM increments.

Bibliography

[1] SCHLUMBERGER. *Hammer Bit Percussion Drilling – Operating Instructions*. Relatório Técnico E6.00101, Smith Bits - A Schlumberger Company, 2012.

[2] PLACIDO, J. C. R., LAGE, A. C. V., CARVALHO, D. J., et al. "A new type of hydraulic hammer compatible with conventional drilling fluids". In: *SPE Annual Technical Conference and Exhibition*. Society of Petroleum Engineers, 2003.

[3] LAGRECA, A., DE SANTANA, D., SUAREZ, G., et al. "Fluid Percussion Hammer Field Test in the Alocthonous Cretaceous Block, Eastern Venezuela". In: *Canadian International Petroleum Conference*. Petroleum Society of Canada, 2002.

[4] TIBBITTS, G. A., LONG, R. C., MILLER, B. E., et al. "World's first benchmarking of drilling mud hammer performance at depth conditions". In: *IADC/SPE Drilling Conference*. Society of Petroleum Engineers, 2002.

[5] GEE, R., RAMIREZ, T., BARTON, S. P., et al. "Reliable Hammer Motor smashes its way to Speedy Success in Brazil". In: *IADC/SPE Drilling Conference and Exhibition*. Society of Petroleum Engineers, 2012.

[6] HERRINGTON, D., BARTON, S., POWELL, S., et al. "Step Change Technology Amplifies Vertical Force Applied to Formation at the Bit Enhancing Cutting Efficiency". In: *SPE Asia Pacific Oil and Gas Conference and Exhibition*. Society of Petroleum Engineers, 2013.

[7] HERRINGTON, D., BARTON, S. P., COTE, B., et al. "Hammer Motor Breaks New Ground in China". In: *SPE Asia Pacific Oil and Gas Conference and Exhibition*. Society of Petroleum Engineers, 2012.

[8] POWELL, S. W., HERRINGTON, D., BOTTON, B., et al. "Fluid hammer increases PDC performance through axial and torsional energy at the bit". In: *SPE Annual Technical Conference and Exhibition*. Society of Petroleum Engineers, 2013.

[9] BREHL, D., DOW, T. "Review of vibration-assisted machining", *Precision engineering*, v. 32, n. 3, pp. 153–172, 2008.

[10] MA, C. X., SHAMOTO, E., MORIWAKI, T. "Study on the thrust cutting force in ultrasonic elliptical vibration cutting". In: *Materials Science Forum*, v. 471, pp. 396–400. Trans Tech Publ, 2004.

[11] SCHLUMBERGER. *Vibration Assisted Drilling Systems*. Relatório Técnico CONFIDENTIAL, Schlumberger Company, 2014.

[12] BABITSKY, V., ASTASHEV, V., MEADOWS, A. "Vibration excitation and energy transfer during ultrasonically assisted drilling", *Journal of Sound and Vibration*, v. 308, n. 3-5, pp. 805–814, 2007.

[13] "Schlumberger Oilfield Glossary". `https://www.glossary.oilfield.slb.com`. Accessed: 2019-05-28.

[14] "How Oil Drilling Works". `https://science.howstuffworks.com/environmental/energy/oil-drilling4.htm`. Accessed: 2019-05-28.

[15] BRUNO, M. S. *Fundamental Research on Percussion Drilling: Improved rock mechanics analysis, advanced simulation technology, and full-scale laboratory investigations*. Relatório técnico, Terralog Technologies Inc., 2005.

[16] RILEY, W., STURGES, L. "Engineering Mechanics Dynamics". John Wiley and Sons, 1996.

[17] GILARDI, G., SHARF, I. "Literature survey of contact dynamics modelling", *Mechanism and machine theory*, v. 37, n. 10, pp. 1213–1239, 2002.

[18] KIM, S.-W. *Contact dynamics and force control of flexible multi-body systems*. Tese de Doutorado, McGill University Libraries, 1999.

[19] WANG, Y.-T., KUMAR, V.-J. "Simulation of mechanical systems with multiple frictional contacts", *Journal of Mechanical Design*, v. 116, n. 2, pp. 571–580, 1994.

[20] STRONGE, W. "Unraveling paradoxical theories for rigid body collisions", *Journal of Applied Mechanics*, v. 58, n. 4, pp. 1049–1055, 1991.

[21] HERTZ, H., JONES, D. E., SCHOTT, G. A. "Miscellaneous papers". Macmillan and Company, 1896.

[22] GOLDSMIT, W. "The Theory and Physical Behavior of Colliding Solids (Arnold, London, 1960); FG Bridges, A. Hatzes, and DNC Lin", *Nature (London)*, v. 309, pp. 333, 1984.

[23] HUNT, K., CROSSLEY, F. "Coefficient of restitution interpreted as damping in vibroimpact", *Journal of applied mechanics*, v. 42, n. 2, pp. 440–445, 1975.

[24] LANKARANI, H., NIKRAVESH, P. "A contact force model with hysteresis damping for impact analysis of multibody systems", *Journal of mechanical design*, v. 112, n. 3, pp. 369–376, 1990.

[25] PAVLOVSKAIA, E., WIERCIGROCH, M., GREBOGI, C. "Modeling of an impact system with a drift", *Physical Review E*, v. 64, n. 5, pp. 056224, 2001.

[26] FRANCA, L. F. P., WEBER, H. I. "Experimental and numerical study of a new resonance hammer drilling model with drift", *Chaos, Solitons & Fractals*, v. 21, n. 4, pp. 789–801, 2004.

[27] AGUIAR, R., WEBER, H. "Mathematical modeling and experimental investigation of an embedded vibro-impact system", *Nonlinear Dynamics*, v. 65, n. 3, pp. 317–334, 2011.

[28] PAVLOVSKAIA, E., WIERCIGROCH, M., WOO, K.-C., et al. "Modelling of ground moling dynamics by an impact oscillator with a frictional slider", *Meccanica*, v. 38, n. 1, pp. 85–97, 2003.

[29] PAVLOVSKAIA, E., WIERCIGROCH, M. "Periodic solution finder for an impact oscillator with a drift", *Journal of Sound and Vibration*, v. 267, n. 4, pp. 893–911, 2003.

[30] AJIBOSE, O. K., WIERCIGROCH, M., PAVLOVSKAIA, E., et al. "Global and local dynamics of drifting oscillator for different contact force models", *International Journal of Non-Linear Mechanics*, v. 45, n. 9, pp. 850–858, 2010.

[31] CAO, Q.-J., WIERCIGROCH, M., PAVLOVSKAIA, E., et al. "Bifurcations and the penetrating rate analysis of a model for percussive drilling", *Acta Mechanica Sinica*, v. 26, n. 3, pp. 467–475, 2010.

[32] PETERKA, F., KOTERA, T., ČIPERA, S. "Explanation of appearance and characteristics of intermittency chaos of the impact oscillator", *Chaos, Solitons & Fractals*, v. 19, n. 5, pp. 1251–1259, 2004.

[33] LIU, H., KOU, S., LINDQVIST, P.-A., et al. "Numerical simulation of the rock fragmentation process induced by indenters", *International Journal of Rock Mechanics and Mining Sciences*, v. 39, n. 4, pp. 491–505, 2002.

[34] GREEN, S. J., JUDZIS, A., CURRY, D., et al. "Single Cutter Testing Improves Understanding of Deep-Well Hammer Drilling Performance". In: *SPE Annual Technical Conference and Exhibition*. Society of Petroleum Engineers, 2005.

[35] POWELL, P. E., GREENWOOD, R., SISSON, D. "Radial vibrational apparatus". mar. 22 2016. US Patent 9,290,996.

[36] ROBERT, W. F., ALAN, M. T., PHILIP, J. P. "Introduction to fluid mechanics", *John Wiley & Sons, Inc*, p. 38, 1998.